Title

Dual Reconfigurable Exoskeleton Hand System with Opposable Thumbs

Author

Ferguson, Peter Walker

Publication Date

2022

UNIVERSITY OF CALIFORNIA
Los Angeles

Dual Reconfigurable Exoskeleton Hand System with Opposable Thumbs

A dissertation submitted in partial satisfaction
of the requirements for the degree
Doctor of Philosophy in Mechanical Engineering

by

Peter Walker Ferguson

2022

ABSTRACT OF THE DISSERTATION

Dual Reconfigurable Exoskeleton Hand System with Opposable Thumbs

by

Peter Walker Ferguson
Doctor of Philosophy in Mechanical Engineering
University of California, Los Angeles, 2022
Professor Jacob Rosen, Chair

Between a global pandemic, aging population, and labor shortages, there is an ongoing spike in the demand for healthcare that cannot be satisfied with traditional methods and the human workforce. Robotic technology offers a solution to this dilemma; applying robotics to healthcare is an active area of research that has begun to be widely commercialized. While there are many potential avenues for robots to improve health and well-being, my research has focused on two areas in particular: the development of robotic hand exoskeletons for rehabilitation and the enhancement of robotic surgery via automation and sensor development.

Exoskeletons have been shown to be effective for use in physical rehabilitation of numerous conditions including spinal cord injury and stroke. However, at present, the huge majority of exoskeleton systems are constructed for only the arm (from shoulder to wrist), back, lower limbs, or hands. Few systems have been developed that combine both full arm and hand systems, and those that do generally have limited actuation of the hand. This is partly because the mechanical complexity of the hand requires rigid hand exoskeletons to be complex and bulky if they are able to control many of the important degrees of freedom. This

bulk and complexity makes the hand systems challenging to successfully integrate onto the distal end of an arm exoskeleton. However, there is significant demand for combined arm and hand rehabilitation exoskeletons because many activities of daily living, that physical therapy focuses on retraining, require reaching and grasping together. The overarching goals of this research are to develop a novel hand exoskeleton, experimentally evaluate its capabilities in preparation for application to stroke rehabilitation, and integrate it on the existing EXO-UL8 and concurrently developed BLUE SABINO upper limb exoskeleton systems. Chapter 1 provides an introduction on hand exoskeleton systems, with a focus on those designed for rehabilitation.

My work on hand exoskeletons started by inheriting a hand exoskeleton mechanical design from Brando Dimapasoc, a graduating Master's Degree student, that was developed as part of NSF Award #1532239. The system was intended to be attached to the EXO-UL8 and BLUE SABINO arm exoskeletons, had six active and six passive degrees of freedom, had three reconfigurable linkages to control the thumb and two groupings of fingers, used a bowden cable transmission system to enable remote placement of actuators, and was optimized to fit 90% of the general population. However, the design had only been tested as a 3D-printed prototype in a modified and simplified form. Further, the necessary electronic hardware (other than motor and sensor selection) and control software had not been started. Thus, the first stage of my research was to bring this first-generation hand exoskeleton to a functional state. This involved the mechanical assembly, the electrical design and assembly, and the software and control development of the system. Through testing, it was determined that a significant number of improvements must be made to the system in order for it to be suitable for use. Details of this work are contained in Chapter 2.

With the lessons learned from development and testing of the first-generation hand exoskeleton, the next stage of my research involved the nearly complete redesign of the system in order to create the second-generation hand exoskeleton named the "Opposable-Thumb Hand Exoskeleton for Rehabilitation" or "OTHER Hand". As the name implies, the system is designed to control opposition/reposition of the thumb in addition to the flexion/extension of each digit. This is a notable feature, not only because of the importance of opposition/reposition in many grasping tasks, but also because only a handful of exoskeletons in the literature control this motion. The OTHER Hand shares a number of features with the first-generation system, though the execution of each is different. It attaches to both the EXO-UL8 and BLUE SABINO arm exoskeletons, is actuated using a Bowden Cable transmission such that the motor pack can be located remotely, has three reconfigurable linkages to control the thumb and two groupings of fingers in order to enable nearly all grasps, and is optimized to fit 90% of the population. The system has six active and eight passive degrees of freedom per hand. Chapter 3 documents the design of the OTHER Hand.

Due to the numerous novel design choices made for the OTHER Hand, combined with the mechanical complexity of the hand in general, and thumb in particular, it is not feasible to know with certainty the types of grasps that can be actuated in the exoskeleton for the wide range of hand shapes and sizes. As such, it is necessary to validate the design of the OTHER Hand through testing with a group of subjects. This was accomplished through adaptation of the Anthropomorphic Hand Assessment Protocol for use with an exoskeleton to test the ability of thirteen subjects to grasp and manipulate 25 objects of the Yale-Carnegie Mellon-Berkeley Object Set using eight prehensile grasps and two non-prehensile hand postures. Additionally, the OTHER Hand was mounted on the EXO-UL8, and both systems were manually controlled to verify compatibility, workspace, and ability to bi-manually grasp a sample object. Chapter 4 presents the testing protocol and results.

While exoskeletons for rehabilitation is an increasingly popular research area, robotic surgical platforms already have widespread commercial use and profound effects on clinical outcomes. Classically, these systems are controlled directly by a surgeon at a console in the same or adjacent room. They can augment the senses and movement precision of the surgeon during open or laparoscopic surgery in order to enhance the surgeon's skills. However, surgeons commonly work exceptionally long hours in an environment where a single mistake can be fatal. Additionally, certain surgical subtasks are time-consuming, repetitive, and common to many different operations. Automating these subtasks has the potential to reduce the burden on surgeons while standardizing outcomes. Automation of one such subtask, soft tissue manipulation, is described in Chapter 5.

Cataract surgery ranks among the most common operating room procedures worldwide. The aim of the surgery is to replace the clouded biological lens with a clear synthetic lens. Despite the prevalence, this operation is currently performed manually by a surgeon, and generally is fast, standardized, and safe. However, the human body is notably non-optimal for performing cataract surgery due to the transparency and fragility of the tissues of the eye. In order to remove the lens, it is standard to break it apart with phacoemulsification, use an irrigation/aspiration handpiece to aspirate the lens material, and then polish any remaining lens material from the capsular bag. Unfortunately, the back of this bag, the posterior capsule, is transparent, mere microns thin, and easily ruptured from contact, ultrasound energy, or pressure. Rupturing the posterior capsule causes the vitreous of the inner eye to spill out, resulting in critical failure of the surgery. Additional information about the location of the tool tip within the eye could be used to reduce the risk of such a failure. To this end, a proof-of-concept modification of a tool to add bioelectrical impedance sensing and tissue classification was developed and tested on porcine eyes. This research is summarized in Chapter 6.

The dissertation of Peter Walker Ferguson is approved.

Dennis Hong

Joel Perry

Veronica Santos

Jacob Rosen, Committee Chair

University of California, Los Angeles

2022

To all those who supported me along the way...

TABLE OF CONTENTS

LIST OF FIGURES

LIST OF TABLES

Acronyms

A/A *Abduction/Adduction.*

AAHE *Arm and Hand Exoskeleton.*

ADLs *Activities of Daily Living.*

ADT *AdaBoosted Decision Tree.*

AHAP *Anthropomorphic Hand Assessment Protocol.*

BSS *Balance Salt Solution.*

CG *Cylindrical Grip.*

CMC *CarpoMetaCarpal.*

CNN *Convolutional Neural Net.*

CPM *continuous passive motion.*

DH *Modified Denavit-Hartenberg.*

DIP *Distal InterPhalangeal.*

DoF *Degree of Freedom.*

DT *Decision Tree.*

DVG *Diagonal Volar Grip or adducted thumb grip.*

EEG *electroencephalography.*

EG *Extension Grip.*

F/E *Flexion/Extension.*

GAS *Grasping Ability Score.*

GTs *Grasp Types/hand postures.*

GUI *Graphical User Interface.*

H *Hook grip.*

I/A *Irrigation/Aspiration.*

IDP *Image Desired Point.*

IP *Index Pointing/pressing.*

IRISS *Intraocular Robotic Interventional Surgical System.*

ITP *InTerPhalangeal.*

LP *Lateral Pinch.*

MCP *MetaCarpoPhalangeal.*

MIS *Minimally Invasive Surgery.*

ML *Machine Learning.*

O/R *Opposition/Resposition.*

OCT *Optical Coherence Tomography.*

OTHER Hand *Opposable Thumb Hand Exoskeleton for Rehabilitation.*

P *Platform.*

PC *Posterior Capsule.*

PD *Proportional-Derivative.*

PDE *Partial Differential Equation.*

PIP *Proximal InterPhalangeal.*

PP *Pulp Pinch or palmar pinch.*

RAS *Robot-Assisted Surgery.*

RF *Random Forest.*

RL *Reinforcement Learning.*

ROM *Range Of Motion.*

sEMG *Surface electromyography.*

SG *Spherical Grip.*

SGD *Stochastic Gradient Descent.*

SL *Synergic Learning.*

SVM *Support Vector Machine.*

TGP *Tissue Grasp Point.*

TP *Tripod Pinch.*

TTP *Tissue Target Point.*

YCB *Yale-CMU-Berkeley Object Set.*

ACKNOWLEDGMENTS

During my graduate studies, truly momentous and tumultuous events have occurred both for the world at large and myself personally. It has been a crazy ride, and I have only been able to reach the end of the journey due to the support of more people than I can reasonably mention. That said, I would like to acknowledge a number of people in particular:

To my advisor, Professor Jacob Rosen: thank you for everything. You accepted me into your lab, enabled me to pursue research topics I am excited about, funded my studies and research, and guided me to the next step in my career. It has been a pleasure researching and teaching with you.

To the various other professors, teachers, and mentors that have shaped me from an inquisitive child to a UCLA engineering PhD, you have my gratitude. To my 5^{th} grade teacher, Mrs. Fisk, you turned me from a C student to an academic. Henry Holcomb, you introduced me to scientific research and enabled me to coauthor a publication as a high-school student. To Professors Page, Ula, Marino, Huang, Jie, Vejarano, Kinsey, Hopkins, Santos, and Clites, to name a few, your dedication to teaching inspired me. To Professors Santos, Perry, Edgerton, and Hong you supported me at various stages of my PhD, from giving me my first teaching assistant position, to introducing me to your colleagues, to providing feedback on my research.

To my lab mates, past and present: it has been a blast. Hao, our ever present verbal jousting made things bearable, even during the hardest struggles and when the world turned upside down. Your messages about research at 1AM on weekends let me know I was not the only one. Changyeob, thank you for your friendship. Your kindness and diligence make you a delight to be around, and I am excited that we can keep working together. Sahba, you introduced me to writing research papers and brought me into your research projects. My knowledge, accomplishments, and PhD experience would be lesser had you not been there. Jianwei, I admire your patience with my ineptitude at coding. You are brilliant, and I hope our friendship has been even a fraction as enjoyable and helpful for you as it has been for me. Erik, 269A would have been unbearable without you and blue-haired Peter. Yang and Haoran, thank you for leading the way. Ji, your engineering is inspirational, and I truly appreciate your willingness to help at a moment's notice. Brando, Brandon, and Ray, we only got to work together for a short time, but that time was valuable to me. Finally, to Seungmin, Mianzhi, Leonardo, Yasamin, Hanbyeol, Bita, Pietro, and Sunwoong, I appreciate your support and friendship. Know that I am rooting for you!

I would also like to thank my friends outside the lab. Will, your continued friendship over the decades and even across thousands of miles is irreplaceable to me. Jong, randomly matching with you as a roommate was incredible, I could not have asked for a better person to live with. The only thing more awe-inspiring than your work ethic is your APM. Eric, we may be in different labs but it feels like we have done this journey together. Catching beers with you is always a joy, and I am looking forward to keeping it going for years to come. To my friends in Archery and Aikido, thank you for all the brightness and joy.

Linna, I am at a loss as to how to even begin to express my gratitude for all that you have brought to my life. Your presence by my side has enabled me to keep going despite the challenges, and stay focused and hopeful. You are so important to me, and I can't wait for our future.

Mom, Dad, Dana, I can confidently say I would not be where I am were it not for each of you. Mom, you have given me your endless love and support, even in the toughest of times. Just because I will have a PhD doesn't mean I won't still call you asking your advice. Dad, your guidance and encouragement along my path have been instrumental. You are why I started my PhD in the first place. Dana, you led the way for so much of my life. I am profoundly thankful and proud to have you as my brother.

Lastly, I would like to thank the late Frederick Schwedner. I will always remember your enthusiasm and encouragement. Our chats motivated me like little else could; I always wanted to be able to show you progress.

VITA

2008-2012	B.S. in Electrical Engineering, Loyola Marymount University.
2015-2017	M.S. in Mechanical Engineering, UCLA.
2015-2022	Graduate Researcher, Bionics Lab, UCLA.
2016-2022	Teaching Assistant in Engineering/Mechanical Engineering, UCLA.
2019-2022	Lecturer in Electrical Engineering, Loyola Marymount University.

PUBLICATIONS

J. Sun, **P. W. Ferguson**, and J. Rosen, “Suppressing Human-Induced Oscillations in Physical Human-Robot Interaction with an Upper-Limb Exoskeleton Using Rate-Limiting,” in *2022 IEEE/RSJ Int. Conference on Intelligent Robots and Systems (IROS)*, in press, 2022.

S. A. Pedram*, **P. W. Ferguson***, M. J. Gerber, C. Shin, J.-P. Hubschman, and J. Rosen, “A Novel Tissue Identification Framework In Cataract Surgery Using an Integrated Bioimpedance-Based Probe and Machine Learning Algorithms,” *IEEE Transaction on Biomedical Engineering (TBME)*, vol. 69, no. 2, pp. 910–920, 2022.

S. A. Pedram*, C. Shin*, **P. Ferguson**, J. Ma, E. Dutson, and J. Rosen, “Autonomous Suturing Framework and Quantification Using a Cable-Driven Surgical Robot,” *IEEE Transaction on Robotics (TRO)*, vol. 37, no. 2, pp. 404–417, 2021.

S. A. Pedram*, **P. W. Ferguson***, C. Shin, A. Mehta, E. Dutson, F. Alambeigi, and J. Rosen, “Toward Synergic Learning for Autonomous Manipulation of Deformable Tissues via Surgical Robots: An Approximate Q-Learning Approach,” in *8th Int. Conference on Biomedical Robotics and Biomechatronics (BioRob)*, 2020, pp. 878–884.

P. W. Ferguson, B. Dimapasoc, and J. Rosen, “Optimal Kinematic Design of the Link Lengths of a Hand Exoskeleton,” in *Wearable Robotics: Systems and Applications*, Academic

Press, 2020, pp. 193–206.

P. W. Ferguson, Y. Shen, and J. Rosen, "Hand Exoskeleton Systems—Overview," in *Wearable Robotics: Systems and Applications*, Academic Press, 2020, pp. 149–175.

H. Lee, **P. W. Ferguson**, and J. Rosen, "Lower Limb Exoskeleton Systems—Overview," in *Wearable Robotics: Systems and Applications*, Academic Press, 2020, pp. 207–229.

Y. Shen, **P. W. Ferguson**, and J. Rosen, "Upper Limb Exoskeleton Systems—Overview," in *Wearable Robotics: Systems and Applications*, Academic Press, 2020, pp. 1–22.

J. Rosen and **P. W. Ferguson**, Eds. *Wearable Robotics: Systems and Applications*, Academic Press, 2019.

C. Shin, **P. W. Ferguson**, S. A. Pedram, J. Ma, E. P. Dutson, and J. Rosen, "Autonomous Tissue Manipulation via Surgical Robot Using Learning Based Model Predictive Control," in *2019 Int. Conference on Robotics and Automation (ICRA)*, 2019, pp. 3875–3881.

P. W. Ferguson*, B. Dimapasoc*, Y. Shen, and J. Rosen, "Design of a Hand Exoskeleton for Use with Upper Limb Exoskeletons," in *4th Int. Symposium on Wearable Robotics (WeRob)*, Springer, 2018, pp. 276–280.

Y. Shen, **P. W. Ferguson**, J. Ma, and J. Rosen, "Upper Limb Wearable Exoskeleton Systems for Rehabilitation: State of the Art Review and a Case Study of the EXO-UL8 Dual-Arm Exoskeleton System," in *Wearable Technology in Medicine and Health Care*, Academic Press, 2018, pp. 71–90.

S. A. Pedram, **P. Ferguson**, J. Ma, E. Dutson, and J. Rosen, "Autonomous Suturing via Surgical Robot: An Algorithm for Optimal Selection of Needle Diameter, Shape, and Path," in *2017 IEEE Int. Conference on Robotics and Automation (ICRA)*, 2017, pp. 2391–2398.

CHAPTER 1

Hand Exoskeleton Background

The following chapter is largely excerpted from the book chapter: “Hand Exoskeleton Systems–Overview” published in *Wearable Robotics: Systems and Applications* [1].

1.1 The Need for Hand Exoskeletons

Since the creation of the MIT-Manus [2], robots used for rehabilitation of various physical conditions have widely been shown to be comparable to, and sometimes superior to, human physical therapists. These robots are used to replicate the physical therapy effort of one or more human therapists by applying forces/torques at different points along the body to stretch, passively move, assist in movement, or resist in the movement of targeted joints. There are, however, several important differences between physical therapy provided by a human and that provided by a robot. Whereas a human physical therapist cannot replicate the exact same motion repeatedly and will eventually tire, the robot can repeat motions precisely and indefinitely as long as power is provided. Additionally, a robot is capable of quantifying and recording information that may be relevant to guiding future therapy, such as but not limited to interaction forces and joint angles. Further, a robot can be designed to physically interact with the patient at more points than is possible for a single physical therapist, and therefore more completely guide movements. Challenges remain, though, in the mechanical design of said robots and in determining how they should be controlled to perform the most useful rehabilitation.

The first rehabilitation robots were built as “end-effector” type systems. An end-effector type rehabilitation robot is one that is grounded externally to the human body, and only interacts with the patient at the end-effector. These have been shown to be useful in rehabilitation of certain movements, but they have a major drawback. Namely, end-effector type systems control the configuration of the point where they attach, but do not specify the human joint angles that result in said configuration. As such, they can only provide limited, if any, assistance to specific joints. Additionally, in the context of hand rehabilitation robots, end-effector type systems generally require the arm to remain largely stationary and block the hand from being used to grasp physical objects.

The alternative is the “exoskeleton” type robot. Exoskeleton robots are characterized by attaching to and interacting with the user at multiple points. Oftentimes, they are constructed such that the motions of the robot will cause controlled motions of specific joints, and thus they are capable of assisting said joints in a more controlled manner than end-effector systems. With regards to hand exoskeletons, they are commonly designed to be grounded to (that is, the origin of each linkage is located at) the dorsum of the hand and leave the palm as unobstructed as possible. Therefore, the user can move their arm while wearing the system, and can grasp physical objects. The challenge of hand exoskeleton systems is in their compactness and complexity. Even simplified models of the human hand contain at least 21 *Degrees Of Freedom* (DoFs). Actuating all of these DoFs generally results in a bulky and overly complex system. As such, many different hand exoskeleton systems controlling different groups of DoFs using different mechanisms have been designed. The remainder of this chapter provides a general overview of the mechanisms, transmissions, actuators, sensors, and controls used in hand exoskeletons as well as a brief discussion of rehabilitation hand exoskeletons, and is excerpted from [1].

Fig. 1.1 provides a chronological overview of the characteristics of 40 hand exoskeletons found in the literature. The Y-axis categorizes systems by the number of independent active DoFs. Mechanically coupled DoFs are commonly found in hand exoskeleton systems and

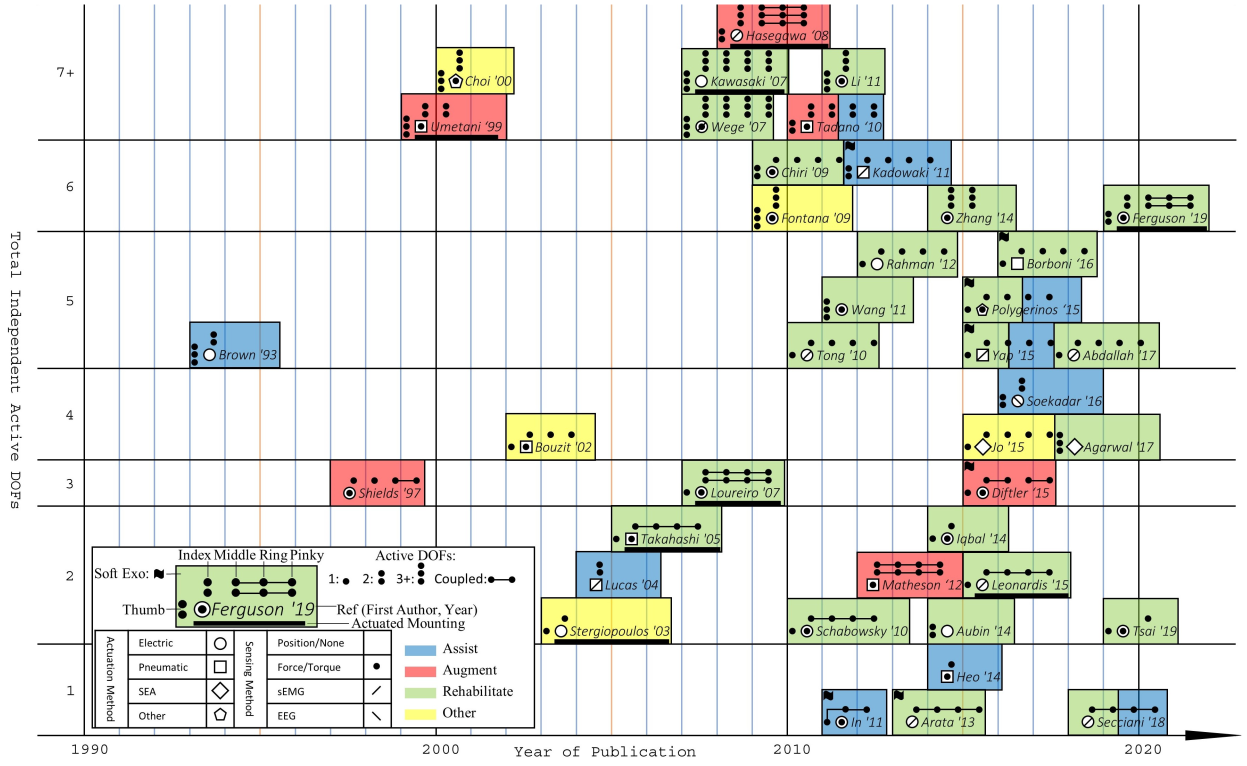

Figure 1.1: A graphic summary of hand exoskeletons in the literature [1].

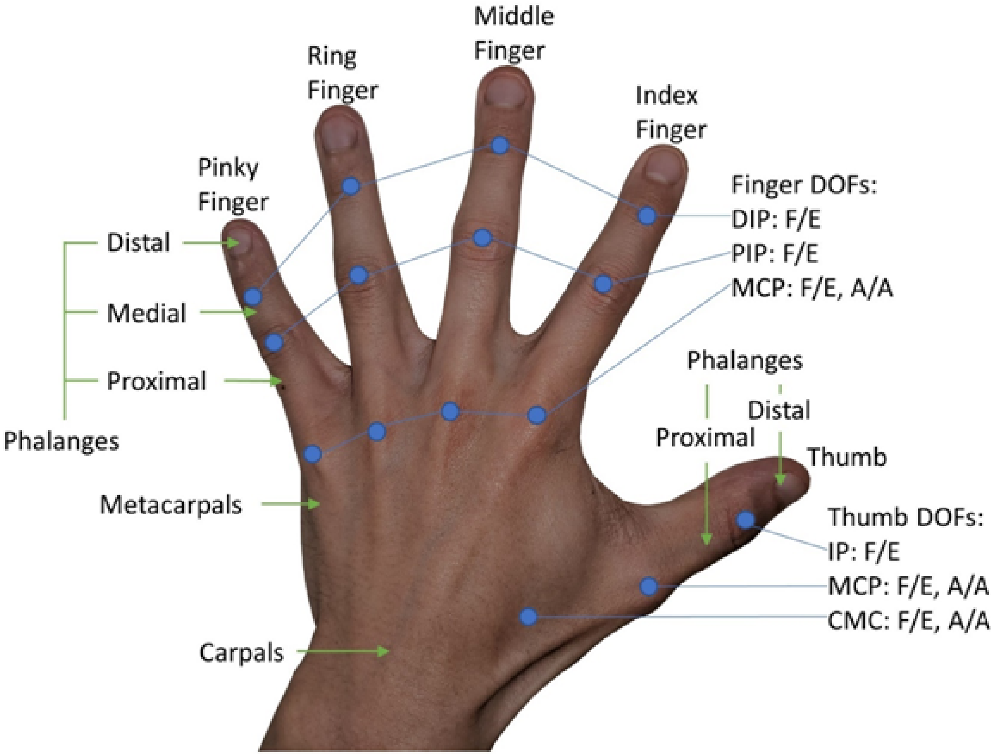

Figure 1.2: A simplified model of the hand. Bones are indicated by green, and joints in blue [1].

are indicated by thin lines between coupled DoFs. Note that only those shaded in green are systems designed for use in rehabilitation.

1.2 Mechanism

1.2.1 Degrees-of-Freedom

A simplified model of the hand that is commonly used for discussion of hand exoskeletons in shown in Fig. 1.2. Each of the four fingers, namely the index, middle, ring, and pinky fingers, are widely agreed upon to contain four DoFs. At the knuckle, or *MetaCarpoPhalangeal* (MCP) joint, each of the four fingers is capable of *Flexion/Extension* (F/E) as well as *Abduction/Adduction* (A/A). The four fingers are capable of two additional F/E motions each, at their respective *Proximal InterPhalangeal* (PIP) and *Distal InterPhalangeal* (DIP) joints.

The thumb is generally regarded as a more complex mechanism than the other digits, and kinematic models for its motion are still being refined [3]. Nonetheless, the prevailing model consists of five rotation axes [4], [5]. The *CarpoMetaCarpal* (CMC) and MCP joints of the thumb are each considered to be capable of F/E and A/A, whereas the *InTerPhalangeal* (ITP) joint is capable only of F/E. However, it should be noted that one of the most important movements of the thumb is that of *Opposition/Resposition* (O/R). O/R consists of rotation of the plane of F/E of the thumb about an axis through the CMC such that the finger pad of the thumb can touch that of the fingers. This motion occurs as a combination of the CMC and MCP joints of the thumb. The F/E and A/A motions of these joints consist of rotations about non-perpendicular and non-intersecting axes at each joint, which together can create the rotation of the thumb about it's long axis necessary for O/R [6], [7].

In total, there are 21 DoFs in this simplified model of the hand that ignores motion of the four finger metacarpals. Given the compact size of the hand, the required ability of the exoskeleton to rotate about hand joints without physically overlapping said joints, actuator size and mass, and increasing complexity of intent estimation and control algorithms with more DoFs, it is frequently impractical to actively control every joint. Instead, it is common practice to include passive DoFs. As such, it is necessary when designing a hand exoskeleton to identify which motions must be actuated and which can be left passive. This choice depends largely on application, however even within applications there is not a unanimous consensus as can be seen in the varying designs shown in Fig. 1.1.

In addition to passive joints, most hand exoskeletons also feature either underactuated or coupled joints. This occurs when multiple DoFs are actuated by a single actuator. In hand exoskeletons, this commonly occurs in three ways. The first consists of placing rigid connections between fingers at specific attachment locations such that separate fingers move together. The second method requires a differential or some other mechanism such that multiple DoFs are driven by a single actuator but without a set ratio between joint angles velocities. This method enables some devices to conform grasp shape to a variety of different objects even with a single actuator. These first two methods are indicated on Fig. 1.1 by thin lines between DoFs. The final method involves the use of gears, pulleys, or links such that separate DoFs actuate together with a fixed ratio of joint angle velocities. This last method is frequently used to control multiple F/E DoFs with a single actuator, and is not indicated in Fig. 1.1.

1.2.2 Topology

Various studies have classified the topology of hand exoskeleton mechanisms in different ways [8], [9]. This study attempts to classify topology by categorizing as matched axes, remote center of motion, redundant linkage, base-to-distal, or compliant. Similar categories have been proposed in the literature, although terminology differs. Fig. 1.3 contains example diagrams of each category.

In order for a hand exoskeleton properly control desired DoFs of the digits of the hand, it is necessary for actuation of the exoskeleton joints to cause predictable rotations of the joints of the human hand.

The most direct way to cause hand exoskeleton motion to predictably control DoFs of the hand is to place the axis of rotation of the exoskeleton joint coincident with that of the human joint as shown in Fig. 1.3a. Exoskeletons that do so are referred to here as matched axes exoskeletons. Although such a topology may initially present as simple, they are in practice difficult to achieve as placing the exoskeleton F/E joints coincident to those of the fingers requires the structure of the exoskeleton to be laterally adjacent to said fingers. Given that many grasps place the fingers in contact with each other, this topology is usually not feasible for multiple finger systems. It should be noted that in all systems studied A/A motions were achieved with a matched axes topology.

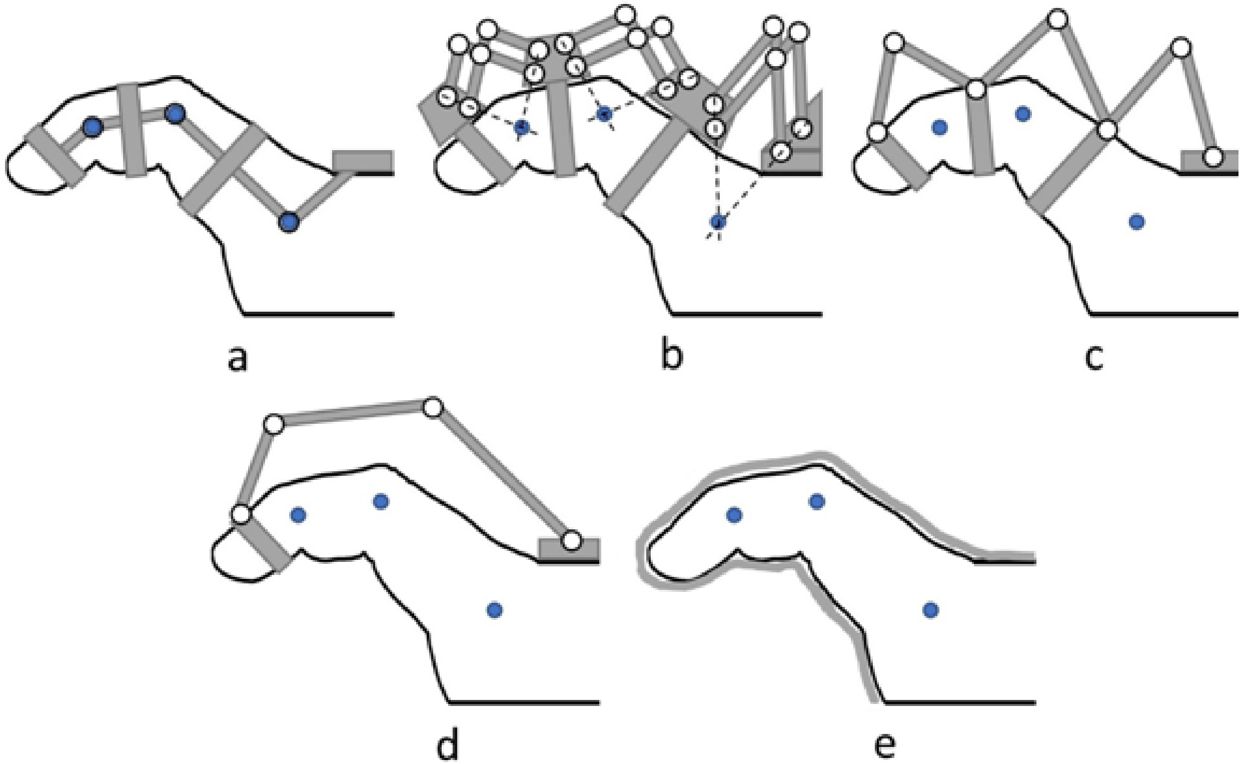

Figure 1.3: Example schematics of hand exoskeletons in each category. a) Matched axes, b) remote center of motion, c) redundant linkage, d) base-to-distal, and e) compliant [1].

An alternative method is for the mechanism of the exoskeleton to cause each link to rotate about remote centers of motion aligned with those of the finger joints as shown in Fig. 1.3b. There are several possible mechanisms to do this, and the problem has been analyzed in [10]. For hand exoskeletons, common mechanisms in this category include parallelogram mechanisms and circular-prismatic joints. These mechanisms can be low-profile depending on design. Exoskeletons that feature this topology generally connect to the segments of the hand immediately proximal and distal to each joint such that each exoskeleton joint is coupled to a biological joint.

A redundant linkage topology is another option to couple motion of a specific exoskeleton joint to a single hand joint. These systems also attach to the digit before and after each actuated hand joint, but feature additional linkages and joints between each attachment point as shown in Fig. 1.3c. These extra joints and linkages serve to turn the combined digit-exoskeleton system between adjacent attachment points into four-bar or other mechanisms with well-defined relations between exoskeleton and hand joint motions. The resulting mechanism is typically slightly larger than those that use a remote center of motion topology.

Base-to-distal topology exoskeletons relax the recommendation of coupling specific exoskeleton joints to specific hand joints. Instead, these systems connect a serial linkage from the exoskeleton base, typically the dorsum, to distal to the last actuated joint as shown in Fig. 1.3d. The connecting serial linkage effectively actuates the entire digit together, as opposed to at each joint. Although there is some variability between individuals, it has been shown that F/E of the PIP and DIP joints are in general coupled [11], and multiple studies have reported accurate estimation of finger joint angles based on this coupling. Foremost among the advantages of this topology are simplified design and the removal of required adjustment mechanisms for varying user digit segment lengths with proper selection of link lengths. However, this comes at the costs of larger mechanism size and, despite joint coupling, reduced controllability of the hand.

Compliant topology exoskeletons can appear similar to gloves, and do away with rigid joints altogether as shown in Fig. 1.3e. The actuation method or transmission is built into the exoskeleton such that there is minimal rigid structure. The structure of the exoskeleton bends with the actuated digits. These exoskeletons bring all the advantages and challenges of soft robots. Extra care must be taken such that forces are not applied inappropriately, as there are not rigid joints to guide torques and forces and thus the user's skeleton becomes the guiding structure.

A common requirement for the topologies of nearly all hand exoskeletons is an open palm. The purpose of this requirement is threefold. First, occupying the palm with the mechanism prevents grasp of, and interaction with, most objects. Second, placing the mechanism on the palm prevents full closure of the hand. Lastly, the ability to obtain tactile feedback is an instrumental part of the human hand. Any obstruction of the palmar side of the hand will reduce this ability, and thus have a negative impact on the user.

1.3 Actuation

All active exoskeleton systems, by definition, require at least one actuator. Requirements for these actuators differ by system and application, but common desirable characteristics are high force/torque, high actuation bandwidth, low mass, backdrivability, and easy and precise control. Figure 1.1 includes information on actuation method for each exoskeleton.

1.3.1 Electric Motors

Electric motors are the most common actuator used, and come in several varieties. While standard rotary motors make up the bulk of these systems, a significant number also use linear actuators. Electric motors provide the notable advantages of easy, precise, and high bandwidth actuation, but they in general have a lower power to mass ratio than their main competitor. Torque for electric motors can be easily increased, but at the expense of speed.

1.3.2 Pneumatic Actuators

Pneumatic actuators account for nearly all other hand exoskeleton systems. Different systems have incorporated pneumatics in different methods, including pneumatic cylinders, pneumatic muscle actuators, and soft elastomeric actuators. Pneumatics are characterized by high power to mass ratio, yet also create challenges in control. Additionally, pumps and/or compressed gas containers are required for their use.

1.3.3 Serial Elastic Actuators

A relatively small minority of hand exoskeletons feature serial elastic actuators (SEAs). This method of actuation typically features an electric motor driving a Bowden cable transmission ending in springs. Despite using electric motors, the addition of springs changes the characteristics of SEAs enough that they can be considered in a different category. By nature, SEAs provided advantages in safety and impact resistance. Additionally, the springs allow the implementation of highly accurate force control. However, SEAs also suffer from high power requirements, increased mechanical complexity, low actuation bandwidth, and low stiffness. A discussion of the use of SEAs in rehabilitation robotics is provided in [12].

1.3.4 Other Actuators

Other actuation methods have been implemented in the remaining few hand exoskeletons. These include hydraulic actuators, ultrasonic motors, and shape memory alloys among others.

1.4 Transmission

1.4.1 Direct Drive, Gear, or Linkage

The simplest and most direct way to transfer force/torque from the actuator to the joints of the hand is through direct drive, gears, or rigid links. With this type of transmission, the motor is typically placed on the dorsum or on the finger linkages themselves. While this reduces complexity, it also increases mass at the hand which is undesirable for many systems. Due to limitations in permissible motor size or mass, these systems usually have fewer actuators unless the structure of the exoskeleton is supported externally.

1.4.2 Bowden Cables

Bowden cable transmission systems offer an attractive alternative to direct drive, gear, or linkage transmission systems due to the ability to place the motor remotely. This option is particularly attractive for non-portable hand exoskeletons, as the motors can be moved to a stationary location to reduce inertia while still permitting the arm to be moved. However, Bowden cable transmissions suffer from friction, backlash, comparatively lower maximum force before breaking, and the sheathes exerting forces on the exoskeleton when moved. Nevertheless, they are a popular choice to reduce inertia of hand exoskeletons.

1.4.3 Tendon Driven

Another option is to use cables to mimic the functionality of the tendons of the hand. By attaching them at a distal point beyond a joint, and applying tension, they can cause joints to move in a way that closely matches biology. However, tendon transmissions are, in general, unidirectional. In order to achieve bidirectional actuation, a second cable, often from another actuator, must be attached to apply force in the opposite direction. Additionally, tendon transmissions can suffer from cable breakage and sometimes require complex routing. Nonetheless, as they apply force/torque across a digit and not just a joint, they are frequently used in soft exoskeleton gloves. They are often coupled with restorative springs.

1.4.4 Compliant Transmissions

Several other compliant transmissions have been proposed for hand exoskeletons, and theoretically any of the methods used in soft robotics [13] could be applied. Various methods using electric motors, pneumatics, and hydraulics have been tried. These transmissions simultaneously increase safety by absorbing impacts, and can reduce safety if unsafe forces are routed through the hand due to lack of exoskeleton structure.

1.4.5 Restorative Springs

Although a passive element, springs are used in most hand exoskeletons with otherwise unidirectional actuation. Frequently, they are coupled with either tendons or pneumatic cylinders that control only flexion or only extension in order to passively provide the other.

1.5 Sensing Method

In order for a hand exoskeleton to properly accomplish a task, it is necessary to prescribe an overarching strategy for how it is to be controlled. The inputs to this control strategy are the desired actions to perform. The desired action, in turn, is dictated by the state of the system and estimated intention of the user. There are a variety of sensors used to acquire this information, and some of the more common strategies are discussed.

1.5.1 Position Sensors

The vast majority of hand exoskeletons have some method of detecting the joint angles and/or the position of the various links with respect to the exoskeleton base. There are a variety of different choices to establish this information including encoders on the motors, encoders or potentiometers placed at joints, flex sensors, and linear variable differential transducers among others. Position sensors are required to obtain the physical configuration of the exoskeleton, and are therefore critical to many control strategies.

1.5.2 Force/Torque Sensors

Numerous applications require knowledge of the forces/torques experienced by the hand exoskeleton. This information can be used to enable admittance or force control, provide information on rehabilitation progress to a physical therapist, and for interactive use as a teleoperation or virtual reality haptic device among others. Inclusion of force/torque sensors are varied, with some systems omitting them, others building them into the fundamental structure of the device, and others placing them at human-robot interface locations.

1.5.3 Electromyography

Surface electromyography (sEMG) is a method for detecting the electrical activity in muscle [14]. In healthy individuals, these electrical signals accompany all movements. With sEMG used to detect these signals, a hand exoskeleton can generate trajectories with complementary movements. This ideally enables real-time control of an exoskeleton without requiring the user to exert forces or torques on the system, creating greater transparency. However, sEMG faces a variety of challenges as a method for intent estimation. Every time the system is donned/doffed, electrodes must be reattached, and changes in position will result in changes in detected electrical activity requiring recalibration. Additionally, there are challenges with using electrodes with hairy, dirty, or wet skin. Finally, the resolution of sEMG is relatively low and the number of electrodes used may be less than the number of active DoFs, and thus it is challenging to use to control a high DoF system.

1.5.4 Electroencephalography

Similar to sEMG, *electroencephalography* (EEG) is used to detect electrical biosignals. However, EEG is used to noninvasively detect brain signals, in the form of electrical activity, through the scalp. As with sEMG, EEG could be used to control a hand exoskeleton without applying forces/torques. Additionally, it can be used with users that do not have proper muscle functioning, such as victims of stroke or spinal cord injury. It has also been shown to be capable of controlling a variety of complex robotic systems, such as mobile or humanoid robots [15], [16]. Surface EEG suffers from many of the same challenges as sEMG, as well as low signal-to-noise ratios, significant required processing, and long reaction times.

1.6 Control

There exist several control strategies used by hand exoskeletons to correctly actuate the hand to accomplish tasks. A brief summary of some of the more common strategies are detailed below.

1.6.1 Passive Motion

Passive motion ignores the intention of the user entirely, and attempts to control the hand exoskeleton along a trajectory as if the user was not there. This strategy typically uses a position or velocity low-level controller. The passive motion can be used to test functionality of a device, or to bring the exoskeleton to a specific state, such as a neutral position for donning/doffing. However, the most significant application is as *continuous passive motion* (CPM) [17]. Applied in the initial stages after an injury or surgery, CPM can be effective in preventing the development of stiffness. However, it has been shown that interactive treatment with a rehabilitation robot can provide benefits that CPM cannot [18]. For this reason, as well as for applications outside of rehabilitation, active intent estimation is necessary.

1.6.2 Master/Slave System

The first active hand exoskeletons were developed as haptic devices and data gloves to control other robotic systems. It is therefore logical that one strategy for controlling a hand exoskeleton is to use it as the slave of a master/slave system. Of particular interest is the use of two hand gloves, one a master system and one a slave hand exoskeleton system, where the movements of the hand in the master system are mirrored to the other by the hand exoskeleton. This is a commonly proposed technique for bimanual rehabilitation of stroke, and has been shown to be effective [19]–[21].

1.6.3 Biosignal Control

This category consists of strategies for controlling the exoskeleton based upon biological signals measured from the body through EMG, EEG, electrooculogram (EOG), or other methods. Depending on the sensing method, the biological signals can be obtained even from users who have impaired motor functioning. As such, biological control strategies are primary candidates for real-time control of assistive exoskeletal devices, although they are also not uncommon for rehabilitation exoskeletons. The challenge of biosignal control strategies is how to convert the biological signals to control inputs, as there is rarely unambiguous or independent mapping between the measured signals and the DoFs to be controlled. There are also options of whether the signals are used as binary switches [22] or for proportional control [23].

1.6.4 Force-Based Strategies

Force-based control strategies are those that control the hand exoskeleton based upon the interaction forces and torques applied between the human hand and exoskeleton. These include low level control of impedance, admittance and force. Further, these strategies can be divided into assistive strategies that help the user move, and resistive strategies that hinder movement. Assistive force-based control strategies are common across all hand exoskeleton applications. Resistive strategies are found primarily in systems made as haptic devices (to simulate virtual objects it is necessary to resist movements of the hand that would penetrate said objects), as well as rehabilitation devices for the latter stages of physical therapy.

1.7 Rehabilitation Hand Exoskeletons

A wide variety of hand exoskeletons have been developed for rehabilitation and presented in the literature. The most important requirement of hand exoskeletons for rehabilitation is the ability to enable the exercises required for physical therapy. These systems do not, by nature, need to be portable. This has enabled the development of extremely complex hand exoskeletons to enable independent control of many movements, although this complexity is not ubiquitous. Indeed, the two hand exoskeletons with greater than 15 active DoFs, as seen in Fig. 1.1, were developed more than a decade ago. Although these systems can reproduce almost any hand motion, the complexity also equates to bulkiness and introduces greater challenges for control and intent estimation. Many recent designs have instead limited the number of independent active DoFs, and therefore enable smaller, sleeker, and potentially less expensive designs that still permit the majority of motions required for rehabilitation. Rehabilitation exoskeletons are also generally designed not to be used by a single patient, but by a variety of users. As such, the ability to accommodate hands of different sizes and impairments is a common requirement.

The goal of hand rehabilitation exoskeletons is to restore, or at least improve, the ability of the patient to use the hand without the exoskeleton. This is done to enable the patient to resume normal *Activities of Daily Living* (ADLs) without the need to constantly wear an assistive device. Many ADLs involving the hand are reach-and-grasp tasks that also require movement of the arms. As it is not uncommon for patients with hand impairments to also have impairments in the arm, it is a logical step to design a single exoskeleton combining both a multi-DoF hand exoskeleton and a full arm exoskeleton. However, there are relatively few examples of this in the literature. Instead, many upper-limb exoskeletons with hand modules actuate just one DoF to permit a single simple grasp.

There are several challenges limiting the development of arm exoskeletons with multi-DoF hand modules. Typically, the more DoFs a hand exoskeleton can actuate, the more complex and heavier the system becomes. This creates problems if the hand exoskeleton is attached to the distal end of an upper limb system, as it increases mass and inertia. Additionally, power and control signals for the hand must be routed in such a way that does not interfere with motion of the arm. Though feasible, this becomes more difficult with more hand DoFs.

Furthermore, the combined human arm and hand system possesses dozens of DoFs. As the number of DoFs of the combined exoskeleton system increases, questions of intent estimation and redundancy resolution become more difficult to answer.

A common addition to rehabilitation robotic systems is a virtual reality or computer game environment [24]–[29]. These games are intended to engage the patient and keep them motivated to perform greater repetitions of tasks, increase possible training session durations, and potentially reduce the need for supervision by a physical therapist. The tasks are designed to require motions similar to those normally performed during physical therapy sessions. They have been proven as effective strategies for rehabilitation in multiple studies.

CHAPTER 2

The Need for a New Hand Exoskeleton

The following chapter is partially excerpted from the conference paper: “Design of a Hand Exoskeleton for Use with Upper Limb Exoskeletons” published in *4th International Symposium on Wearable Robotics (WeRob2018)* co-first authored with Brando Dimapasoc [30].

2.1 Introduction

For decades, stroke has been one of the leading diseases that causes long-term disabilities [31]. Researchers and physical therapists have been working on exoskeleton-like robots to help patients regain capabilities post stroke. The upper limb is an area of focus, but research has focused mainly on individual parts, either arm or hand [32]–[34]. Although there is a need for rehabilitating the capabilities in reach and grasp ADLs, only a handful of systems have a working combination of both arm and hand [29], [35]. Even fewer combination systems actively actuate multiple DOFs across multiple fingers [36]. Based on the upper limb exoskeletons EXO-UL8 [37] and BLUE SABINO [38], a reconfigurable hand exoskeleton is designed.

2.2 Methods

2.2.1 Design Requirements

The following requirements were formulated for a rehabilitation hand exoskeleton that attaches to an arm exoskeleton:

1. Low Mass: Mass at the hand must be minimized to reduce required torque of the upper limb exoskeleton.
2. Torque: The torque capabilities of the exoskeleton must be sufficiently large to actuate the hand.
3. Workspace: The workspace of the exoskeleton must contain the workspace of the human hand.
4. Grasp: It must be able to actuate a variety of grasps.
5. Open Palm: It must leave the palm and fingers unoccupied to permit interaction with physical objects.
6. Unisize: It must fit 95% of the general population.

2.2.2 Actuation Method

For the low mass and torque requirements, a Bowden cable transmission system with brushed DC motors was chosen. The cable transmission enabled remote location of the motor pack, reducing mass at the hand. It also allowed use of over-sized actuators with sufficient torque for hand rehabilitation.

2.2.3 Basic Topology:

Workspace, grasp, open palm, and unisize requirements are satisfied by a reconfigurable design topology of three 3R planar serial linkages that attach on the dorsal side of the hand to the distal phalanges. Three linkages are used as 95% of human grasps are achievable with a thumb and two fingers [39]. The topology allows a one-size-fits-all design that neither requires adjustment for different finger lengths nor impedes grasping physical objects. The third joint is made passive to decrease complexity and inertia compared to an active joint. Due to the link lengths, this joint mainly relates to orientation. A passive rotational joint added at the end-effector of each finger linkage permits slight adduction/abduction to improve comfort and allow more natural movement. Bending beam load cells are used as the structure of the first link (L_1) of the thumb linkage and second link (L_2) of the finger linkages, enabling admittance control.

The linkages are reconfigurable to enable a variety of grasps. The first linkage attaches from above the CPC joint to the distal phalanx of the thumb. The plane of the workspace of this linkage is adjustable via rotation around the CPC. The second and third linkages connect from above the MCP joints to the distal phalanges of the fingers. The origin of these linkages is adjustable for different hand widths or to place them in plane with different fingers. The distal end of the second and third linkage feature interchangeable customizable 3D-printed finger attachments that enable different sets of fingers to be actuated by each linkage. Notable configurations include 1-1-3 (thumb, index, middle+ring+little) and 1-2-2 (thumb, index+middle, ring+little). The 1-1-3 configuration is shown for a set of representative hand positions in Fig. 2.1. To account for motion of the little finger relative to the ring finger, a passive slider mechanism connects the finger attachment for the little finger to the third linkage.

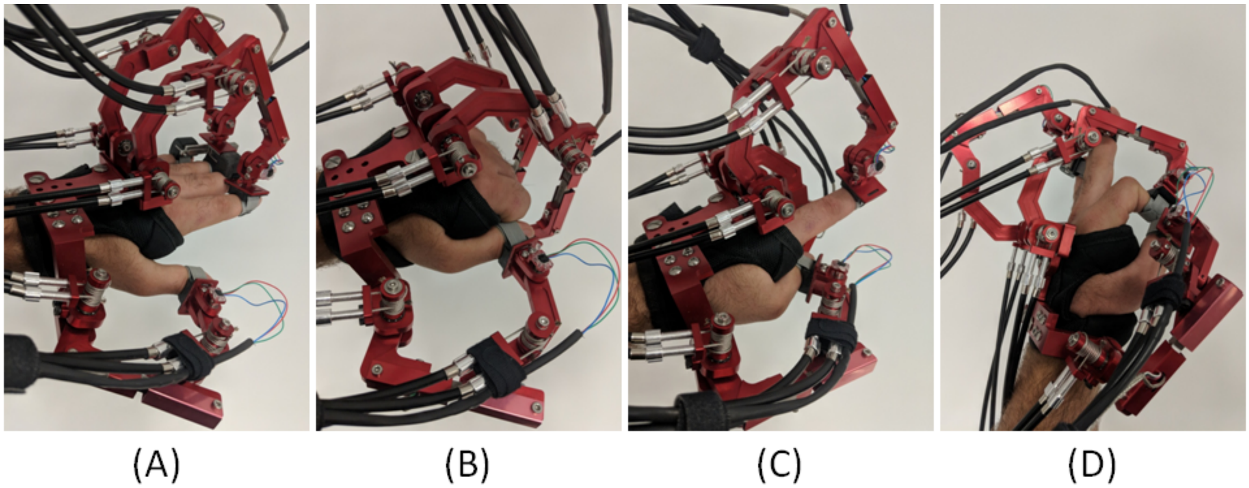

Figure 2.1: 1-1-3 Configuration shown with (A): Open Hand, (B): Closed Fist, (C): Pointing, (D): Pincer Grasp.

2.2.4 Link Length Optimization:

To satisfy the unisize requirement, the link lengths were chosen via a brute force optimization algorithm considering fingers in the 95th percentile for length.

The lengths of L_1 of the thumb linkage and L_2 of the finger linkages were set to 8.9cm due to the length of the bending beam load cells. For each linkage, the remaining link lengths were varied across a reasonable range. Each combination, L, of potential link lengths L_1, L_2, and L_3, was checked for kinematic feasibility. Forward and inverse kinematics were used to verify that the linkage could correctly attach to the tip of the distal phalanx of the appropriate finger at all combinations of joint angles (θ_1,θ_2,θ_3) within the workspace with 3° resolution. To correctly attach, L_3 must be capable of connecting perpendicularly to the dorsal side of the distal phalanx, and the joints of the linkage must not physically touch or cross through the finger.

A design score, J, was calculated for each L based on mechanism isotropy and link length. Mechanism isotropy (ISO), a function of the joint angles is a measure of kinematic performance. It is defined in (2.1) as the ratio of the min (λ_{min}) and max (λ_{max}) eigenvalue of the Jacobian matrix.

$$ISO(\theta_1, \theta_2, \theta_3) = \frac{\lambda_{min}}{\lambda_{max}} \in (0, 1) \tag{2.1}$$

A value of 0 indicates singularity while a value of 1 means the end effector can move equally well in all directions.

Mechanism isotropy is calculated for each set of joint angles previously mentioned. To account for varying densities of the end effector location in these sets, the finger workspace area is discretized into a grid of cells, K, and the isotropy is averaged for each cell. Summing the average isotropy of the cells provides an indication of the kinematic capabilities of the mechanism across the entire workspace. It is desirable for the mechanism to avoid singular or near-singular configuration within the workspace of the finger. Therefore, J of each L is proportional to both overall performance (sum of ISO) and to worst-case performance (minimum ISO value calculated).

As mechanical isotropy tends to reward longer link lengths, but it is desirable to keep size and mass of the mechanism low, an additional term is included in the J score to reward shorter designs. This was accomplished by making J inversely proportional to the sum of the link lengths raised to a hyperparameter, A, as shown in Equation (2.2). A prototype with adjustable link lengths was used to experimentally verify the design produced by a variety of A. Based on this verification, link lengths were chosen for each linkage.

$$J = \frac{\Sigma_K ISO(\theta_1, \theta_2, \theta_3) * MIN_K(ISO(\theta_1, \theta_2, \theta_3))}{(L_1 + L_2 + L_3)^A} \tag{2.2}$$

The results of the optimization are illustrated for the linkage that connects to the index finger in Fig. 2.2.

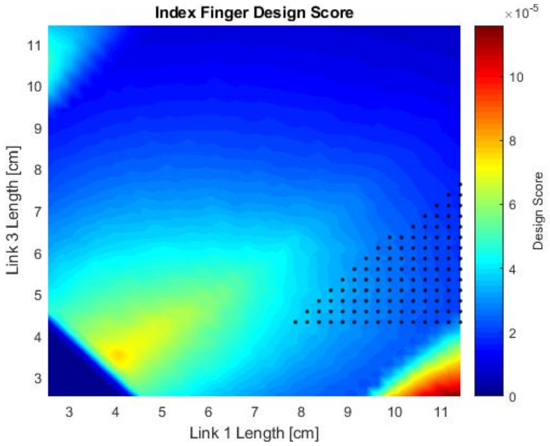

Figure 2.2: Optimization results for the linkage connecting to the index finger for A=5. Dots represent kinematically valid combinations of L_1 and L_3 for L_2=8.9cm. Set $L_1 \geq 4.4$cm due to minimum axes size.

2.3 Challenges

The above presented design was the first generation hand exoskeleton for attachment to the BLUE Sabino and EXO-UL8, and was mechanically designed by Brando Dimapasoc. It is multi-fingered, multi-DoF, reconfigurable, and designed to attach to a full-arm exoskeleton. Additionally, the link lengths were determined by optimization to maximize mechanism isotropy and minimize footprint for the huge majority of the population. However, preliminary integrated testing with the actuated system revealed numerous issues that prevented it from being applied and required modification.

2.3.1 Thumb Opposition/Reposition

A primary issue with the first generation hand was the inability for A/A or O/R of the thumbs. The A/A angle could be adjusted, and O/R was locked in a mostly reposed position. It was observed that very few objects could be grasped and grasping in general was uncomfortable. Most grasps require some degree of opposition [40], but the amount varies between grasps and within the trajectory of a single grasp. Further, stroke patients with spasticity of the hand have increased tone that can interfere with voluntary O/R. In order to enable grasping of a wider range of objects, and better meet the Grasp requirement, active O/R was deemed to be needed.

2.3.2 Motors and Transmission

The motor combination for the system was created by Maxon Motors (`https://www.maxongroup.us`) consisting of a 3-watt brushed DC motor (part 118638), 275:1 planetary gearhead with maximum 0.3 Nm continuous torque (part 110316), and 256 counts per turn quadrature encoder (part 323054). In system testing, these motors had been mounted with direct drive on the 3D-printed prototype. During integrated testing the motors were found to be too weak to move the fingers when actuating remotely through the Bowden cable transmission, and could be passively ignored by a wearer. Further, while the steel cables used were of both sufficient strength and flexibility, the sheathes for the Bowden cables were far too stiff to bending. Having been adapted from bicycle brake cables, the sheathes featured both an internal steel spring and external plastic coating. The result was effectively 6-DoF springs that continually exerted forces to restore the exoskeleton finger linkages to an equilibrium position. These exerted forces were nonlinearly related to both relative placement of the motor pack to the hand, and on the joint angles of the finger linkages. Thus, they would apply significant forces between the motor packs and the hand, forces that would have to be compensated by the upper limb exoskeleton that the system mounted to. Additionally, the cables connecting to the second joint of each linkage applied torques about the first joints, and were stiff enough to prevent the motors from moving the linkages outside of a limited range of motion. As such, it was determined that significantly stronger motors and more flexible Bowden cable sheathes were required to meet the Torque and Workspace requirements. Further, care must be taken in routing the Bowden cables of the second joints such that restoring forces do not primarily act perpendicularly to the moment arm between their termination points and the first joints.

2.3.3 Additional Force Sensors

Each linkage contained a single LBB200 bending-beam load cell from Futek (`https://www.futek.com`) integrated in the second link to detect user intention to flex/extend. As the third joint was passive, it was assumed that forces could only be applied on the final link parallel to the link (perpendicular to the distal phalanx) and that F/E torques could not be applied to or be applied by the finger. However, this assumption was inaccurate; forces and torques can be transmitted between the finger and the attachments. Depending on link configuration, these transmitted forces could be misread by the load cell to cause flexion when extension was desired, or vice-versa. It was determined that two force sensors were needed for each linkage, one for each active DoF. Further, to only read the desired forces, single point load cells were to be used.

2.3.4 Link Length Optimization and Topology

The first generation hand exoskeleton did use a link length optimization algorithm that gave feasible results. However, constraints were included that were not necessary. An 8.9cm minimum second link length was included to account for the force sensors. Force sensors that were less than half as long were found, significantly relieving the constraint on second link length. Additionally, the base-to-distal topology had been selected such that the entire linkages were behind the hand. This required the algorithm to disqualify link length combinations that resulted in planar overlap between the exoskeleton and biological joints anywhere within the workspace. Also, it enforced a minimum third link length for there to be a mechanically feasible third joint. This nonzero third link length, combined with a passive third joint, meant that wearers had a very large workspace they could reach even when both active joints were locked. This effectively removed the ability to control the fingers accurately. However, if a reconfigurable 3 linkage topology with two finger groups is used, it is not mandated that the linkage be purely dorsal to the hand. Indeed, the linkages can run lateral to the thumb, index, and pinky respectively such that there is no minimal third link length and no joint interference is possible. This allows setting the third link length to zero, which reduced the play due to passive third link to only orientation. However, if distal phalanx position is locked, the additional kinematic constraints of the human fingers largely eliminate the ability to change orientation as well.

In addition to changing the force sensors and topology to remove constaints on the link length optimization algorithm, it was judged that the algorithm itself was not physically justified. Specifically, the inclusion of the hyperparameter A reduced physical meaning of the denominator and permitted tuning of Equation (2.2) to give a wide range of results that mostly just reflected the designer's judgement. Even then, as seen in Fig. 2.2, the optimal design selected had a much lower score than options with longer L_1 and shorter L_3 that were only excluded due to the above mentioned constraint on L_3. Additionally, the algorithm did not consider small hands in the optimization, but there are link lengths sets that work for larger hands that do not work for small hands. As such, the link length optimization needed to be redesigned to be physically justified and to check kinematic feasibility for all hands targeted.

2.3.5 Electronics and Control Hardware

In system testing, the quadrature encoders in the motor combinations were not tested, and instead potentiometers had been used to measure joint angles. Upon assembly with the machined parts, it was found that the quadrature encoders could not be read by the NI myRIO that had been intended for use as the controller. While the myRIO does have quadrature encoder readers, they were limited in read rate to a small fraction of what was needed for the pulse trains created by the selected encoders at nominal motor speed. Additionally, the myRIO was not sufficiently fast enough to read all sensors, process the control loop, and send motor commands at a sufficient rate ($\gg$100 cycles/second). These reasons, combined with a desire to not use LabView, necessitated that alternate electronics and control hardware be found.

2.3.6 Abduction/Adduction of Finger Linkages

In order to reduce the distance between the back of the hand and first F/E joint of the finger linkages, which in turn reduced the link lengths, A/A joints of finger joints that align with the biological A/A joints were omitted. Instead, passive joints with axis of rotation parallel to the distal phalanges were added for the finger linkages. While these joints did enable abduction/adduction-like motion, the range of motion was limited and centered about the linkage. Additionally, the A/A motions were coupled with rotation of the fingers, which is not desirable as it either requires twisting the fingers or slipping in the attachments. It was judged that this was not a beneficial trade-off, and that A/A joints aligned with the biological joints should be used.

2.3.7 Attachment to Palm

In testing the first generation hand exoskeleton with motors, it was found that the cloth brace used to attach the exoskeleton to the palm was not sufficient. Even when tightened uncomfortably tight, there was significant play in the connection. As such, when the exoskeleton attempted to apply assistive or resistive forces to the fingertips, the palm moved with respect to the base of the exoskeleton as well. Further, the brace used an integrated hook-and-loop strap to secure, and the strap was observed to wear down quickly. An alternative attachment method that was more secure but still satisfied the Open Palm requirement and would not prohibit donning by a user with spasticity in the hand was sought.

2.4 Conclusion

The first generation rehabilitation hand exoskeleton developed to attach to the BLUE SABINO and EXO-UL8 contained numerous excellent design features that educated and were inherited by subsequent designs. These included, but are not limited to, the reconfigurable three linkages, remote actuation with Bowden cable transmission, use of a base-to-distal topology with a link length optimization algorithm, number of active DOFs, a passive pinky-slider mechanism, and use of non-contact magnetic rotary sensors for passive joints. However, the integrated system suffered from a number of challenges that together required a major redesign that resulted in the “Opposable Thumb Hand Exoskeleton for Rehabilitation” or “OTHER Hand” Exoskeleton.

CHAPTER 3

Development of the OTHER Hand Exoskeleton

Given the challenges and issues observed in the first-generation hand exoskeleton, a near-complete redesign resulted in the development of the *Opposable Thumb Hand Exoskeleton for Rehabilitation* (OTHER Hand). The new system sought to solve the shortcomings of the previous, while expanding on the successes. The OTHER Hand still had the same high-level design requirements of unisize, torque, workspace, grasp, open palm, and low mass. However, a series of novel design choices not found in the literature were made to achieve the requirements. The system has been completed and is fully functional.

3.1 Reconfigurable Topology

As with the first-generation, the workspace, grasp, open palm, and unisize requirements are addressed by a reconfigurable base-to-distal topology of three serial linkages that attach from the dorsal side of the hand to the distal phalanges. Three linkages are used as 95% of human grasps are achievable with a thumb and two fingers [39], and 100% of standard grasps can be accomplished with three or fewer “virtual fingers” [40].

Each finger linkage consists of four serial DoFs as shown in Fig. 3.1. The first joint of each of the two finger linkages passively allows A/A motion. This DoF can be locked in the neutral A/A if desired. When unlocked, the range of motion is 25° from neutral towards abduction. The remaining joints are all oriented for F/E of the associated finger(s), with the second and third joints actuated and the fourth passive. The second joint includes

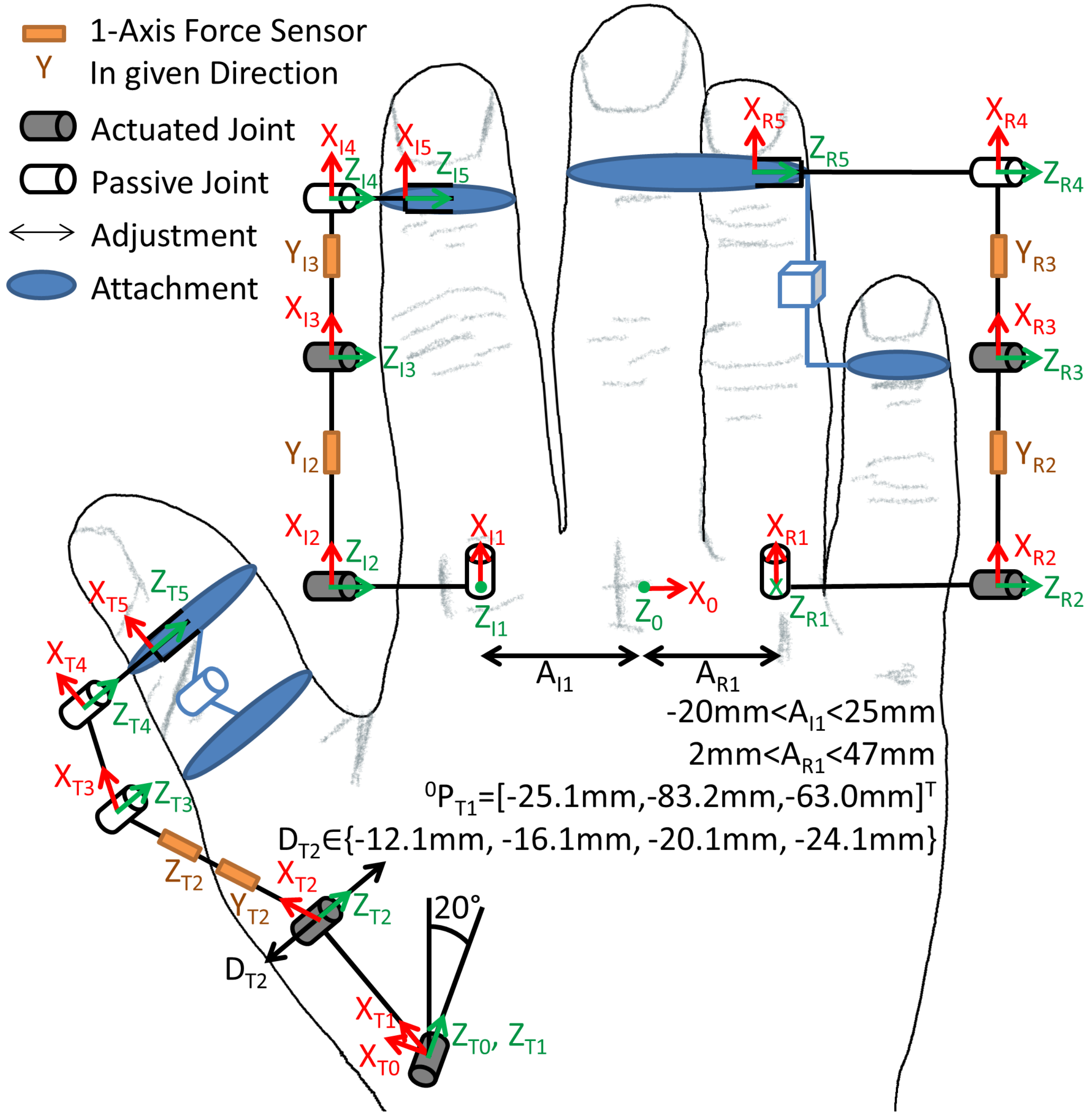

Figure 3.1: Kinematics of the right OTHER Hand.

physical end-stops to prevent near-singular configurations. The fourth joint is selected to have zero link length. Together, each linkage passively allows A/A, actuates F/E to control distal phalanx position, and passively allows adjustment of orientation of the finger tip due to F/E. However, with positions specified, the kinematic constraints of the fingers largely prevent changing of orientation of the distal phalanges. The linkage that connects to the pinky finger features a passive "pinky-slider" mechanism to accommodate the pinky's relative motion when flexing from an open palm to a fist. The fourth joint is selected to have zero link length. Together, each linkage passively allows A/A, actuates F/E to control distal phalanx position, and passively allows adjustment of orientation of the finger tip due to F/E. However, with positions specified, the kinematic constraints of the fingers largely prevent changing of orientation of the distal phalanges. The linkage that connects to the pinky finger features a passive "pinky-slider" mechanism to accommodate the pinky's relative motion when flexing from an open palm to a fist.

The thumb linkage also consists of four serial DoFs, with the first approximating O/R of the thumb and the remaining in the F/E plane. The first two joints are actuated, while the distal two are passive. Again, the final link has zero link length so that it only accommodates orientation changes, and the second to last link has physical end-stops to prevent near singular configurations. Although this underconstrains both the position and orientation of the thumb tip in the F/E plane, physical experiments verified that negligible passive motion is permitted due to the additional kinematic constraints imposed by the anatomy of the thumb.

Fig. 3.1 shows the kinematics of the right OTHER Hand. The *Modified Denavit-Hartenberg* (DH) parameters and joint *Ranges Of Motion* (ROMs) are provided in Table 3.1. ROMs are defined with zero positions given by DH parameters, except θ_{I1} and θ_{R1} are 0° when A/A is neutral. Positive angles are defined for abduction, flexion, and opposition.

Inherited from the first-generation system, a key feature of the OTHER Hand is reconfigurability of the linkages. The two finger linkages control all four fingers. One of the finger linkages is designed to always attach to the index finger, while the other always attaches to the ring and pinky fingers. Depending on which interchangeable finger attachments are used, the middle finger can be grouped with either linkage. This enables two important configurations, denoted as 1-1-3 (thumb, index, middle+ring+pinky) as shown in Fig. 3.1, and

Table 3.1: Modified DH Parameters and ROM for the right OTHER Hand.

i	a_{i-1}	α_{i-1}	d_i	θ_i	θ_i ROM
$T1$	0	0	0	θ_{T1}	-20.7° — 236.8°
$T2$	31.9 mm	60°	D_{T2}	θ_{T2}	-19.3° — 206.8°
$T3$	83 mm	0	-2.5 mm	θ_{T3}	6.1° — 150°
$T4$	40 mm	0	0	θ_{T4}	0° — 360°
$T5$	0	0	24.1 mm	0	N/A
$I1$	A_{I1}	0	0	θ_{I1}	0° — 25°
$I2$	0	90°	-14.2 mm	θ_{I2}	-25.7° — 101.8°
$I3$	99 mm	0	-6.5 mm	θ_{I3}	3.4° — 173.6°
$I4$	40 mm	0	0	θ_{I4}	0° — 360°
$I5$	0	0	20.7 mm	0	N/A
$R1$	A_{R1}	180°	0	θ_{R1}	0° — 25°
$R2$	0	-90°	28.2 mm	θ_{R2}	-44.5° — 101.8°
$R3$	103 mm	0	6.5 mm	θ_{R3}	3.4° — 173.6°
$R4$	41 mm	0	0	θ_{R4}	0° — 360°
$R5$	0	0	-40.2 mm	0	N/A

1-2-2 (thumb, index+middle, ring+pinky). Between the two configurations and the pinky slider mechanism, only grasps that require independent A/A motion of the pinky finger are prohibited. Such grasps are used during less than 6% of the time spent in daily household tasks [41].

3.2 Opposable Thumb

3.2.1 Motivation

The original exoskeleton prototype demonstrated that the 3R serial linkage for F/E permitted too few grasps for ADLs. Thus, to better satisfy the grasp requirement, an additional DoF was added.

As the OTHER Hand is designed with a base-to-distal topology, the exoskeleton cannot individually control A/A of the MCP and CMC. Instead, the added DoF should control the A/A or O/R of the entire thumb. These two motions for the thumb each have multiple differing definitions in the literature. For clarity, we identify A/A as motion of the thumb tip away from/towards the plane of the palm without change in orientation of the plane of the thumbnail. O/R is defined as the circumduction of the thumb such that the plane of the thumbnail changes, with full opposition when the thumbnail is parallel to the frontal plane of the palm, and full reposition when the entire thumb is along the frontal plane of the palm. As described in [42], this motion is a complex combination of F/E, A/A, and rotation about the longitudinal thumb axis that is driven by thenar muscles. It was determined that the ability to actuate O/R motions was of the highest priority due to the importance of opposition in grasping. Indeed, it has been argued that "thumb opposition is required for all useful prehension" [43], and it is widely accepted that having opposable thumbs is what enables humans (and more broadly, primates) to grasp objects and use tools. It should be noted however, that although O/R motions are largely responsible for selecting between different grasp types (e.g. cylindrical versus lateral), A/A motions allow some fine tuning within grasp types (e.g. opposing the thumb to the index finger versus opposing the thumb to the pinky finger). Additionally, it should be noted that abduction is almost only useful when combined with opposition.

3.2.2 Desired Axis

Mechanically, the prevailing kinematic model of the thumb places non-orthogonal, non-intersecting DoFs for A/A and F/E at each of the CMC and MCP joints, and a F/E DoF at the ITP joint as seen in [4], [44]. However, the exact kinematics of the thumb are still an active area of research, and new models continue to be proposed [3]. As the OTHER Hand uses a base-to-distal topology, the configuration of the MCP joint is less relevant than those of the CMC and ITP. To reflect this, the exoskeleton was designed based on an alternate simplified model of the thumb, as was done in [45] and discussed in [46] as the "surgeons" method, which places a spherical joint at the CMC joint and only F/E at the MCP and ITP joints. Through visual inspection of thumb motions, it was approximated that O/R motions

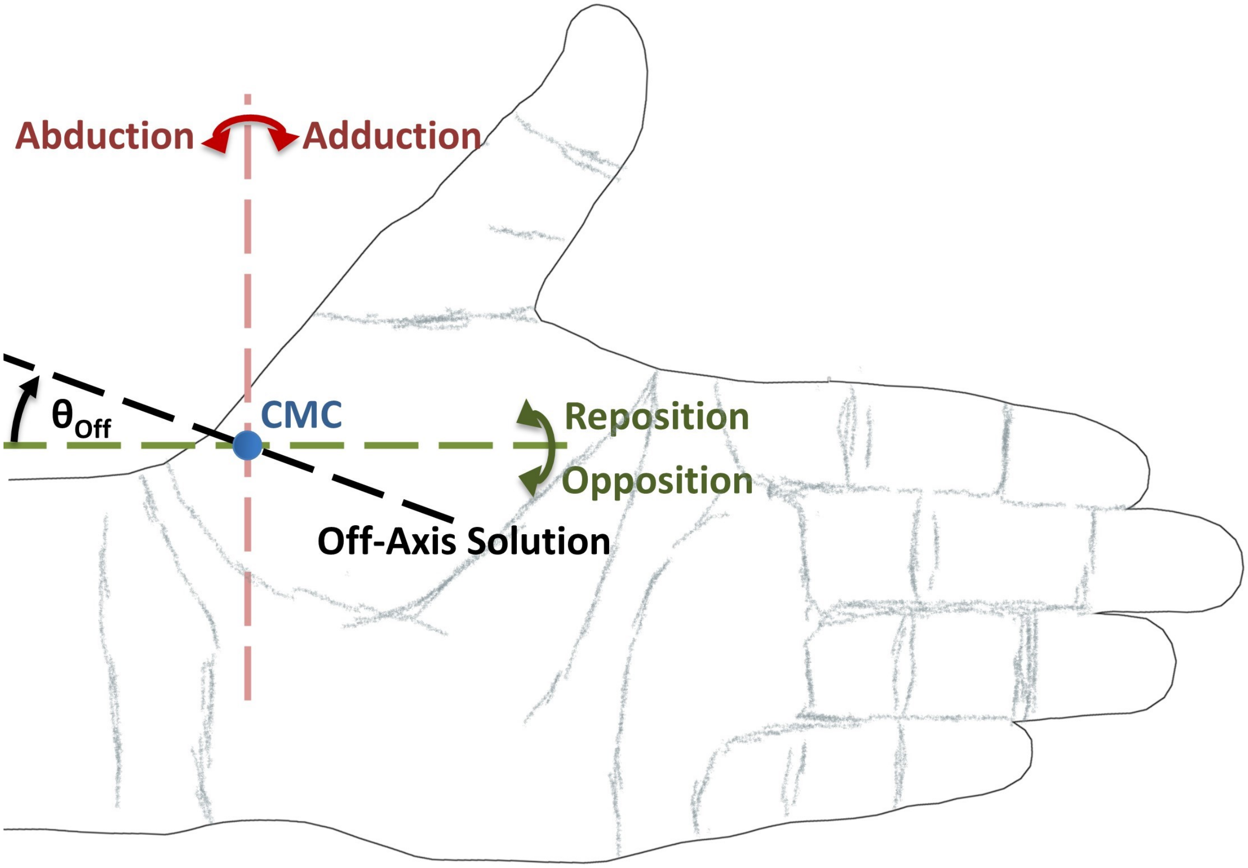

Figure 3.2: Axes for A/A (red) and O/R (green) of the thumb for the CMC (blue) modeled as a spherical joint. The off-axis DoF displayed in black.

of the thumb can be obtained by rotation about a single axis through the CMC, parallel to the forearm when the wrist is neutral in F/E and radial/ulnar deviation as shown in Fig. 3.2. A/A motions were found to be approximated by rotation about a perpendicular axis through the CMC that also lies in the plane of the palm when all fingers are extended.

3.2.3 Designs in the Literature

While many hand exoskeletons in the literature include a thumb mechanism, most of them are only actuated in F/E. Of the remainders, the majority control A/A motions (as shown in Fig. 3.2) [51]–[57]. This is attributed to the ease of design of a DoF for A/A as the axis points out of the hand. It should be noted that the configuration of the thumb of

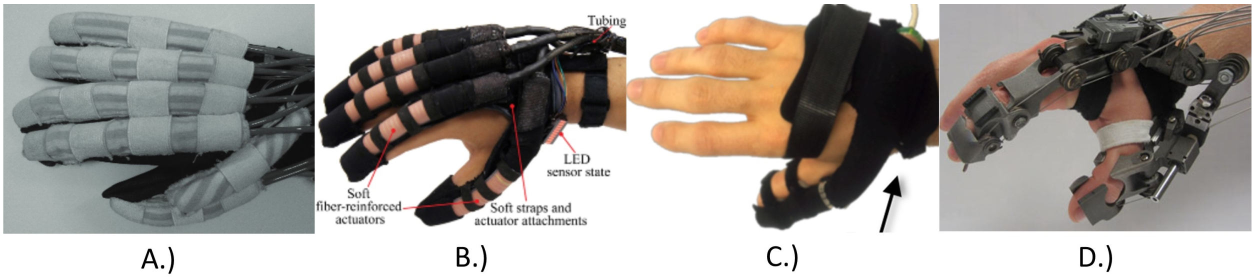

Figure 3.3: Hand exoskeletons in the literature capable of actuating O/R. A.) Kadowaki et al. [47], B.) Polygerinos et al. [48], C.) Maeder-York et al. [49], D.) HX [50].

these systems lock in varying degrees of opposition for grasping, but do not allow for active changing of said O/R degree. As such, each system may allow reposition grasps/postures (such as the lateral pinch or platform push) or opposition grasps (such as the pulp pinch or spherical grasp), but generally cannot do both and cannot be used to retrain the motions of O/R. Design of a mechanism for O/R (as shown in Fig. 3.2) is notably more challenging due to the proximity of the axis of rotation with the forearm. Additionally, radial deviation of the wrist moves the axis within the forearm, prohibiting any mechanism placed along the axis for systems that do not constrain wrist deviation.

While many hand exoskeletons in the literature include a thumb mechanism, most of them are only actuated in F/E. Of the remainders, the majority control A/A motions [51]–[57]. This is attributed to the ease of design of a DoF for A/A as the axis sticks out of the hand. Design of a mechanism for O/R is notably more challenging due to the proximity of the axis of rotation with the forearm which makes placement of a mechanism along that axis nearly impossible. Additionally, radial deviation of the wrist places the axis within the forearm which prohibits any mechanism placed along the axis for systems that do not constrain wrist deviation.

Several hand exoskeletons with O/R motions of the thumb have been developed. They are generally either soft robot gloves or rigid robots with remote center of motion mechanisms. The systems featuring O/R found in the literature are shown in Fig. 3.3.

Soft robot gloves enable actuation of O/R motions without rigidly constraining the motion. They can relieve issues with axis misalignment and enable less constrained motions. However, for individuals with pathologies of the hand, their muscles, tendons, and bones cannot be guaranteed to guide the motion along safe and useful trajectories. Furthermore, they often can only actuate each digit along a single predefined trajectory, and must be reconfigured or re-manufactured for a different trajectory. Kadowaki et al. developed an entirely cloth and rubber soft robot glove using a spiral type pneumatic rubber muscle to actuate O/R [47]. Polygerinos et al. developed a topologically similar glove that is portable and uses soft fiber-reinforced hydraulic actuators [48]. Maeder-York et al. created a thumb-only soft robot glove for task-oriented stroke rehabilitation therapy that used a fiber-reinforced actuator with elastomer wrapped in a strain layer to replicate the trajectory of the opposition grasp of a healthy individual [49]. The HX is a rigid, cable-driven index finger and thumb exoskeleton that actuates O/R using an articulated parallelogram [50]. An earlier prototype of the HX called the HANDEXOS approximated O/R with an axis placed on the dorsum of the hand driven by a slider-crank mechanism [58].

It should be noted that many hand exoskeletons have been constructed with the thumb in opposition to the fingers. These designs, particularly those with A/A, can actuate the large majority of grasps. However, they cannot form grasps such as the platform push or abducted thumb power prismatic grasp that require the thumb to be in reposition. They are also incapable of training the motions involved in opposition.

3.2.4 Off-Axis Solution

Initial designs for the O/R motion of the thumb attempted to solve the problem using a remote center of motion. Two different mechanisms were designed, one featuring a semicircular prismatic joint and the other a four-bar parallelogram structure similar to ones designed for joints of the BLUE SABINO. However, these designs were deemed overly complex and prohibitively large for use with a hand exoskeleton to be placed on upper-limb exoskeletons.

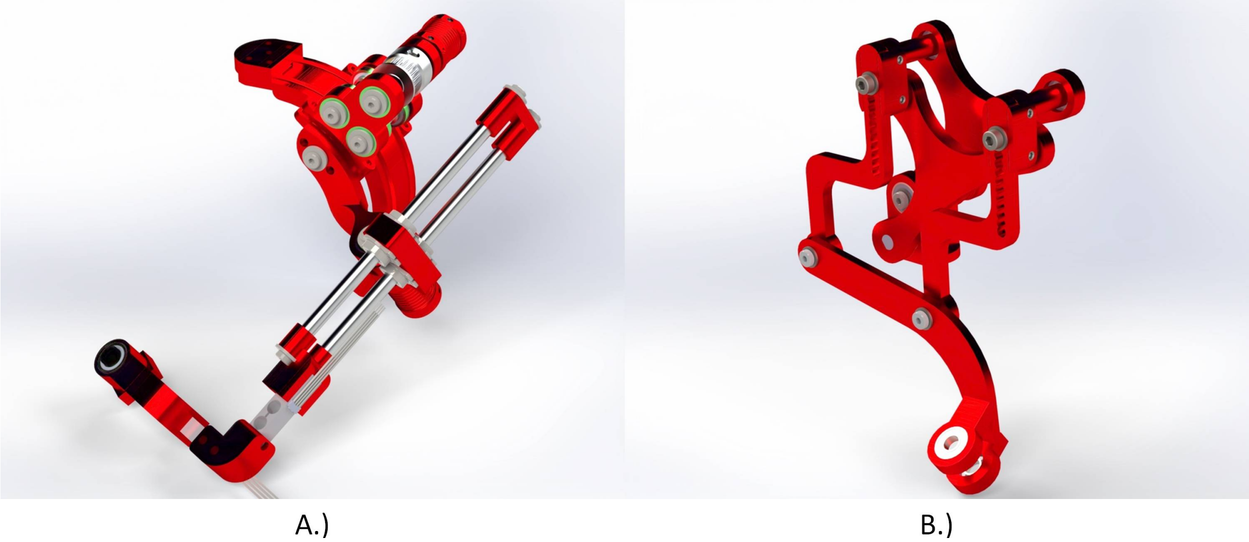

Figure 3.4: Two prior designs for the O/R joint. A.) Semicircular prismatic joint design. B.) Four-bar parallelogram design.

The semicircular prismatic joint presented challenges with high complexity, tight tolerances for manufacturing, and high friction when subjected to higher forces/torques involved with F/E. The parallelogram mechanism performed better, but kinematics required it to be of a size and position that would place it in the way of the transmission system of the finger linkages. CAD Renderings of the two mechanisms are shown in Fig. 3.4.

Further, although O/R was achieved, the lack of any A/A created unnatural motion when tested with additively manufactured prototypes. As such, it was determined that moving the axis of rotation from O/R towards A/A by some angle θ_{Off}, as shown in Fig. 3.2, could enable more natural motions. Furthermore, an off-axis design with sufficiently large θ_{Off} enables placement of the mechanism along the axis without interfering with radial deviation. As O/R was the primary desired motion, the minimum θ_{Off} that prevented this interference was chosen, namely 20°, to match normal radial deviation range of motion [59], [60]. Testing with 3D-printed prototypes confirmed the mechanism permitted opposition of all finger tips as well as full reposition.

3.3 Link Length Optimization

The unisize and workspace requirements dictate that the workspace of the OTHER Hand must cover the full relevant workspace of the hand, namely all reachable configurations of the fingers and thumb in their respective F/E planes, of all individuals between the 5th and 95th percentile for hand size. Due to the selection of a base-to-distal topology, this can be achieved without adjustments for link length if each linkage contains three F/E joints. However, an infinite number of link length combinations can satisfy these requirements. Thus, it is necessary to specify a design score to optimize in order to obtain appropriate link lengths.

This problem has been addressed by several hand exoskeletons with base-to-distal topologies [30], [61]–[63]. The optimization algorithm used for the OTHER Hand was previously published in [64] and is summarized below.

3.3.1 Zero Final Link Length

The original prototype of the hand exoskeleton featured 3R planar linkages placed on the dorsal side of the hand. One of the consequences of this configuration was nonzero length of the final link that attaches to each finger. This was observed to be a prominent issue in the design, as the final joint of each linkage was passive. As such, each finger was able to make significant uncontrolled motions in the F/E plane while in the exoskeleton. To address this, it was determined that the final link should have zero link length. This necessitated placing the axis of rotation of the final joint lateral to the attachment point located 1cm distal to the DIP joint. The trade-off made is that the mechanism now occupies space both adjacent to and behind the fingertip. It should also be noted that this design choice is only physically possible if there are no linkages connecting to only the ring and/or middle fingers.

3.3.2 Dorsal-Lateral Placement of Linkages

The decision to place the final F/E joints lateral to the biological fingers reduced the cost of placing the first and second F/E joints also lateral to the finger. Doing so again causes the linkage to occupy space both lateral and dorsal to the finger, which is undesirable, but removes the issue of joint collisions. In order to prevent the exoskeleton and finger joints from colliding, the required link lengths in the original prototype of the hand exoskeleton were undesirably large, as can be seen in Fig. 2.1. Placement of the joints lateral and distal to the fingers enabled much smaller linkages. For comparison, the total length of the index finger of the original hand exoskeleton was 20.9 cm versus just 13.9 cm for the OTHER Hand. It should be noted that the A/A and O/R joints of exoskeleton intended to align with biological joints such that the A/A motions of the fingers and O/R motion of the thumb do not affect the relative positions of the F/E exoskeleton joints projected onto the F/E planes of the digits. Lateral placement is illustrated in Fig. 3.1.

3.3.3 Finger Anthropometry

The first required portion of the optimization algorithm was to define the link lengths and joint ROM of the human digits actuated by the exoskeleton. The three digits under consideration were the thumb, index, and ring fingers. The linkage controlling the ring finger

Table 3.2: Minimum, mean, and maximum considered segment lengths.

Digit	Segment	Minimum (cm)	Mean (cm)	Maximum (cm)
Thumb	Metacarpal	3.834	4.622	5.410
	Proximal Phalanx	2.531	3.157	3.783
	Distal Phalanx	1.847	2.167	2.487
Index	Proximal Phalanx	2.990	3.978	4.966
	Medial Phalanx	1.736	2.238	2.740
	Distal Phalanx	1.130	1.582	2.034
Ring	Proximal Phalanx	3.363	4.137	4.911
	Medial Phalanx	1.907	2.565	3.223
	Distal Phalanx	1.286	1.730	2.174

always also controls the pinky, and thus could have been based on pinky finger measurements. However, it was determined to be safer to actuate the ring finger, and let the pinky be attached than vice versa. Table 3.2 shows the minimum, mean, and maximum lengths considered of each relevant hand segment, which correspond to small, medium, and large hands. The lengths of each segment for each of the three digit sets were calculated from $\mu - 2\sigma$, μ, and $\mu + 2\sigma$, where μ and σ are the mean and standard deviation of each finger segment length as reported in [45]. The ROM of each F/E joint is listed in Table 3.3. Joint ROM were obtained from [65] and observations of desirable ranges. Hyper-extension was not considered for any joint for safety purposes.

Table 3.3: Considered range of motions of joints in F/E.

Digit	Joint	Range of Motion
Thumb	Carpometacarpal	56°
	Metacarpophalangeal	73°
	Interphalangeal	85°
Fingers	Metacarpophalangeal	100°
	Proximal Interphalangeal	105°
	Distal Interphalangeal	85°

3.3.4 Modeling of 3R Planar Mechanisms

In order to guarantee that any combination of link lengths will cover the workspace of the human digit, it is necessary to find the kinematics of the digit and robot linkage. As the second joint of each linkage is intended to remain stationary relative to the associated actuated digit, due to alignment of finger and linkage A/A or O/R, it is possible to simplify each digit and linkage to planar 3R mechanisms. For the following analysis, L_1, L_2, and L_3 are the link lengths and θ_1, θ_2, and θ_3 are the F/E joint angles of the of the 3R mechanism. As the exoskeleton is only intended to attach to the distal phalanx, only the coordinates (x, y) and orientation (ϕ) of the end of each mechanism is needed. The forward kinematics are shown in Eq. 3.1.

$$\begin{bmatrix} x \\ y \\ \phi \end{bmatrix} = \begin{bmatrix} L_1 c_1 + L_2 c_{1,2} + L_3 c_{1,2,3} \\ L_1 s_1 + L_2 s_{1,2} + L_3 s_{1,2,3} \\ \theta_1 + \theta_2 + \theta_3 \end{bmatrix} \tag{3.1}$$

where

$$\begin{aligned} &c_1 = cos(\theta_1), \quad c_{1,2} = cos(\theta_1 + \theta_2), \quad c_{1,2,3} = cos(\theta_1 + \theta_2 + \theta_3), \\ &s_1 = sin(\theta_1), \quad s_{1,2} = sin(\theta_1 + \theta_2), \quad s_{1,2,3} = sin(\theta_1 + \theta_2 + \theta_3) \end{aligned} \tag{3.2}$$

3.3.5 Mechanism Isotropy

Mechanism isotropy is a kinematic measure of the ability of a mechanism to move its end-effector in any direction, is a function of the joint angles, and ranges from zero to one. An isotropy value of zero specifies a singular configuration while a value of one indicates the end-effector can move equally well in all directions. As with the first-generation system, mechanism isotropy was considered as a desirable trait to consider in the optimization algorithm. However, the ways in which mechanism isotropy was included in the design score were modified to better account for a wider range of hand sizes.

By taking the derivative of Eq. 3.1 with respect to joint variables, and using the same shorthand defined in Eq. 3.2, the Jacobian matrix with respect to the ground frame, ${}^0J$, is obtained in Eq. 3.3:

$${}^0J = \begin{bmatrix} -L_1 s_1 - L_2 s_{1,2} - L_3 s_{1,2,3} & -L_2 s_{1,2} - L_3 s_{1,2,3} & -L_3 s_{1,2,3} \\ L_1 c_1 + L_2 c_{1,2} + L_3 c_{1,2,3} & L_2 c_{1,2} + L_3 c_{1,2,3} & L_3 c_{1,2,3} \\ 1 & 1 & 1 \end{bmatrix} \tag{3.3}$$

Mechanism isotropy is defined in [66] as the inverse of the condition number of ${}^0J$. Namely, the mechanism isotropy, $ISO(\boldsymbol{\theta})$, can be written as in Eq. 3.4:

$$ISO(\boldsymbol{\theta}) = \frac{\sigma_{min}}{\sigma_{max}} \in [0, 1] \tag{3.4}$$

where σ_{min} and σ_{max} are the minimum and maximum singular values of the ${}^{0}J$, respectively, and $\boldsymbol{\theta} = [\theta_1, \theta_2, \theta_3]$.

3.3.6 Projected Planar Area

As noted in the previous chapter, the link lengths summed and taken to the power of an arbitrary hyperparameter was used to penalize excessively long linkages in the optimization algorithm of the first-generation hand exoskeleton. While the hyperparameter could be tuned to result in reasonable linkages, the physical meaning of what was penalized was lost. As such, an alternative value with more physical meaning was sought for inclusion in the design score to ensure reasonable link lengths.

The selected value is the area of the largest polygon created with all vertices at joints of the digit or linkage projected on the F/E plane of the digit as shown in Fig. 3.5. As the configuration of the digit is fully defined (assuming no hyper-extension of any joint) by the configuration of the linkage, $AREA(\boldsymbol{\theta})$ is fully defined by the joint angles of the linkage. This value serves as a measure of the physical envelope or bulk of the exoskeleton, and thus should be minimized.

3.3.7 Optimization Summary

The optimization algorithm used a grid search for the optimal link lengths of each F/E link based on kinematic performance as defined by $ISO(\boldsymbol{\theta})$ and $AREA(\boldsymbol{\theta})$. As the exoskeleton must fit hands between the 5th and 95th percentiles for digit length, three sets of digits were optimized across. Namely, a small hand in the 5th percentile for digit length, a medium hand in the 50th percentile, and a large hand in the 95th percentile with phalanx lengths specified as Minimum, Mean, and Maximum, respectively, in Table 3.2. However, regardless

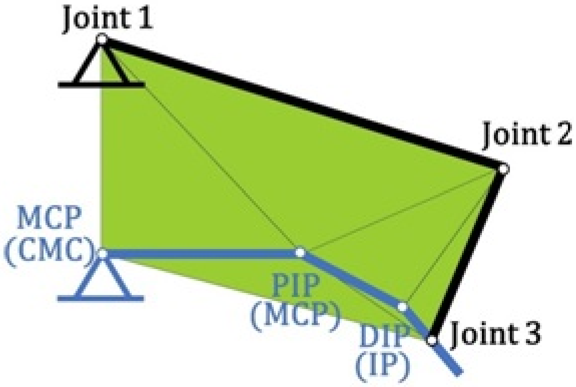

Figure 3.5: Visualization of $AREA(\boldsymbol{\theta})$. The blue 3R mechanism represents the human digit while the black represents the robot linkage. The green polygon is the largest possible with all vertices coincident with joints of the digit or linkage [64].

of distal phalanx length, the OTHER Hand exoskeleton was designed to attach 1 cm distal to the DIP joint (ITP joint for the thumb linkage). For each digit, the joint angles were varied in 3° increments from 0° (extended without hyperextension) to a maximum flexion angle as specified by Range of Motion in Table 3.3. A range of combinations of possible link lengths (narrowed down to appropriate ranges iteratively through use of the optimization algorithm) were generated for each linkage. The elbow-up (Joint 2 dorsal to the finger as shown in Fig. 3.5) inverse kinematic solutions to all combinations of hand sizes and joint angles for the corresponding digit were then calculated, creating sets of joint angles $\boldsymbol{\theta}$. All possible link length combinations that did not have valid solutions for all $\boldsymbol{\theta}$ considered were assigned *Design Score* of 0, as they would not be able to accommodate the required range of hands. Each remaining link length combination was then assigned a *Design Score* given by Eq. 3.5:

$$Design\,Score = \frac{\sum_{\boldsymbol{\theta}\in K}(ISO(\boldsymbol{\theta}))\min_{\boldsymbol{\theta}\in S}(ISO(\boldsymbol{\theta}))\min_{\boldsymbol{\theta}\in M}(ISO(\boldsymbol{\theta}))\min_{\boldsymbol{\theta}\in L}(ISO(\boldsymbol{\theta}))}{\sum_{\boldsymbol{\theta}\in K}(AREA(\boldsymbol{\theta}))} \tag{3.5}$$

where S, M, L, and K are all combinations of $\boldsymbol{\theta}$ generated by link length and joint angle combinations of the small hand, medium hand, large hand, and all hands respectively. The

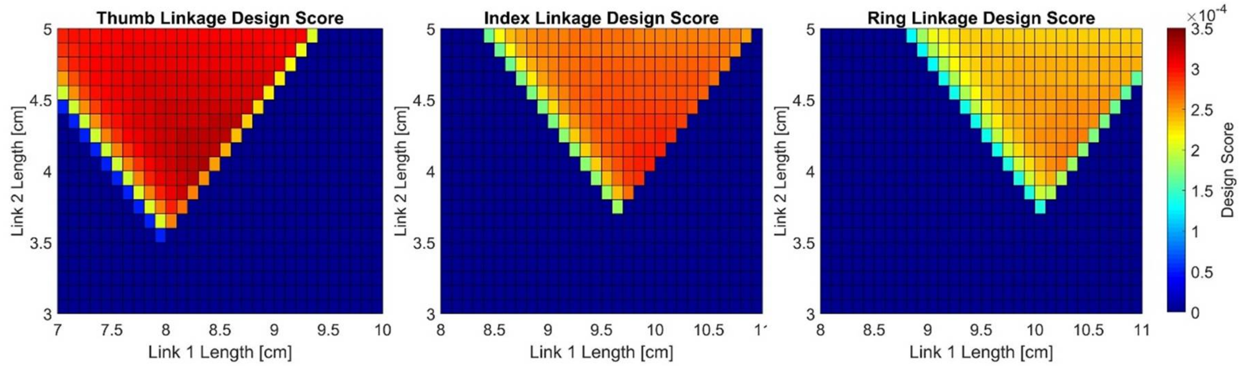

A.) B.) C.)

Figure 3.6: Optimization results for the A.) thumb linkage, B.) index finger linkage, C.) ring finger linkage [64].

numerator of the $Design\,Score$ consists of isotropy terms. The first term is the sum of the mechanism isotropy across all configurations of the hands, and is an overall measure of the kinematic performance of the linkage. This term is multiplied by the minimum $ISO(\boldsymbol{\theta})$ in the workspace of each of the small, medium, and large hands. These minimum $ISO(\boldsymbol{\theta})$ terms serve to penalize designs that do not perform well across all hand sizes. Lastly, the denominator consists of the sum of the $AREA(\boldsymbol{\theta})$ across all configurations of the hands in order to penalize designs that occupy excessive volumes. The set of link lengths with the highest $Design\,Score$ for each digit were considered the optimal solutions.

3.3.8 Results

Fig. 3.6 shows the results of the optimization algorithm for the thumb, index finger, and ring finger. Table 3.4 shows the optimal link lengths and corresponding design score. These link lengths were tested with 3D prototypes to verify kinematic performance and size, and then used in the OTHER Hand exoskeleton.

Table 3.4: Optimized link lengths and corresponding *Design Score*.

Linkage	L_1 (cm)	L_2 (cm)	L_3 (cm)	*Design Score*
Thumb	8.3	4.0	0	$3.283*10^{-4}$
Index	9.9	4.0	0	$2.943*10^{-4}$
Ring	10.3	4.1	0	$2.597*10^{-4}$

3.4 Attachments

To assist ease of use by stroke patients, the OTHER Hand is designed to be quickly and securely donned/doffed by stroke patients (with assistance). One specific motor deficit that is common following stroke is spasticity. Spasticity is defined as a state of increased muscle tone with exaggerated reflexes. In the hand, this presents as stiff muscles, low flexibility, and a resting clenched fist posture. In a study of 301 stroke patients, 42.6% developed spasticity after 6 months, with 15.6% classified as clinically relevant (severe) according to the Modified Ashworth Scale which measures the resistance of a relaxed limb to rapid passive stretches [67]. Spasticity of the upper limb was more common, presenting in 35.5% of the patients [67]. Patients with spasticity had lower scores on the Barthel Index, which measures ability to independently perform ADLs [67]. Due to the prevalence of spasticity in the intended patient population, a glove was ruled out, and the OTHER Hand was designed for each attachment to be donnable as independently as possible.

3.4.1 Palm Attachment

In keeping with the requirement of easy use by stroke patients, the attachment to the palm is designed to be quickly and securely donned/doffed. The palm attachment is made from 3D-printed PLA plastic, designed using 3D scans of a hand, and padded with neoprene where it contacts the user. The attachment is separated into a posterior segment secured to the aluminum base-plate of the exoskeleton and an anterior segment connected to an aluminum sliding mechanism that can be quickly locked relative to the base-plate via a cam

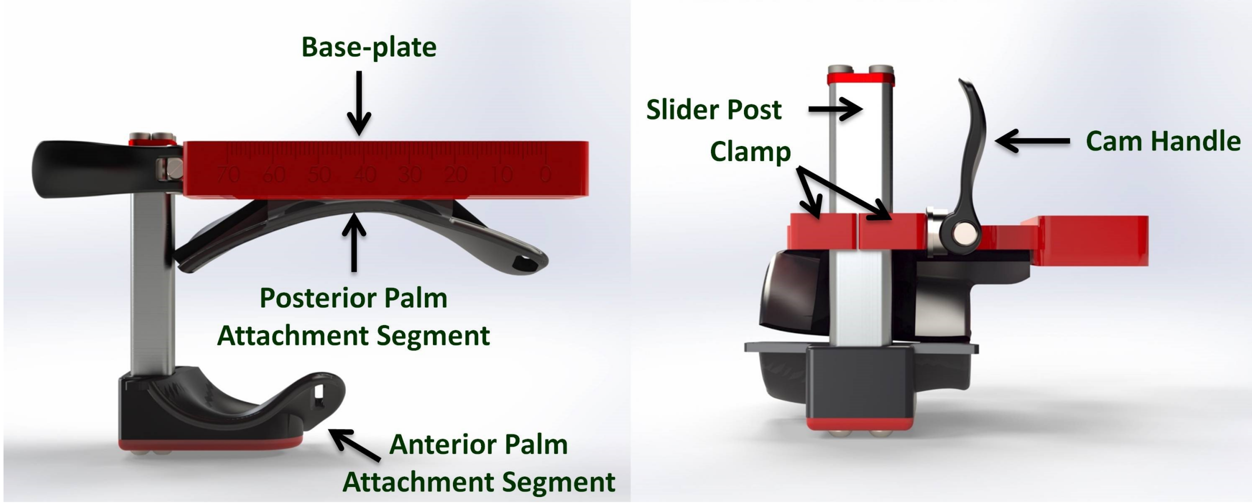

A.)

B.)

Figure 3.7: Palm attachment. Note that hook-and-loop straps and neoprene padding are not displayed. A.) Front view with mechanism open. B.) Side view with mechanism closed.

handle. To permit thumb O/R motions, the anterior segment only covers the proximal-ulnar portion of the palm. To further secure the palm, hook-and-loop straps connect between the anterior and posterior segments. The palm attachment is shown in Fig. 3.7.

3.4.2 Quick Disconnect

To enable reconfigurability and ease of use, the thumb and all finger attachments are designed with quick disconnect mechanisms. Each attachment connects to the linkages by sliding into a slot that constrains 5 DoFs, and then locking in place using a pivoting latch and ball-nose spring plunger. Figs. 3.8A and 3.8B display the quick disconnect mechanism. The attachments are secured to the user's fingers via hook-and-loop straps. The long-finger attachments attach to the distal phalanges just past the most distal joint. As the thumb actuates O/R, the attachment must be robust to rotation around the long axis of the thumb. Thus, the thumb attachment features a double parallelogram mechanism that attaches at both the distal and proximal phalanges and passively permits F/E of the interphalangeal joint.

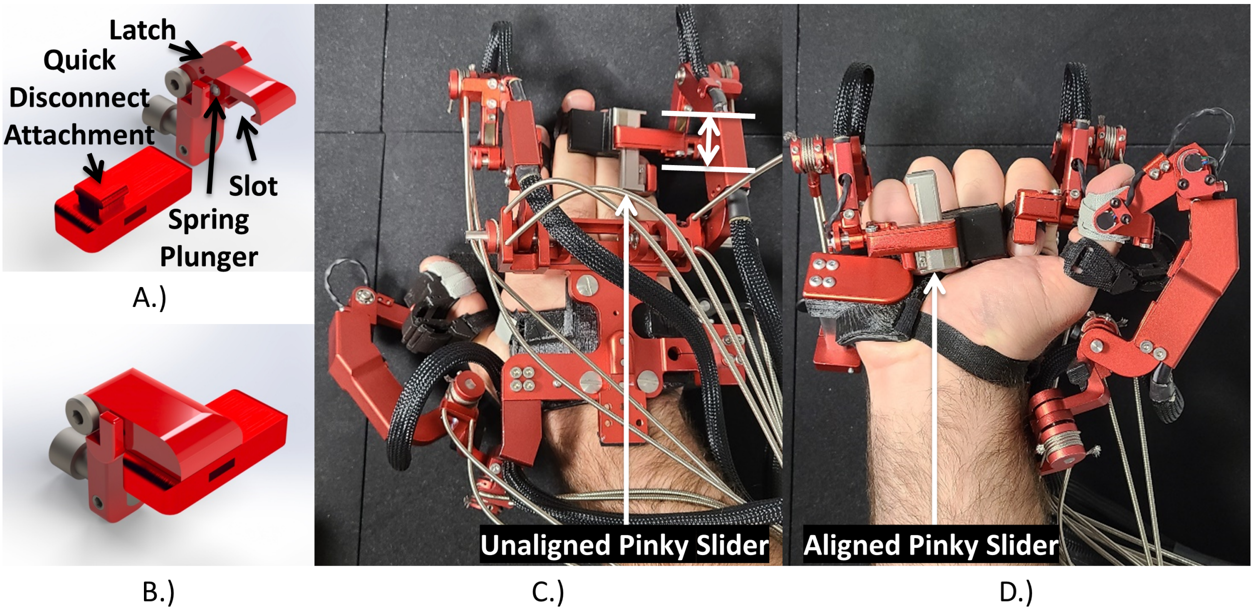

Figure 3.8: Finger attachments. A.) Exploded view of the quick disconnect mechanism. B.) Assembled view. C.) Posterior view of the 1-1-3 finger attachments with pinky slider unaligned. D.) Anterior view with pinky slider aligned.

In addition to enabling reconfigurability, the quick disconnect attachments make the device more easily donned by stroke patients. The quick disconnect mechanisms allow users to don the attachments finger-by-finger before getting into the exoskeleton. Once in the exoskeleton, each attachment can then be connected to the appropriate linkage. While wearing the finger attachments, a practiced user can insert the hand, secure the palm attachment, and connect the quick disconnects of one hand in approximately 45 seconds using their other hand. When fully attached, quick disconnects and palm attachments can be disconnected such that the hand can be removed from the exoskeleton in as little as 20 seconds.

3.4.3 Pinky Slider

The distal phalanx of the pinky frequently moves with respect to that of the ring finger. Specifically, with variation between individuals, the tip of the pinky distal phalanx can be several centimeters more proximal to the palm than that of the ring finger when the fingers are extended. However, when flexed into a fist, the pinky advances with respect to the ring finger such that the their tips align. As in the first-generation hand, this is accounted for by a pinky slider mechanism that is incorporated in the attachments that connect to the ring and pinky fingers (and middle finger when in the 1-1-3 configuration). This slider mechanism constrains the pinky distal phalanx to be parallel to the ring distal phalanx, but allows it to move with a single passive prismatic DoF. This permits approximation of some of the grasps requiring independent motion of the pinky finger that would otherwise be prohibited by a 1-2-2 or 1-1-3 configuration. The pinky slider is shown in Figs. 3.8C and 3.8D.

3.4.4 Adjustments

Although the link lengths of the OTHER Hand were selected to fit all fingers from the 5th to 95th percentile, it is necessary to add adjustment mechanisms to change the placement of the linkages to enable use with individuals of varying hand widths and thicknesses. The thumb is designed with four discrete positions for the origin of frame $T2$ as indicated by the different options for D_{T2} in Fig. 3.1. In the same figure, A_{I1} and A_{R1} display the continuous adjustment ranges of the X position of frames $I1$ and $R1$, respectively, as seen in the 0 frame. As such, the linkages can be adjusted to best maintain alignment of the F/E planes of the exoskeleton with those of the biological digits through the joint ranges of O/R of the thumb and A/A of the fingers. Additionally, three sizes of the anterior segment of the palm attachment are available for different hand sizes.

3.5 Actuation and Transmission

As with the first-generation hand, a Bowden cable transmission system with brushed DC motors was chosen to address the low mass and torque requirements. The cable transmission enabled remote location of the motor pack, reducing mass at the hand. It also allowed use of actuators with sufficient torque for hand rehabilitation.

3.5.1 DC Brushed Motors

The OTHER Hand is actuated by Maxon (`https://www.maxongroup.us`) motor combinations consisting of DCX19S GB KL 18V motor, GPX19HP 231:1 planetary gearhead, and ENX16EASY 256IMP quadrature encoder. DC brushed motors with built in gearboxes and quadrature encoders were selected to actuate the system due to their ease of control, price, and performance. The motors and gearbox were sized to provide 1.6Nm of nominal torque compared to just 0.3Nm of torque for the first-generation hand. Given the robot kinematics across it's workspace, 1.6Nm enables application of at least 11.1N in any given direction. This is comparable to the maximum forces with which the fingertip can resist applied forces without moving, which is highly dependent on finger position and force direction, as reported in [68]. As the Maximum joint rotation angular velocity is 52RPM, which was judged to be sufficient for fast finger movements during rehabilitation. Six motors are used for each hand.

3.5.2 Bowden Cable Transmission

Bowden cable transmissions were selected in order to permit remote placement of the motor pack, such as at the elbow joint of the EXO-UL8. The cables used are CB-0044-777-CS-U steel 7x7x7 construction, 0.044" diameter wires with 756N breaking strength from Strand Products (`https://strandproducts.com`). Given the 1.6Nm motor torque and diameter of the capstans used, up to 213.5N of tension can be applied, for a factor of safety of 3.54. The cables are sheathed in SG-100-023-120 0.1" outer diameter, 0.054" inner diameter round wire spring guides from the D.R. Templeman Company (`https://www.drtempleman.com`). These spring guides were chosen without an external plastic layer to minimize the forces/torques experienced by the fingers and wrist when the fingers, wrist, or elbow joints are actuated. To further minimize the resistance of the cable guides to finger movements, the guides are routed through channels in the axis of rotation of the first joints of the finger linkages. In-line cable tension adjusters are installed on each cable.

3.6 Sensors

Each hand of the OTHER Hand features six quadrature encoders for rotational measurement of active joints, four magnetic rotary encoders for the F/E passive joints, and six single-axis force sensors. All wires from the magnetic rotary encoders and force sensors are shielded to reduce noise and routed through numerous strain reliefs to improve durability of the system.

3.6.1 Force Sensors

As each linkage possesses two active DoFs, two single-axis force sensors are used in each. All force sensors used are S215 ultra-low profile, single point load cells with 53.37N capacity from Strain Measurement Devices (`https://www.smdsensors.com`). These sensors were selected as the smallest available single point load cells with appropriate ranges. Each sensor is integrated so as to create the physical structure of the links. Each of the finger linkages possess two such load cells measuring forces in the F/E plane placed between the first and second F/E joints, and between the second and third F/E joints. The thumb contains two force sensors placed perpendicularly to each other, just after the actuated F/E joint, so as to measure forces associated with F/E and with O/R. Placement of the force sensors along with direction of measured force are indicated in Fig. 3.1.

3.6.2 Rotation Sensors

Each actuated DoF is measured in rotation using the ENX16EASY 256IMP quadrature encoders with 256 counts per turn. All passive joints involved in F/E are measured with RM08 super small non-contact rotary encoders from Renishaw (`https://www.renishaw.com`). These magnetic absolute encoders are used in the 360° linear voltage variety. Custom mounts are used to position the sensors.

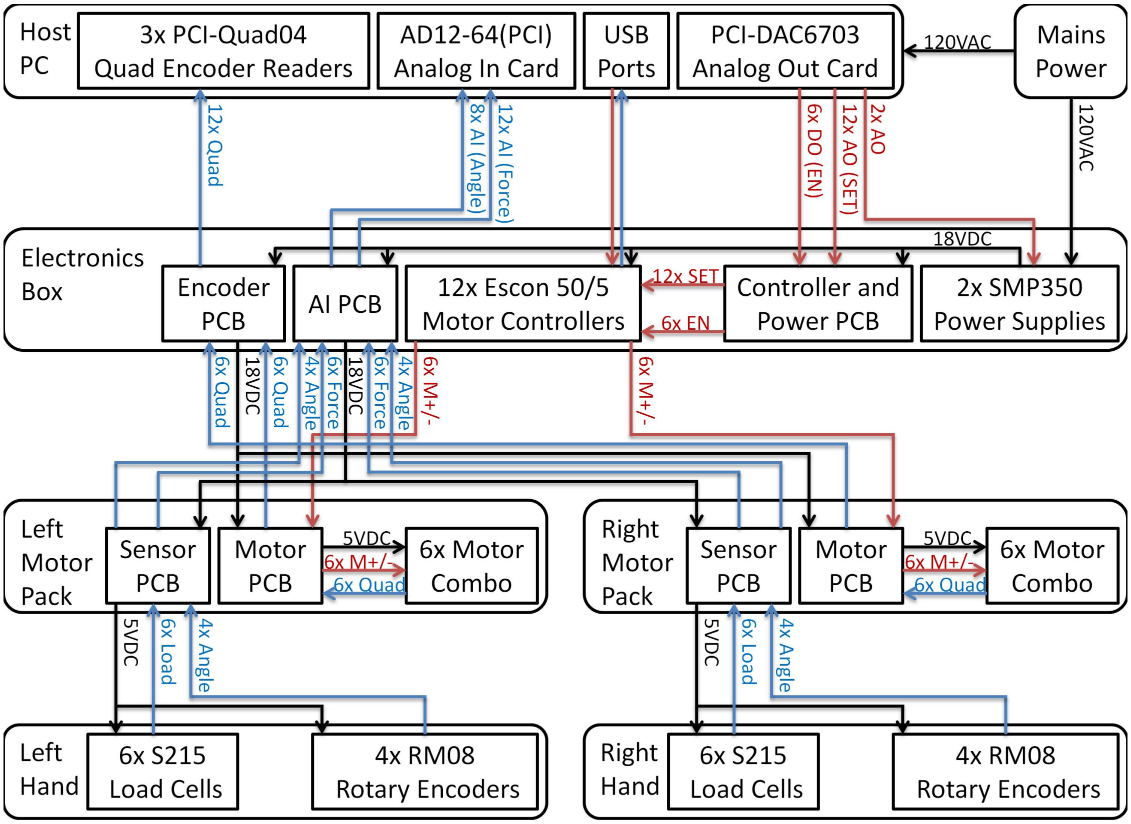

Figure 3.9: Overview of the electronic subsystems and connections of the OTHER Hand. Red arrows indicate outgoing command signals (towards the hand). Blue arrows indicate incoming sensor signals (towards the host PC). Black arrows indicate power signals. Note that the 'Force' signal is the 'Load' signal after amplification, and the 'M+/-' signal is the motor signal determined by the 'SET' signal.

3.7 Electronics

The electronics of the OTHER Hand consist of four hubs: the host PC, the electronics box, and the left and right motor packs. Signal routing between hubs is displayed in Fig. 3.9.

3.7.1 Hand

The hand contains the least number of electrical connections, but the most challenges with wire routing. Each of the four passive joint rotation sensors is wired to a three-position shielded cable and routed through various strain relief and wire guides built into each linkage. Each of the six force sensors are connected to shielded four-position wires that similarly are routed through strain relief. All 36 connections on each hand are systematically combined from 10 wire bundles to one which is then connected to a custom ‘Sensor’ PCB mounted at the motor pack. All wire bundles are wrapped in cable sleeves and merged using heat shrink tubing.

3.7.2 Motor Pack

The motor packs serve to improve wire management, reduce the length of cables including those for noise-sensitive unamplified force sensor signals, and amplify said signals. All sensor and motor signals are routed through three custom PCBs. The motor packs feature 3D-printed covers that hide the motors and PCBs.

3.7.2.1 Routing PCB

A ‘Routing’ PCB is added to each motor pack to communicate between the electronics box and the Sensor and Motor PCBs. The Routing PCB serves only to convert from the the ribbon cables sent from the two other PCBs to the enclosure box into three D-Sub cables. This was done because D-Sub cables are shielded and connect far more securely (due to screwing to the PCB) than the ribbon cables output from the other two PCBs. The Routing PCB is not displayed in Fig. 3.9.

3.7.2.2 Sensor PCB

The ‘Sensor’ PCB receives all connections from the hand, and amplifies the signals of the force sensors using INA125U instrumentation amplifiers. The PCB outputs a 12-connector ribbon cable that is converted to a 15-pin high-density D-Sub cable at the Routing PCB, which in turn connects to the electronics box. The PCB receives 18VDC and ground from the electronics box, which is used to power the instrumentation amplifiers as well as an on-board MC7805 5V voltage regulator connected to the rotary sensors. The remaining 10 connections to the electronics box consist of a single signal for each sensor.

3.7.2.3 Motor PCB

The custom ‘Motor’ PCB routes all signals from and to the six motors. Two ribbon cables connect the Motor PCB to the Routing PCB, which converts them to two D-Sub cables that connect to the electronics box. A 40 connector 28AWG ribbon cable converts to a 44-pin high-density D-Sub cable and is used to route 18VDC power to an on-board MC7805 5V voltage regulator powering all the motor encoders, and route the 6 signal wires of each encoder to the electronics box. A 12-connector 22AWG ribbon cable converts to a 15-pin standard-density D-Sub cable and is used to route the motor+ and motor- signals from the electronics box to each of the motors.

3.7.3 Electronics Box

The electronics box shown in Fig. 3.10 is a rackmount enclosure that contains three custom PCBs for wire routing, two SMP350 18VDC switching power supplies, four fans for cooling, a 3-outlet power strip, a 12-outlet USB hub, and twelve Escon 50/5 motor controllers from Maxon Precision Motors, Inc. The electronics box connects all signals to/from the motor pack to the motor controllers, power supplies, the host PC, foot pedal, and emergency stop button.

Figure 3.10: The electronics box containing the power supplies, motor controllers, and wire routing PCBs. A.) Front panel. B.) Rear panel.

Additionally, the electronics box features custom front and rear panels. These panels contain contain numerous PCBs (not shown in Fig. 3.9) and discrete components. The front panel mounts two fans for cooling, as well as LED indicators for status of the power supplies, motor controllers, and software. The rear panel passes through all connections from/to the motor pack and host PCB, the foot pedal, the emergency stop button, and mains power (with power switch).

3.7.4 Host PC

The host PC is a 4U rack mount industrial PC featuring a 6th Gen Core i7 processor, 8GB of ram, 500GB solid state drive, 2TB 7200RPM hard drive, and backplane with 10 PCI, 1 PCIe x4, and 1 PCIe x16 (part SL-4U-SBC-Q170-HA from SuperLogics, Inc). Installed on the PC are three PCI-QUAD04 4 quadrature encoder reader PCI cards (Measurement Computing Corp.), a PCI-DAC6703 16 analog output PCI card (Measurement Computing Corp.), and a Contec AD12-64(PCI) 64 analog input PCI card (Contec Co., Ltd). These cards are used to interface with the required 12 quadrature encoders (installed on the 12 motors), 20 analog inputs (12 from force sensors, 8 from magnetic rotary encoders), and 12 analog outputs (control signals to the 12 motor controllers).

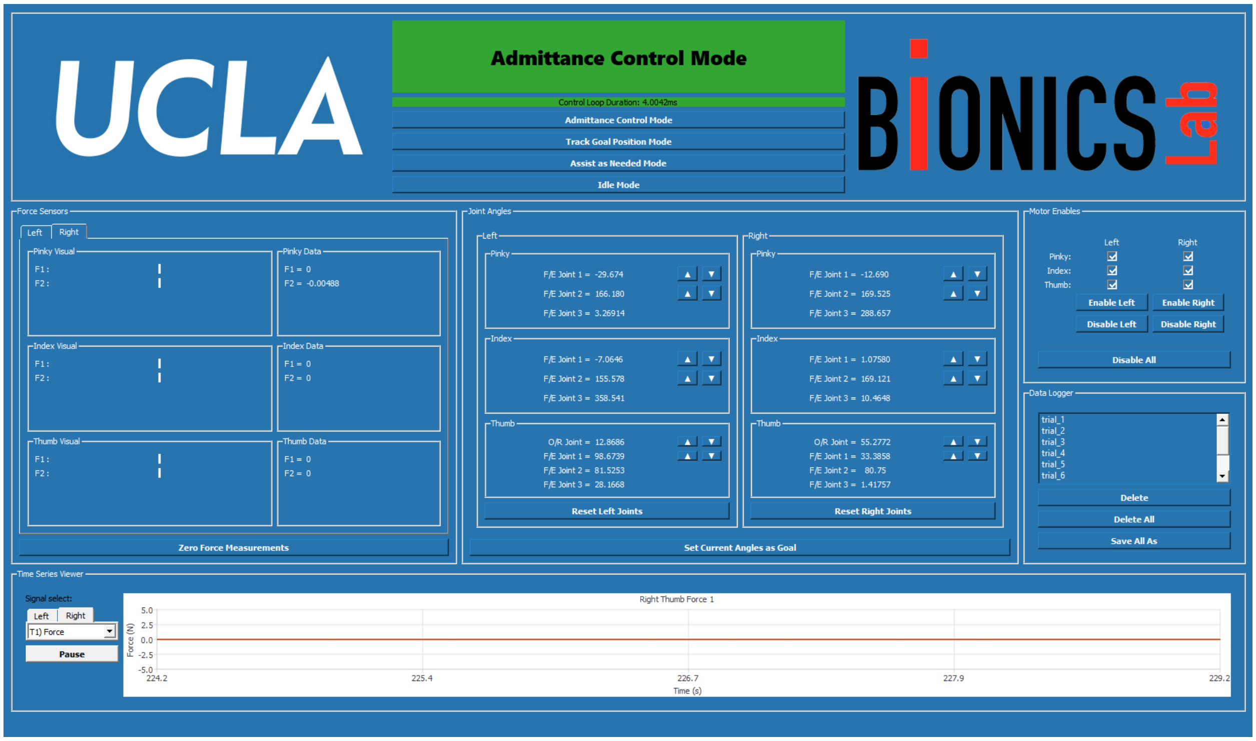

Control Loop Duration: 4.0042ms

Force Sensors (Right)

Pinky Data: F1 = 0, F2 = -0.00488

Index Data: F1 = 0, F2 = 0

Thumb Data: F1 = 0, F2 = 0

Joint Angles

Left – Pinky: F/E Joint 1 = -29.674, F/E Joint 2 = 166.180, F/E Joint 3 = 3.26914

Left – Index: F/E Joint 1 = -7.0646, F/E Joint 2 = 155.578, F/E Joint 3 = 358.541

Left – Thumb: O/R Joint = 12.8686, F/E Joint 1 = 98.6739, F/E Joint 2 = 81.5253, F/E Joint 3 = 28.1668

Right – Pinky: F/E Joint 1 = -12.690, F/E Joint 2 = 169.525, F/E Joint 3 = 288.657

Right – Index: F/E Joint 1 = 1.07580, F/E Joint 2 = 169.121, F/E Joint 3 = 10.4648

Right – Thumb: O/R Joint = 55.2772, F/E Joint 1 = 33.3858, F/E Joint 2 = 80.75, F/E Joint 3 = 1.41757

Motor Enables

	Left	Right
Pinky:	☑	☑
Index:	☑	☑
Thumb:	☑	☑

Data Logger: trial_1, trial_2, trial_3, trial_4, trial_5, trial_6

Signal select: Right – T1) Force

Figure 3.11: The GUI for the OTHER Hand controller

3.8 Software and Control

The OTHER Hand is controlled from the host PC running a C++ executable. A *Graphical User Interface* (GUI), written with Qt, displays sensor information numerically and graphically, enables manual control of each joint, permits selection of control scheme, and allows for data logging. The GUI is shown in Fig. 3.11.

Although the OTHER Hand is anticipated to use a variety of control schemes for rehabilitation, a simple *Proportional-Derivative* (PD) admittance controller running at 250Hz is currently implemented. The control receives as inputs the forces measured from the load cells. The proportional and derivative of the error of each force reading is scaled and then mapped one-to-one to the actuator of an adjacent joint. The first F/E joint of each finger and thumb is controlled by a force sensor between the first and second F/E joint. For each finger, the second F/E joint is controlled by the force sensor between the second and third

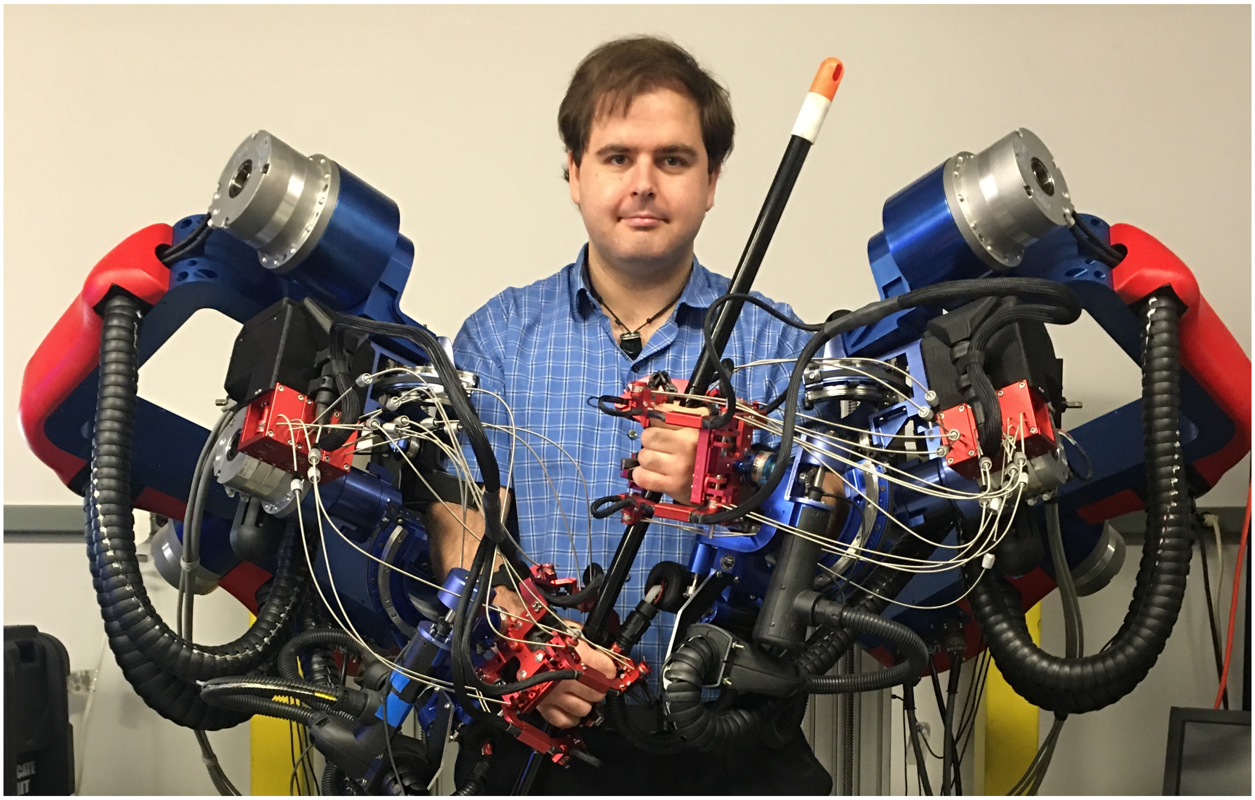

Figure 3.12: OTHER Hand mounted on the EXO-UL8 upper-limb exoskeleton demonstrating bimanual grasping.

F/E joint. The O/R joint of the thumb is controlled by the other force sensor between the first and second F/E joint (that measures forces normal to the F/E plane). While this one-to-one mapping does not well account for the dynamics of the linkages, all test subjects have favorably evaluated the naturalness and ease of the resulting motions. Thus, it is deemed that including cross-terms between joints is likely unnecessary as the dynamic effects are small compared to the forces involved in grasping.

3.9 Integration with the EXO-UL8

In addition to functioning as a standalone device, the OTHER Hand can be mounted to the EXO-UL8 as shown in Fig. 3.12. Such combined *Arm and Hand Exoskeleton* (AAHE) systems featuring several-DoFs hand systems and full arm systems provide significant advantages. Primary among them is the ability to train reach-to-grasp ADLs. This is crucial, as it has been observed that the training effects of rehabilitation exercises are task specific [69]. It is therefore anticipated that rehabilitation with the combined OTHER Hand and EXO-UL8 system would not only be more time efficient, but may result in improved outcomes compared to separate trainings with each system alone. As both systems are bilateral, the combined system is also capable of bilateral/bimanual training and tasks. A secondary advantage comes from the inherent positional knowledge of the hand due to measurement of the joint angles of the arm. Although there are other ways to obtain position and orientation of the hand, they typically require some form of optical tracking and therefore can suffer from occlusion issues. Position and orientation of the hand can be useful for VR applications and games that are common methods of improving attentiveness and participation during rehabilitation sessions.

3.9.1 Challenges

There exist a number of challenges to integrating a hand exoskeleton and arm exoskeleton together. These challenges can be broadly classified into mechanical, electrical, and control.

3.9.1.1 Mechanical Hardware

The foremost challenges of creating an AAHE are the inertia and high number of DoFs. Specifically, hand exoskeletons with many active DoFs require a corresponding number of actuators. In order to provide even comparable forces/torques and velocities to the contained biological hands, the combined mass of the required motors is non-negligible. Placement of the motors at the hand is possible, but requires either oversized motors on the arm or undersized motors at the hand. The motors can alternatively be placed further up the arm with a transmission system leading to the hand. This can reduce the inertia felt by the arm exoskeleton, but causes other challenges.

A second issue is that of interference. Generally speaking, the more DoFs at the hand, the more complex and bulkier the required mechanical assembly. If attached to an arm exoskeleton with a 3 DoFs wrist, it is difficult to design both systems such that no interference occurs across the entire range of motion of both subsystems. In the case of the OTHER Hand, the design has to work with both the EXO-UL8 and BLUE SABINO arm exoskeletons.

Lastly, as the number of required attachment points increase, donning/doffing the complete system becomes more challenging and time consuming. If a user has partial hemiparesis and/or hypertonia that causes a pathological resting posture, aligning and then attaching the exoskeleton to the user can become nearly impossible.

3.9.1.2 Electrical Hardware

The major challenges with regards to electrical hardware of an AAHE stem from the number of electrical connections required.

The obvious issue with many electrical connections is wire routing. For an entirely new AAHE, the arm subsystem can be designed to allow for neat routing of any cables within the exoskeleton structure. However, the shear number of connections can make this prohibitive, especially as it prevents design of the arm until all wiring of the hand is designed. This was also not an option for the OTHER Hand as the EXO-UL8 already existed.

The other issue with the number of connections comes from the requirements of any host PC or intermediate input/output system. The PC or input/output system must be capable of properly interfacing with the large number of motors and sensors at sufficiently high frequencies.

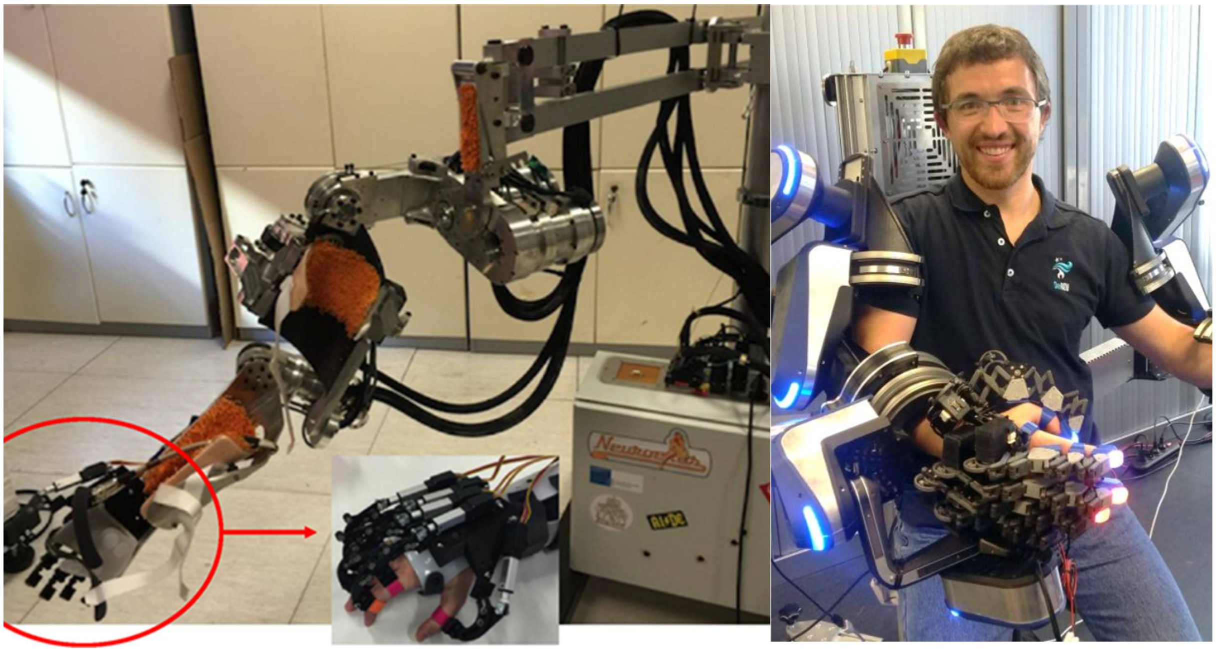

Figure 3.13: The only discovered combined full arm and hand exoskeletons in the literature. Left: [36], Right: [70].

3.9.1.3 Control

Control of any system generally gets more complicated with the number of DoFs. AAHE systems are no exception. Given the number and types of sensors, actuators, and transmission systems that must be accounted for, different parts of the system require different strategies to function well. Though it is no longer anticipated to be problematic due to speeds of modern computers, the computations required by the control system place an upper bound on control frequency.

3.9.2 Existing Arm and Hand Exoskeletons

Likely due to the numerous challenges with integrating a several-DoFs hand exoskeleton with an upper limb exoskeleton, the only two other such systems discovered in the literature are [36] and [70] shown in Fig. 3.13. However, Lauretti et. al. details the system with a combined total of 9 active DoFs (3 at the shoulder, 1 at the elbow, 1 at the wrist, and 4 at the hand) on a unilateral system compared to the 13 active DoFs (3 at the shoulder, 1 at the elbow, 3 at the wrist, and 6 at the hand) on each side of the bilateral system in the presented research [36]. DEXO [70] is similar to the current work in that it has matching numbers of active DoFs at the arm and hand. However, the DEXO Hand splits the 6 DoFs differently, and features a significantly different topology than the OTHER Hand. Numerous other systems, including the EXO-UL8, have single DoF hand modules, but they do not present the same challenges or advantages of a system with a multi-DoFs hand module, and thus are not considered comparable.

3.9.3 Motor Pack

The OTHER Hand uses a Bowden cable transmission system to minimize mass at the hand. As such, it was necessary to determine where and how to place the motors. The cables must be kept short because the further up the arm the motors are placed, the more potential for the Bowden cables to interfere with motions of the intervening DoFs and the lower the stiffness of the transmission system. However, the closer to the hand the motors are placed, the higher the inertia felt by the proximal motors of upper limb system. A suitable location for placement of the motor pack was determined to be on the Harmonic Drive motors of the elbow F/E joints as shown in Fig. 3.14. This results in a transmission length of approximately 45cm, and inertia of the motor pack only felt by the shoulder joints.

The motor pack of each hand contains six actuators, divided into three sub-packs. Each sub-pack contains two motors and associated capstans contained in a rigid structure, and is linked to the actuated DoFs of one of the three linkages of the OTHER Hand. All sub-packs of each side are connected to a single adapter designed to conform to the curvature of the elbow harmonic drive motor. The adapters are secured to the harmonic drives on each side with worm-drive hose clamps.

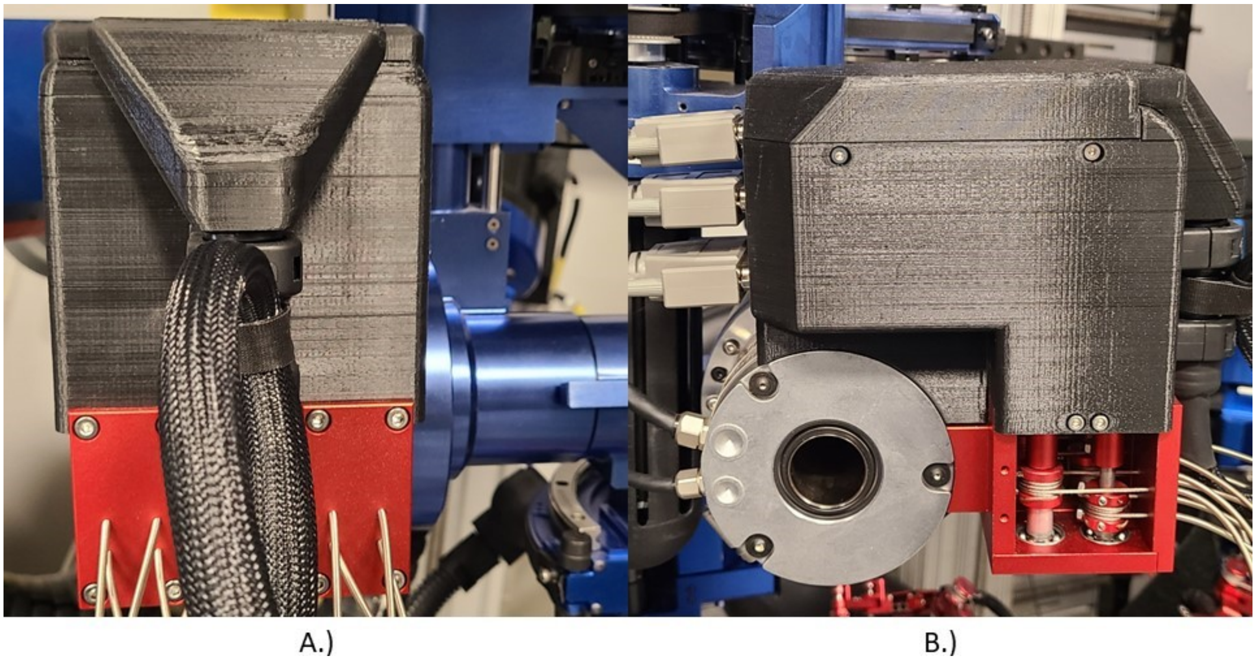

Figure 3.14: The motor pack mounted at the elbow joint of the EXO-UL8. A.) Front view. B.) Side view.

3.9.4 Wrist Attachment to EXO-UL8

The EXO-UL8 was designed with a single DoF hand module attached to the 3 DoFs wrist through a 6-axis force sensor. The part proximal to the force sensor, as well as a custom attachment from the force sensor to the dorsum of the OTHER Hand were designed. The attachments were constructed such that the anatomical wrist would align with the 3 DoFs of the EXO-UL8 while the hand is worn as shown in Fig. 3.15. When the motor pack and wrist attachments are connected to the EXO-UL8, the user does not need to exert their own energy to lift the OTHER Hand due to gravity compensation of the EXO-UL8. Additionally, the bulk of the forces applied on the hand by the Bowden cables are passively compensated for by the upper limb system.

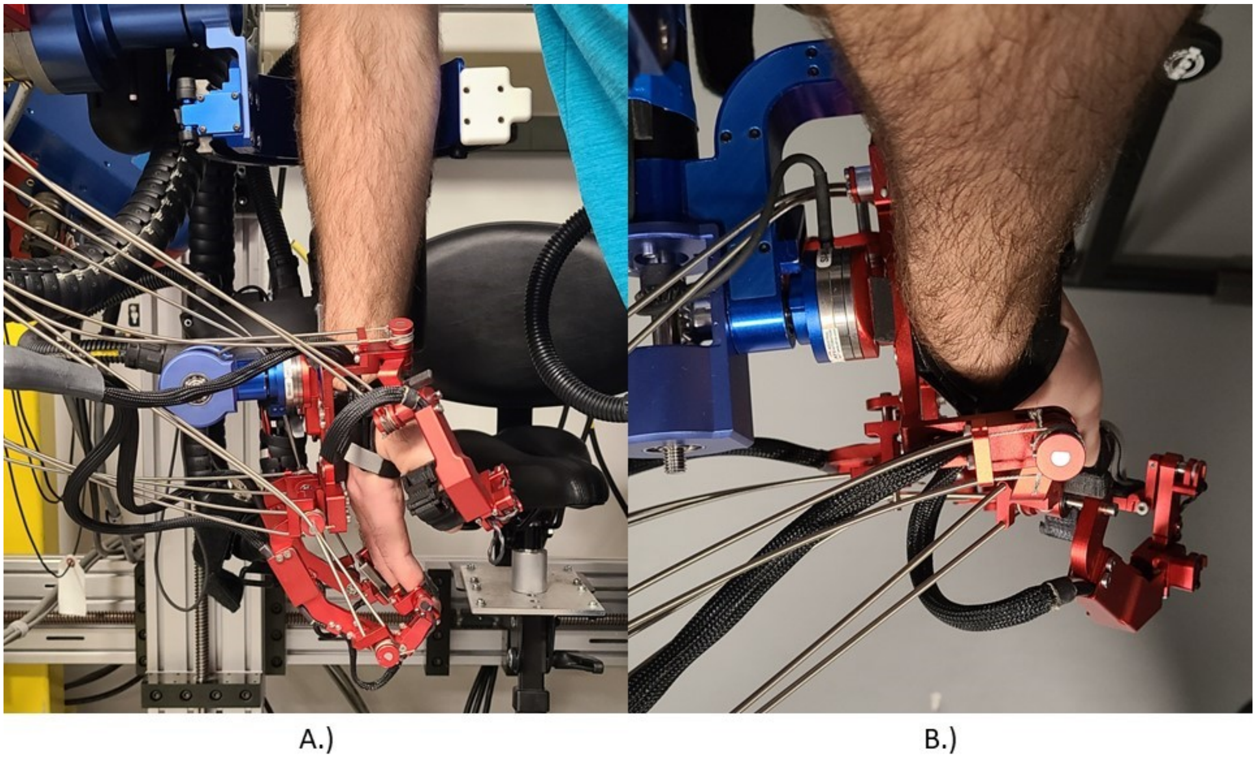
A.)
B.)

Figure 3.15: The OTHER Hand mounted at the wrist of the EXO-UL8. A.) Front view. B.) Top view.

3.9.5 Donning/Doffing

The quick disconnect finger attachments and clamping palm attachments were designed with the EXO-UL8 in mind. Specifically, the user can don the finger attachments before entering the exoskeleton, and can slide their hand into the palm attachment while positioned to attach to the EXO-UL8. Once hand is in place, the fingers, palm, forearm, and upper arm attachment points can then be easily secured.

3.9.6 Electronics and Software Integration

At present, the OTHER Hand and EXO-UL8 are not integrated from either a electronics or software perspective. No signals are sent between them, and each acts independently even when mechanically combined. However, methods have been proposed for integrating them.

Both systems use rackmount electronics enclosures and industrial PCs. Both also use the same model PCI cards for communicating with sensors and motors. If desired, all PCI cards can be placed on a single backplane with 13 PCI slots to centralize all control on a single PC. This, however, would require modifying routing of connections from the EXO-UL8 and OTHER Hand to share some analog in PCI cards. The backplane has been purchased, but system modularity has prioritized.

Regardless of electronic integration, software development by future graduate students is anticipated to enable connection of the control of the hand and arm exoskeletons. This would primarily involve the establishment of a standardized UDP packet for both the EXO-UL8 and OTHER Hand to use. These packets could then be used to enable independent or coordinated control of the systems. An overview of the potential organization of the software for a combined OTHER Hand and EXO-UL8 system is provided in Fig. 3.16 courtesy of Jianwei Sun.

3.10 Conclusion

This chapter presented the research effort on the development of the OTHER Hand exoskeleton. This exoskeleton is a novel one-size-fits-all, 3-linkage, 6 actuated and 8 passive DoFs, reconfigurable, rehabilitation hand exoskeleton designed to attach to upper limb exoskeletons. It features a lateral base-to-distal topology, quick disconnect attachments, a Bowden cable transmission system, integrated force sensors, and an opposable thumb. The design and assembly of the OTHER Hand has been completed. One pair of the exoskeleton hands have been delivered to Dr. Joel Perry for integration with the BLUE SABINO upper limb exoskeleton, and a second pair is installed on the EXO-UL8 as displayed in Fig. 3.12.

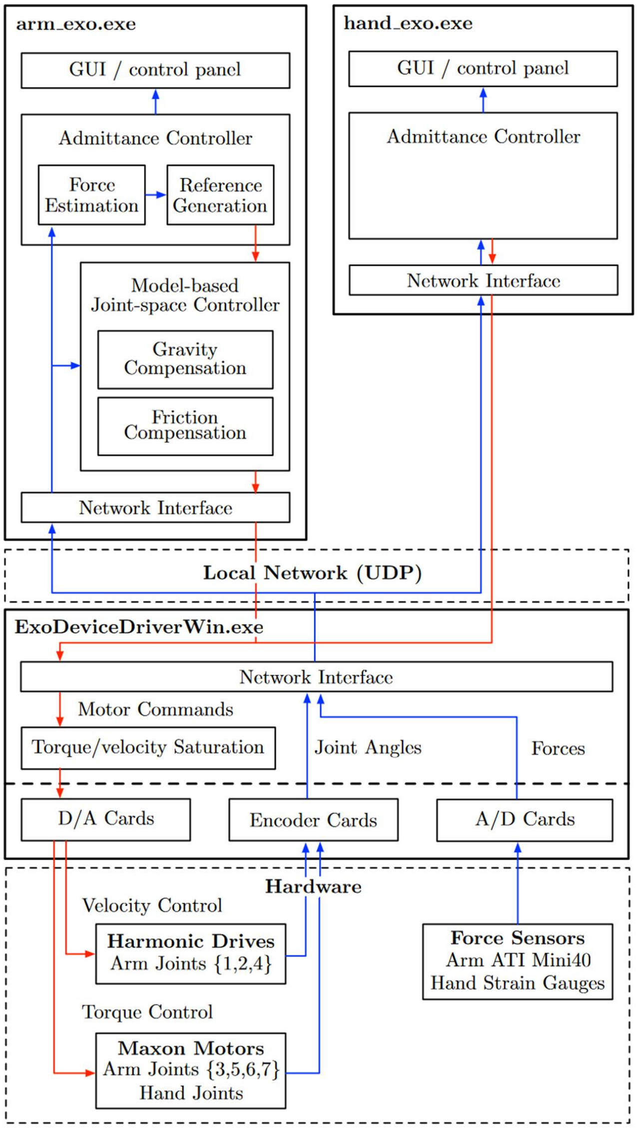

Figure 3.16: System overview of the anticipated software organization for the combined EXO-UL8 and OTHER Hand system.

CHAPTER 4

Experimental Evaluation of the OTHER Hand

Due to the high number of novel design features as well as the inaccuracies in the standard kinematic models of palms and thumbs, it is difficult to predict the functionality of the OTHER Hand without physical testing. This is doubly so because the system is not designed to work with a specific hand but rather the hands of the general population per the unisize requirement. In particular, it is uncertain how the physical structure of the OTHER Hand will interfere with grasping, if the system will be securely attached and comfortable to use, and if the thumb mechanism can provide the desired DoFs with the appropriate ROM for users with different size hands reflective of the range in the general population.

In order to demonstrate the capabilities of the OTHER Hand, a validated test protocol for grasping of real world objects was desired. This is due to the intended use of the OTHER Hand as a rehabilitation device; it must be capable of training the grasps and hand postures needed for ADLs. Of particular interest is the ability to perform the grasps on relevant physical objects. This is because doing so enables tactile and kinesthetic feedback when performing rehabilitation tasks, which is shown to increase motor and functional recovery [71]. Furthermore, the abilities of the OTHER Hand should be tested for a range of user hand sizes to validate the design choices enabling it as a one-size-fits-all device. Several protocols for testing various metrics of hands (robotic and biological) have been proposed, including applying Cutkowsky's Taxonomy [72] or the GRASP Taxonomy [40] (objects used are not standardized for either), the Action Research Arm Test [73] (also tests arm motions unrelated to hand design), or the Southamptom Hand Assessment Procedure [74] (measures function-

Figure 4.1: All tasks of the AHAP and the initial pose wearing the OTHER Hand. Tasks are labeled with task number and associated GTs. Note: all grasps are performed palm up.

ality as based on task completion time, which is not inherent to the OTHER Hand design). Given the goal of evaluating grasping abilities but *not* arm manipulation (that is a factor of the upper limb exoskeleton to which the OTHER Hand attaches), the *Anthropomorphic Hand Assessment Protocol* (AHAP) was selected [75].

4.1 Anthropomorphic Hand Assessment Protocol

Most standardized performance tests of robotic hands attempt to quantify kinematic and dynamic capabilities or test very specific tasks, such as pick-and-place. Metrics like workspace or actuation property comparisons to the human hand provide an overview of the anthropomorphism of the robot in terms of design specifications, however they do not address the ability to grasp real world objects [75]. Grasping ability is defined as the ability of the hand to both effectively initiate grasp and maintain a stable grip under motion without external forces of a representative set of objects used in ADLs [75]. The AHAP is designed to holistically measure the anthropomorphism of a robot hand operated by a human subject in terms of ability to replicate the most characteristic grasp types used in ADLs with the standardized set of physical objects of varying physical characteristics in the *Yale-CMU-Berkeley Object Set* (YCB) [75], [76]. The AHAP is also generalizable across arbitrary robot hand systems, and thus enables comparison between different designs [75]. This permits the demonstration of grasping ability for the range of hand sizes of users of one-size-fits-all exoskeletons such as the OTHER Hand.

10 *Grasp Types/hand postures* (GTs) including *Pulp Pinch or palmar pinch* (PP), *Lateral Pinch* (LP), *Diagonal Volar Grip or adducted thumb grip* (DVG), *Cylindrical Grip* (CG), *Extension Grip* (EG), *Tripod Pinch* (TP), *Spherical Grip* (SG), *Hook grip* (H), *Platform* (P), and *Index Pointing/pressing* (IP) are tested in the AHAP. These grasps account for more than 90% of grasps by frequency of use, and the non-grasping postures are included due to their importance [75]. Each grasp is tested with three different objects of varying size, shape, weight, texture, and rigidity, and each non-grasp posture is tested with a single object, obtained from all categories of the YCB [75], [76]. The GTs for each task, as well as the initial position formed prior to and at the end of each task, are shown with the OTHER Hand worn in Fig. 4.1.

4.1.1 Procedure

4.1.1.1 Modifications

The procedure largely follows the AHAP with two modifications:

1. The human hand within the OTHER Hand is considered for scoring purposes, and not the exoskeleton itself, with the exception of the palm of the OTHER Hand which is considered as part of the palm of the user. To do otherwise would prevent full scoring for many grasps despite correct posture of digits and secure grasp of the tested objects.
2. Before each repetition of each task, the subject is instructed to clench their hand into a fist with thumb in opposition to the palm. The initial pose for each task is not specified by the AHAP. The closed fist posture was selected to force users to pregrasp prior to grasping, further demonstrating the abilities of the OTHER Hand.

4.1.1.2 Pre-Trial Fitting and Donning

Prior to beginning the AHAP procedure, the OTHER Hand is adjusted to fit the user:

1. The subject is instructed on the format of the experiment and questions are answered.
2. The subject's index finger from center of rotation of the MCP joint to the fingertip (including soft tissues) is measured to the nearest millimeter and recorded.
3. The distance from the index finger MCP to the ring finger MCP joint is measured to the nearest millimeter, and the lateral placement of the right ring linkage of the OTHER Hand is adjusted to match this width.
4. The subject must don the finger attachments before donning the OTHER Hand. Assistance is provided by the operator if necessary.

5. The OTHER Hand is powered on and enabled through the GUI. All right finger linkages are enabled. Force measurements are zeroed. All right joint positions are reset. Admittance control is enabled, and the OTHER Hand is configured to be in a reasonable position for donning before force measurements are zeroed again.

6. The subject is instructed on the use of the emergency stop button. Specifically, to press the emergency stop with their left hand (which should be resting on the emergency stop) if the OTHER Hand moves in a way other than desired.

7. The subject sits in an adjustable-height chair with back support and without arm rests. The subject adjusts and/or positions the chair such that the platform is level with the navel and they are able to touch all four corners of the platform with their index finger without moving their torso. The subject is instructed to keep their back against the back support of the chair such that their face does not enter the video.

8. With assistance from the operator, the subject dons the OTHER Hand. Specifically, the subject's hand should be comfortably clamped and strapped into the palm and each finger attachment should be connected to the appropriate mechanism.

9. The subject must give verbal confirmation that they are comfortable before proceeding.

10. The subject is allowed up to three minutes to accustom themselves to use of the foot pedal and moving while wearing the OTHER Hand.

11. "Delete all data" should be clicked in the Data Logger on the GUI.

12. Webcam recording of top and side view is started. The subject is instructed to keep the OTHER Hand in view of the webcams when performing each task.

4.1.1.3 AHAP Trials

Tasks should be completed in numerical order of T_{01} to T_{26} with the objects from the YCB as shown in Fig. 4.1. All grasping and object manipulations should occur in view of the webcam. The operator should delete each logged data file that is not associated with a task. The subject should request a break whenever desired. For each task, the following steps are followed:

1. The operator shows the object and correct grasping posture/task to the subject, and explains any requirements of the task. Objects/grasp postures are found in Fig. 4.1. Requirements are listed in Table 4.1. [75]

2. The operator assists the subject in practicing the task for one minute [75].

3. The subject, with the OTHER Hand donned, forms a clenched fist with thumb opposed as the initial configuration.

4. The operator enables the foot pedal and presents the object to the subject for the test in a way that enables the subject to properly perform the grasp posture. For the IP task (T_{09}), the timer is fixed to the platform surface [75].

5. The subject operates the OTHER Hand with palm facing upwards to grasp the object. The operator releases the object as soon as it is grasped by the subject. For the IP task (T_{09}), the subject presses the button to start the timer, and then waits for three seconds [75].

6. While maintaining the grip, the subject naturally rotates the hand/arm with low acceleration until the palm faces downwards (180° rotation), and maintains the grip for three seconds in this position. For the IP task (T_{09}), the subject presses the button again to stop the timer within three seconds after the completion of step 5. This step is not executed for the P task (T_{18}) [75].

7. The subject returns the object to the operator [75] and forms a clenched fist again. The operator releases the foot pedal and renames the trial in the data logger to S*SubjectNumber*T*TaskNumber*R*RepeatNumber*.

8. Steps 4-7 are repeated two additional times (for a total of three repetitions) [75].

Upon completion of all tasks, video obtained from the webcam is saved. Additionally, "Save All As" is clicked in the graphical interface. Subjects are read the following five questions, asked to rate each on a 1-10 scale (1 worst, 10 best), and to provide comments on their experience with the OTHER Hand:

1. Comfort: The attachments to the hand are comfortable considering the palm and all finger attachments. 1 is too uncomfortable to use, 10 the attachments are so comfortable as to be unnoticeable.

2. Security: The attachments to the hand connect securely considering the palm and all finger attachments. 1 is completely insecure, 10 is completely secure.

3. Weight: How heavy or light is the sytem? 1 is too heavy to use, and 10 is so light as to be unnoticeable.

4. Movement: The system moves as desired in terms of control. 1 is the system never moving as desired and requiring great effort, 10 is always moving as desired and taking no effort.

5. Constraint: The system physically constrains/blocks desired motions and postures due to size, joint alignment, finger groupings, etc. 1 is always constrained, 10 is never constrained.

Table 4.1: Requirements for successful completion of each grasp [75].

Grasp/Posture Type	Requirement for Correctness
Index pointing/pressing (IP)	The palmar side or tip of distal phalanx of the index finger is contacting the object and starting the timer (stopping for maintaining grip score).
Platform (P)	There is contact between the object and the palm and the angle between any phalanx (long fingers and thumb) and the palm is less than 30°.
Hook (H)	There is contact between the object and the palmar side of at least three long fingers.
Spherical Grip (SG)	There is contact between the object and the palmar sides of the thumb, all the phalanges of at least three longer fingers, and the palm.
Tripod Pinch (TP)	The object is contacted by the radial side of the middle finger and by the palmar side of the distal phalanges of the thumb and the index finger.
Extension Grip (EG)	There is contact between the object and the palmar side of the distal phalanges and the intermediate phalanges (if exist) of at least three long fingers and the palmar side of the thumb. In any case, the angle between the distal phalanges axes and the object side must be less than 30°. For the boxes the contact of the thumb and finger phalanges must be in the opposing sides of the box with bigger area.
Cylindrical Grip (CG)	The angle between the main axis of the thumb and the main axis of the object's grip area is greater than 60° and there is contact between the object and the palmar sides of the thumb, all the phalanges of at least three long fingers and the palm.
Diagonal Volar Grip (DVG)	The angle between the plane defined by the thumb phalanges and the symmetry plane of the object is less than 30° and there is contact between the object and the palmar sides of the thumb, the palm and at least three long fingers.
Lateral Pinch (LP)	There is contact between the object and, at least, the palmar side of the distal phalanx of the thumb and the radial side of the index finger.
Pulp Pinch (PP)	The object contacts with the palmar sides of the distal phalanx of the thumb and the distal phalanx of only one long finger, without any contact of the object with the palm.

4.1.1.4 Scoring

For each task the scoring protocol in Table 4.2 is applied for each of the three repetitions, for for a maximum total *Grasping Ability Score* (GAS) of 153, which can be normalized [75]. Inter- and intra- rater reliability, internal consistency, and responsiveness to small changes in robot hand design of the GAS have all been found to be high [75].

Table 4.2: Scoring method for each trial of each task of the AHAP [75].

Step	Task	Score	Criteria
5	All except T_{09}	1	The grasp is completed with the correct grasp type given requirements.
		0.5	The grasp is different to the one specified given requirements.
		0	The object was not successfully grasped.
	T_{09}	1	The timer is pressed with the correct grasp type given requirements.
		0.5	The timer is pressed with a different grasp type given requirements.
		0	The timer is not successfully pressed.
6	All except T_{09} and T_{18}	1	No visible motion of the object with respect to the hand (for T_{19} only the portion of the rope located in the grasping area is considered).
		0.5	The object moves with respect to the hand but is not dropped.
		0	The object is dropped.
	T_{09}	1	The timer is pressed within three seconds with the correct grasp type given requirements.
		0.5	The timer is pressed within three seconds with a different grasp type given requirements.
		0	The timer is not successfully pressed within three seconds.
	T_{18}	N/A	No additional points for this task.

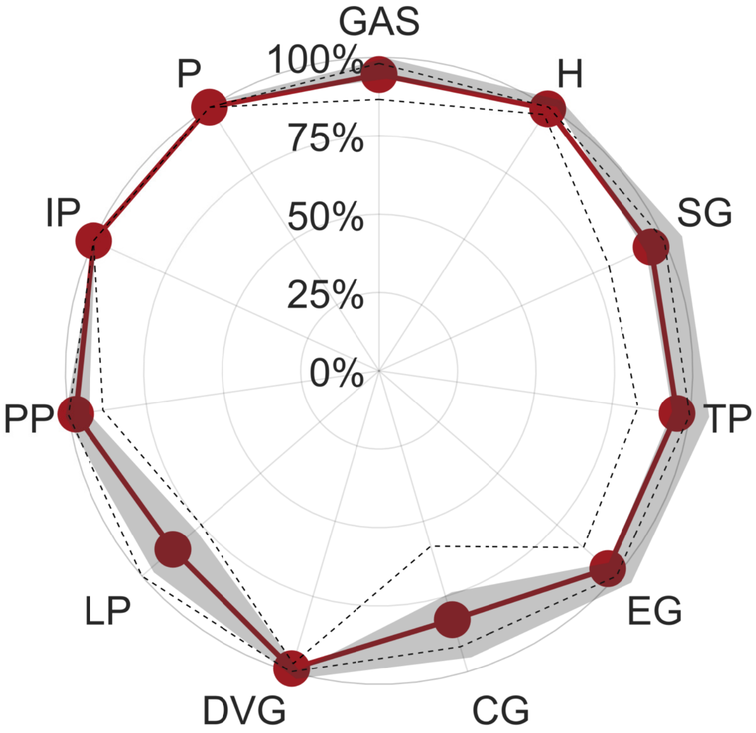

Figure 4.2: Normalized overall scores by GTs. The solid line displays the mean across subjects, the dashed lines the maximum and minimum, and gray shaded area ± one standard deviation from the mean (which can exceed the maximum/minimum).

4.1.1.5 Subject Criteria

The AHAP trials were completed by thirteen healthy subjects aged 24-34 (29.0±3.7, mean±standard deviation) with 31% self-identifying as female. Their index finger lengths measured 81.5±5.9mm, compared to 81.8±10.3mm of the general population [45]. Subjects fell between the 10.5th and 80.5th percentile for hand size assuming a normal distribution.

4.2 Results

The results of the AHAP testing of the OTHER Hand are displayed in Fig. 4.2. The mean and standard deviation for the GAS and GTs are listed in Tab. 4.3.

Most users were able to correctly grasp and maintain for each task, as evident in the mean 143.79 GAS. However, subjects often could not perform two of the CG tasks and two of the LP, and the P task was performed with a caveat.

Task 14, CG of the coffee can, was generally able to be grasped correctly. However, some subjects were unable to maintain because the low-friction between the hook-and-loop straps used for the finger attachments and the high weight of the object caused the can to slip from some subjects' fingers when inverted. Subjects with smaller hands that relied on friction, as opposed to circling the can, were especially likely to drop the object. The correct grasp was unachievable for Task 23, CG of the power drill. The lateral base-to-distal topology of the OTHER Hand resulted in too wide of a system for the four long fingers to fit on the handle of the power drill between the barrel of the drill and its battery pack. As such, no user was able to grasp the handle with contact between the object and the palmar side of all phalanges of at least three long fingers, as required. Instead, users made similar grasps that did not satisfy requirements for CG, and could generally maintain the grasp without motion of the object with respect to the hand.

Tasks 7 and 16 involve LP of the bowl and XS clamp, respectively. The lateral placement of the index linkage largely prevented correct grasping for both tasks. The only unobstructed area of the index finger on the radial size was at the distal portion of the distal phalanx. Only a few subjects with larger hands were able to grasp the objects with said area, and then only insecurely. Other subjects used a PP or similar grasp instead of the LP. The issue

Table 4.3: Scores by GTs.

GTs	Mean	Std. Dev.	GTs	Mean	Std. Dev.
GAS	143.79/153	5.31			
H	17.92/18	0.16	SG	17.13/18	1.18
TP	17.25/18	1.21	EG	17.29/18	0.82
CG	14.79/18	1.91	DVG	17.83/18	0.24
LP	15.54/18	1.56	PP	17.04/18	2.04
IP	6.00/6	0.00	P	3.00/3	0.00

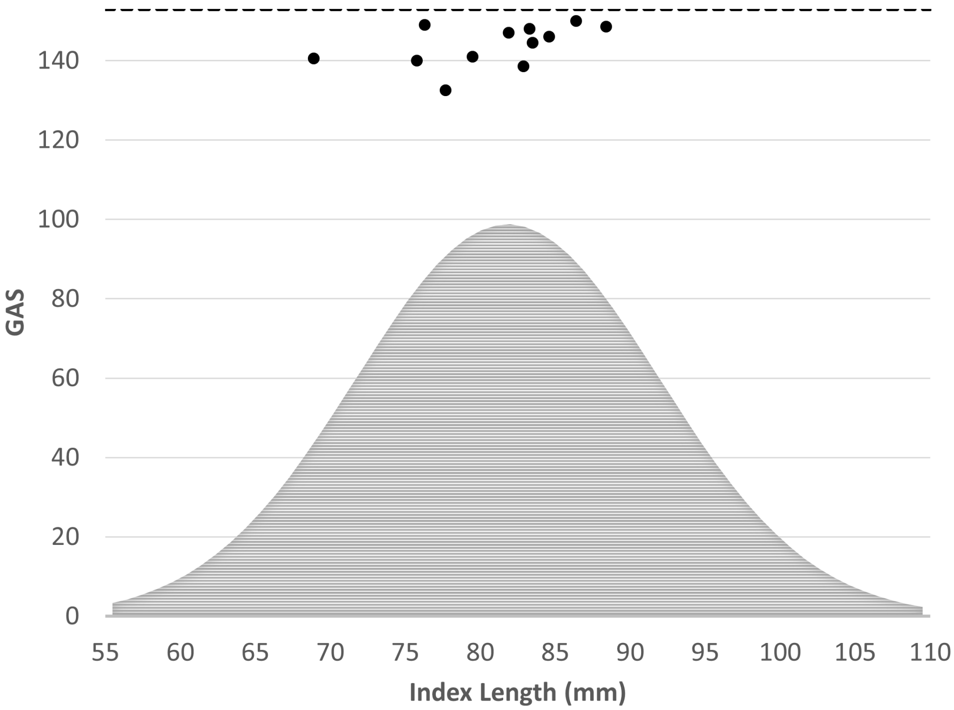

Figure 4.3: GAS versus hand size of test subjects as approximated by index finger length. Index length of population is displayed for reference as a normal distribution with mean and standard deviation from [45]. Max possible GAS is displayed with the dashed line.

preventing LP of the bowl and XS clamp was not an issue for the key, as it fit in the area and keys are generally grasped at the distal phalanx.

In addition to the noted challenging tasks, task 18 was performed unnaturally. Every subject performed the correct P posture according to the requirements of the AHAP, and successfully held the plate. However, the plate sat on the exoskeleton, and did not make direct physical contact with the subject's hand as seen in Fig. 4.1. Exclusion of the palm attachment for scoring would have resulted in a 0.5 score for all users for each repetition of this task.

The GAS of each subject is plotted against their hand size, as approximated by index finger length, in Fig. 4.3. While there is a moderate tendency for users with larger hands to score higher (Pearson correlation coefficient = 0.53), even the lowest-scoring subject scored a 132.5 (86.6%).

The average and standard deviation of the numeric scores given in the post-trial questionnaire are reported in Table 4.4.

4.3 Discussion

The high overall score of the OTHER Hand on the AHAP across all users indicate that the novel design choices resulted in a unisize system able to perform the wide range of grasps needed for ADLs. The mean normalized GAS of the OTHER Hand was 94.0% ± 3.5%. This is notably higher than the 45-79% reported for various designs [75], [77]–[79], although it is an exoskeleton as opposed to the prosthetic and robotic hands tested with the AHAP in the literature. All subjects, from 10.5th to 80.5th percentile hand size, scored higher than any reported prosthetic or robotic hand. It is therefore deemed that the OTHER Hand did not greatly hinder healthy grasping performance. Importantly, the novel thumb O/R axis enabled the desired thumb motions of the subjects, and several even expressed surprise when informed that one DoF of the thumb was actually constrained.

Based on observations during the trials, a 10th percentile hand is the smallest that can operate the OTHER Hand without limiting thumb ROM during simultaneous extension and opposition, due in part to joint stops. Although not the 5th percentile designed for, this is not unexpected. The link-length optimization accounted for F/E but not O/R motions that were only approximated with a single DoF. For subjects with smaller hands, the linkages extruded far past the biological fingers when extended. While this didn't prevent grasping of any of the tested objects, it did require subjects to be cautious in their approach to objects

Table 4.4: Responses to post-trial questionnaire.

Comfort	Security	Weight	Movement	Constraint
6.92 ± 1.26	5.38 ± 2.02	6.84 ± 1.41	8.69 ± 0.63	6.15 ± 1.57

to avoid collision. These factors, along with challenges of smaller hands grasping the coffee can in task 14, may give users with larger hands a slight advantage in GAS.

Subjects' comments in after-experiment discussions were also generally positive, particularly with regards to the ease, comfort, and naturalness of the motions. Comfort was noted to be moderate, though modifications to the padding of the palm attachment may be beneficial. Weight of the system was also generally judged to be decent, with no subject assigning a score below a 5. However, the questionnaire also informed where improvements can be made, particularly the finger attachments. The security of each finger attachment varied between digits and subjects. After two of the first five subjects expressed difficulty and frustration in keeping the thumb attachment on, which was then just a hook-and-loop strap to the distal phalanx, the attachment was redesigned. For subjects 6-13, the attachment was a double parallelogram mechanism attached at both the distal and proximal phalanges. This improved the mean Security of attachment score from 4.8 for subjects 1-5 to 5.75 for subjects 6-13, and the later subjects were generally more positive with their comments on the security of the thumb attachment. However, the index and pinky attachments, which remain single hook-and-loop straps secured to the distal phalanges, and different subjects were more or less prone to falling out of one or the other. Additionally, the hook-and-loop straps were noted to be slippery and challenging to don sufficiently tight by the subject alone. Therefore, future work will focus on improving the finger attachments. Comfortable and secure finger attachments were identified early-on as an issue not sufficiently solved by the hook-and-loops straps. The quick disconnect mechanisms permit redesign of just the finger attachments, without modifying the rest of the system.

Further, the experiments highlighted that lateral placement of the index linkage obstructed specific grasps for several objects, particularly for LP of large objects. This was the primary complaint that resulted in the lower score in the Constraint category. It is still judged that the combined benefits of zero final link length and shorter linkage are worth the lateral placement. However, modifications to the structure or topology to reduce the

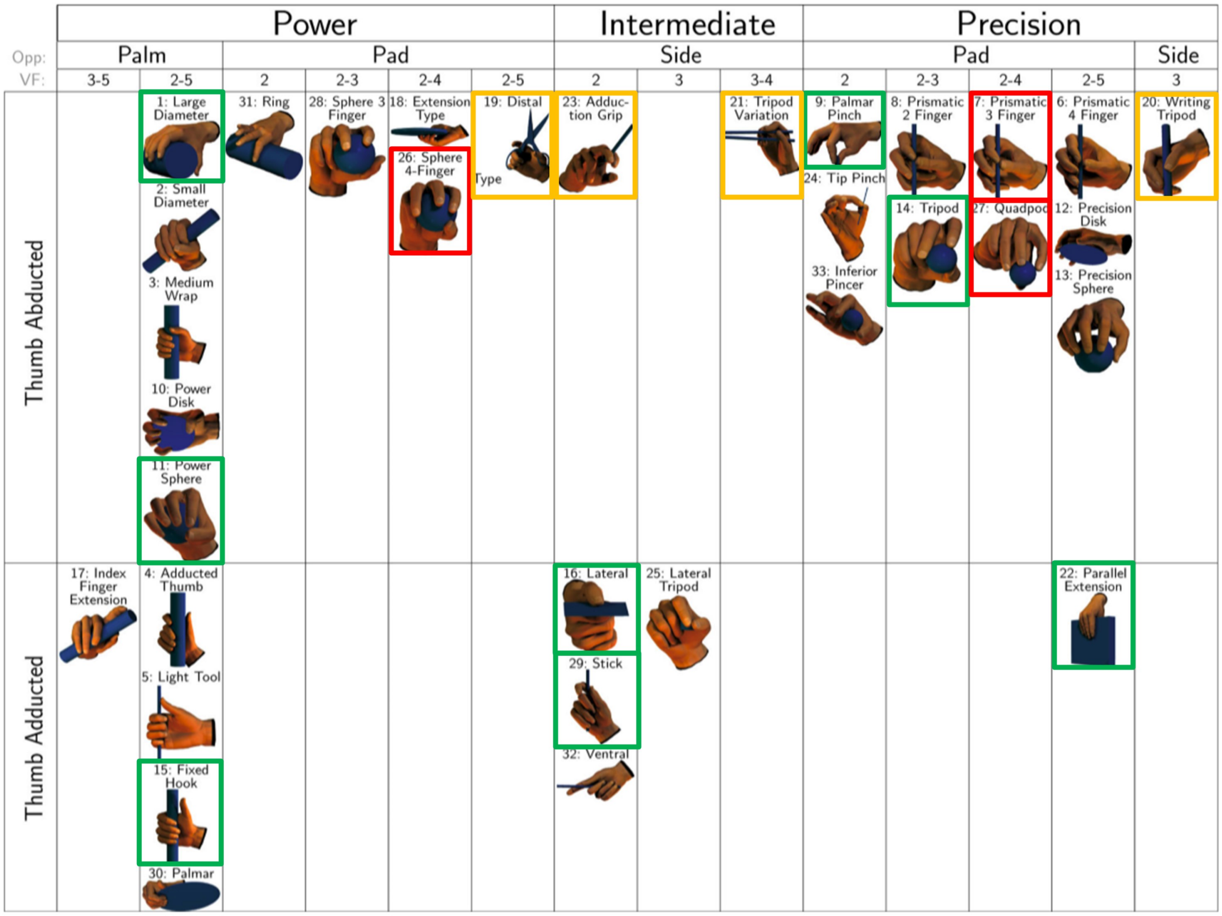

Figure 4.4: The 33 everyday prehensile grasp types from [40]. Grasps tested by the AHAP are highlighted in green, those unachievable by the OTHER Hand are in red, and those achievable but uncontrollable in yellow.

structure on the radial side of the index finger may be beneficial in future generations.

Beyond the eight prehensile grasps and two hand postures tested with physical objects by users of varying hand sizes in the presented study, it is expected that the OTHER Hand is capable of forming the vast majority of prehensile grasp types that humans commonly form. These grasps types have been systematically categorized by other researchers, and modern models have settled on 33 prehensile grasps [40], [80] shown in Fig. 4.4. Of these grasp types, 3 are unachievable by the OTHER Hand due to independent motion of the pinky relative to the ring finger, and are highlighted in red. Three additional grasps are deemed to be formable but unassistable, and are highlighted in yellow. These grasps depend on A/A of the fingers or fine orientation changes of the distal phalanges, neither of which the OTHER Hand can control. Equivalent prehensile grasps to those tested are highlighted in green. It should be noted that not all of the eight grasps in the AHAP neatly fall into single grasp categories, and some might be considered additional grasps depending on which object was grasped.

In addition to testing via the AHAP, the OTHER Hand has been mounted to the EXO-UL8, and initial work on integrating software and control of the systems has begun. Preliminary performance ability of bimanual reach-to-grasp tasks and ADLs appears promising, however thorough investigation and system integration are future work.

4.4 Conclusion

The experimental evaluation of grasping ability of the OTHER Hand using the AHAP confirmed what was anticipated but challenging to model, namely that the system is capable of performing the wide variety of grasps and hand postures that are commonly found in ADLs. Across hand sizes ranging from 10.5th to 80.5th percentiles, subjects were able to obtain higher GAS scores than any reported robot or prosthetic hand. Although being an exoskeleton likely provides advantages in this regard, it still demonstrates that the OTHER Hand does not significantly hinder ability to make anthropomorphically standard grasps. The mean normalized GAS was found to be 94%, indicating the potential of the system to train ADLs.

The testing also highlighted certain aspects of the OTHER Hand that need future improvements. Primary among these needed improvements are better attachments. The finger attachments, with the exception of the combined ring/middle finger portion, were found to be less secured than desired. Meaningful improvements were made to the thumb attachment by converting to a remote-center-of-motion double parallelogram mechanism. The subjective rating for security of attachments remained comparatively low though. An alternative method of securing to the fingers compared to hook-and-loop straps is expected to be needed for the system to be tolerable by users already suffering from movement impairments due to stroke and other conditions. However, though these improvements may make significant impacts on the ease and comfort of use of the system, they are not expected to need a significant system redesign as was the case between the first generation hand and the OTHER Hand.

CHAPTER 5

Autonomous Tissue Manipulation via Surgical Robot Using Approximate Q-Learning

The following chapter is adapted from the conference paper titled “Toward Synergic Learning for Autonomous Manipulation of Deformable Tissues via Surgical Robots: An Approximate Q-Learning Approach” published in the 2020 8th IEEE RAS/EMBS International Conference for Biomedical Robotics and Biomechatronics (BioRob) co-first authored with Sahba Aghajani Pedram [81].

5.1 Abstract

In this paper, we present a synergic learning algorithm to address the task of indirect manipulation of an unknown deformable tissue. Tissue manipulation is a common yet challenging task in various surgical interventions, which makes it a good candidate for robotic automation. We propose using a linear approximate Q-learning method in which human knowledge contributes to selecting useful yet simple features of tissue manipulation while the algorithm learns to take optimal actions and accomplish the task. The algorithm is implemented and evaluated on a simulation using the OpenCV and CHAI3D libraries. Successful simulation results for four different configurations which are based on realistic tissue manipulation scenarios are presented. Results indicate that with a careful selection of relatively simple and intuitive features, the developed Q-learning algorithm can successfully learn an optimal policy without any prior knowledge of tissue dynamics or camera intrin-

sic/extrinsic calibration parameters.

5.2 Introduction

Robot-Assisted Surgery (RAS) is becoming the norm of many operating room procedures, as it enables enhanced precision, dexterity, and feedback. Compared to conventional *Minimally Invasive Surgery* (MIS) and/or open surgery, however, RAS restricts paramount information such as haptic feedback and direct vision from the surgeons. These deficiencies make surgical sub-tasks such as suturing or tissue manipulation very challenging for, and demand high cognitive loads from, surgeons [82]. To reduce the surgeon's burden, recent work has begun on automation of specific MIS tasks including suturing [83]–[85], tissue manipulation [86], [87], tissue dissection [88], and drilling [89], [90]. Robotic automation of these tasks would place surgeons in a supervisory position and could reduce the physical and cognitional strain of the operation. Hence, robotic automation has great potential to improve surgery, and therefore patients' outcome.

A particular task of interest in various MIS interventions (e.g. tumor dissection and tissue debridement) is tissue manipulation, as shown in Fig. 5.1. Due to the uncertain deformation behavior of tissue, however, this manipulation task is challenging even for expert clinicians. The main sources of this complication are homogeneous/heterogeneous physical or geometrical properties of deformable tissue such as stiffness and viscoelasticity which are unknown and hard-to-model [91]. Recent advances in machine/robot learning fields have enabled them to learn very complicated mappings and/or tasks [92], [93]. Hence, in order to lessen the surgeon's burden during RAS, learning-based autonomous tissue manipulation strategies are reasonable paths to explore.

From a clinical perspective, tissue manipulation tasks in MIS can be defined in various ways. This includes placing some points on the tissue to desired locations, or applying force to achieve and maintain certain tension of specific tissues. As a first step, we select the

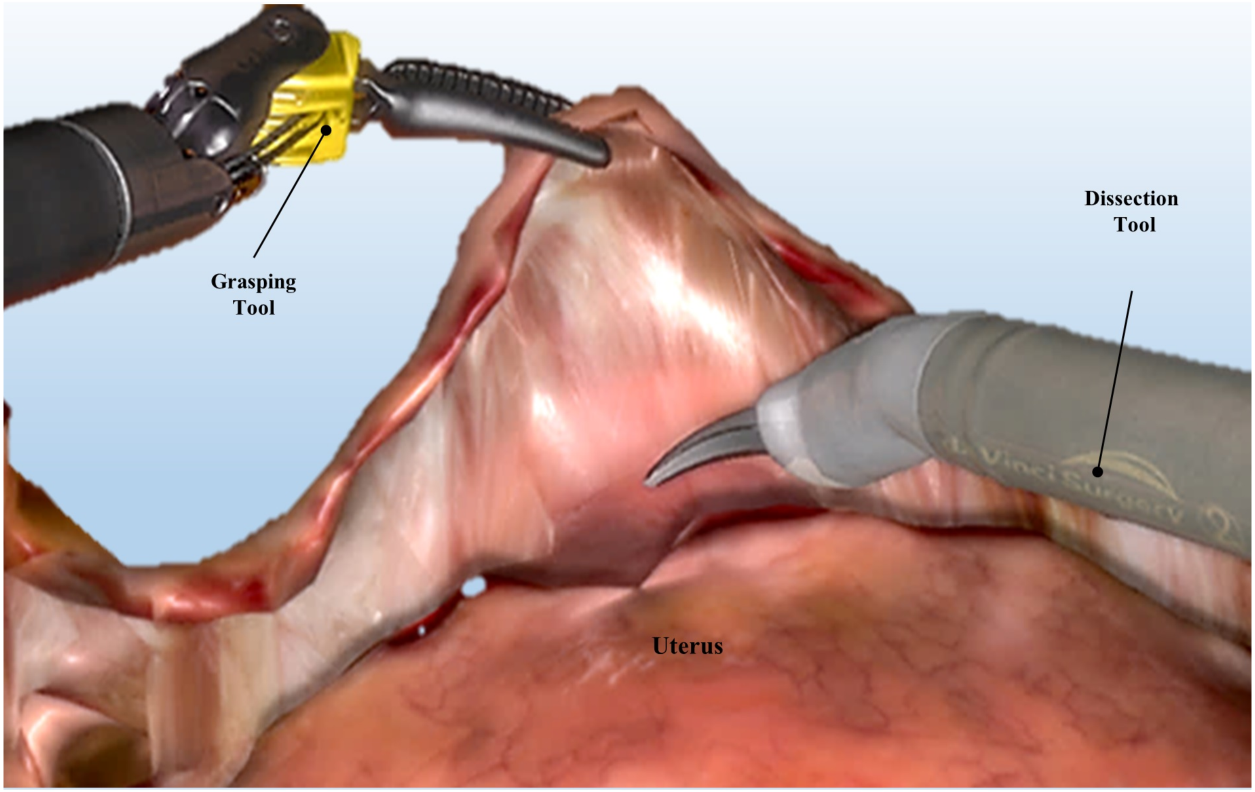

Figure 5.1: Example of an MIS tissue manipulation during a tissue debridement procedure.

former method and define three sets of points: a grasp location, a point on the tissue to be moved, and a desired location of the point on the tissue. In general, it cannot be assumed that any of these points of interest initially coincide. Of specific interest is that the grasp location may not be the same as the point on the tissue to be moved. This scenario is the case of 'indirect' tissue manipulation, where the point of clinical interest to be moved is inconvenient or impossible to grasp. Such cases frequently arise in surgery, such as in a suturing task where the insertion point of the needle must be placed at a desired location but it cannot be grabbed directly as it would prevent needle insertion.

Several researchers have attempted different methods to address the task of deformable object/tissue manipulation. These methods can be classified into two broad categories based on whether they deploy human knowledge about physics of the problem or purely rely on the machine learning capabilities. The first category, which we refer to as *human-knowledge driven* algorithms, incorporate explicit human knowledge about the model of the tissue and/or manipulation task. For example, indirect positioning of a deformable object based on a linearized second order model was proposed in [94]. Reference [95] comprehensively reviews manipulation of deformable objects where algorithms deployed human knowledge in their methodologies explicitly. The second category of methods, which we refer to as *machine-knowledge driven* or *data driven* algorithms, encompass algorithms in which machines deploy data to build knowledge of the tissue and/or manipulation task. For example, an optimization framework with an online Jacobian update was used to learn the dynamics of the tissue manipulation task [86].

Due to unknown or large inter- and intra-subject variability between biological tissues in complex surgical scenarios, data driven approaches may be viewed as a more appropriate solution. However, these methods (i.e. [96], [97]) do not incorporate prior human knowledge into their solution, and thus may require large amounts of data to train which is both expensive and time-consuming [98]. For real-world robotics applications, methods of choice are data-driven algorithms which use more suitable and task-specific representations [99]–[101]. Hence, in the case of robotic tissue manipulation, a *Synergic Learning* (SL) algorithm which combines basic human knowledge about the physics of the problem with a learning algorithm is of interest.

To explore the performance of a SL algorithm in autonomous manipulation of deformable tissues, we propose an approximate Q-learning algorithm. For this algorithm, human knowledge contributes to selecting useful yet simple features of tissue manipulation while the algorithm learns to take optimal actions and accomplish the task. Q-learning [102], [103] is among the most popular reinforcement learning algorithms in which the agent learns to take optimal actions without explicitly building knowledge of the system dynamics and/or control. Q-learning has already been successfully applied to a range of challenging robotics problems [104].

5.2.1 Contribution

The tissue manipulation problem has already been approached by many researchers in [90], [94], [105] which have used either human-knowledge or machine-knowledge driven algorithms. In this paper, to the best of the authors' knowledge, for the first time, we propose an SL algorithm based on feature-based linear approximate Q-learning approach, which combines human knowledge with the learning algorithm to address this problem. In fact, we demonstrate that upon careful selection of simple yet effective features and reward, the developed linear approximate Q-learning algorithm is capable of accomplishing the desired manipulation task without any prior knowledge of tissue deformation behavior or camera calibration.

5.3 Methods

5.3.1 Problem Definition

This paper targets the task of indirect tissue manipulation with surgical robots that pinch *Tissue Grasp Point*s (TGPs) to place *Tissue Target Points* (TTPs) at *Image Desired Point*s (IDPs), shown in Fig. 5.2b. The tissue phantom is manipulated at two TGPs representing the grasp locations of a surgical robotic system such as the Raven [106]. In operating rooms, TGPs , TTPs, and IDPs could be selected by the surgeon.

Q-learning is a popular *Reinforcement Learning* (RL) algorithm that attempts to find (near-) optimal policy by learning the Q values of the underlying Markov Decision Process and taking an action that maximizes Q at a given state. The most thorough form of Q-learning is to create a table of Q values for each possible state-action pair which suffers from the curse of dimensionality problem [107]. To remedy this problem, in our SL framework the Q values are approximated with a linear function of features that are input based on human knowledge of the problem.

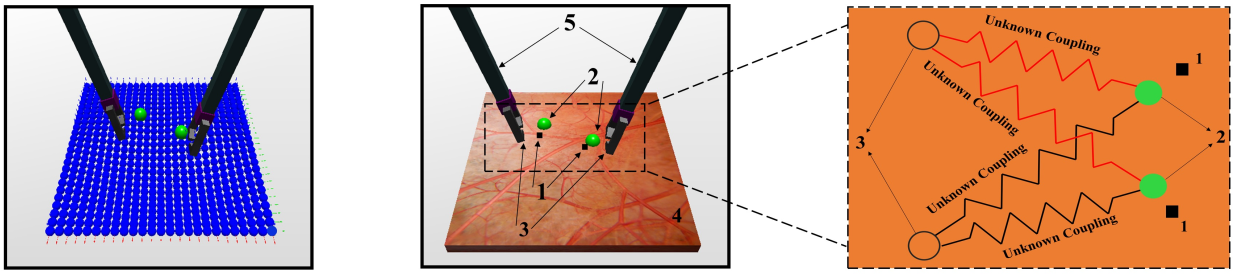

(a) (b) (c)

Figure 5.2: Simulation Environment. (a) All nodes used in the gel simulation (blue) with TTPs highlighted (green). (b) Components of interest: 1) IDPs, 2) TTPs, 3) TGPs, 4) simulated tissue, and 5) graspers. (c) Representation of intuitive coupling between TTPs and actions of TGPs (1, 2, and 3 are as defined).

5.3.2 Tissue Manipulation with Approximate Q-learning

As stated, the goal of the tissue manipulation task is to (indirectly) manipulate the TTPs to IDPs. Since the dynamics of the system (tissue) are not known *a priori*, this problem can be viewed as an RL problem. Moreover, while camera calibration (intrinsic and extrinsic) information may be available for a surgical robotic system, it might not be accurate or may vary when the experimental parameters are changed. Hence in this paper we assume the robot has no camera calibration information to account for real RAS scenarios.

5.3.2.1 Approximate Q-Learning

To incorporate human knowledge into solving the RL problem as well as to avoid the curse of dimensionality, we deploy a linear function approximation approach [107], [108] to approximate the Q function values given state and action ($Q^*(s,a) \approx Q(s,a;w)$):

$$Q(s,a;w) = \sum_{i=1}^{N} w_i f_i(s,a) \tag{5.1}$$

where N is the number of features, w_i is the i^{th} weight, w is the vector of weights, and f_i is the i^{th} basis function.

This method allows incorporating human knowledge by handcrafting basis functions (known as *features*) to create the function approximator. Although features must be selected with domain specific knowledge, in real-world robotics applications learning algorithms with task-specific representations/knowledge are suggested [101]. In fact, in this paper we show that by carefully selecting simple yet effective features, a linear function approximator is rich enough to capture and accomplish the very complicated task of robotic manipulation of deformable tissue.

In linear approximate Q-learning, the weights, w in (5.1), are updated to reduce the expected value of error norm (usually 2-norm) between the unknown $Q^*(s, a)$ value and the value of the Q approximator [109], [110]:

$$L(w) = \mathbb{E}\Big[\Big(Q^*(s,a) - Q(s,a;w)\Big)^2\Big] \tag{5.2}$$

where

$$Q^*(s,a) = \mathbb{E}\Big[R(s,a,s') + \gamma \max_{a'} Q(s',a')\Big] \tag{5.3}$$

and s, a, R, γ, s', a' are the current state, action, reward, discount factor, next state, and any possible action respectively. Differentiating the loss function in (5.2) with respect to w, we obtain the gradient (∇) as:

$$\nabla = \mathbb{E}\Big[\Big(R(s,a,s') + \gamma \max_{a'} Q(s',a') - Q(s,a)\Big) f(s,a)\Big] \tag{5.4}$$

where w is then updated based on gradient decent. In (5.4), $f(s, a)$ is the vector of features.

5.3.2.2 States and Actions

The actual state of the problem contains the location of all of the nodes of the simulated tissue, which is intractable for computational purposes. Since the goal for tissue manipulation is to accurately move the TTPs to IDPs , we approximate the states of the system by only the x and y pixel coordinates of each of TTPs in image space (i.e. $s \in \mathbb{R}^4$).

Although actual surgical robot manipulators are capable of moving in three dimensions, in order to simplify the problem and enable the use of a single camera image, we constrained the motion of the TGPs to a plane parallel to and above the tissue surface. To reduce the action space dimension, an action set consisting of staying still, moving up, down, left, or right was selected for each TGP (i.e. $a \in \mathbb{R}^2$). This selection resulted in 5 possible actions for each TGP and, therefore, a total of 25 possible actions for both TGP points. Of note, all actions are defined in robot base frame as camera calibration information is assumed to be unavailable.

5.3.2.3 Reward

We deploy reciprocal Euclidean norm of the pixel error between IDPs and TTPs:

$$R(s, a, s') = R(s) = \frac{1}{\sqrt{e^T e + \epsilon_s}} \tag{5.5}$$

where $e \in \mathbb{R}^4$ is the pixel error vector between IDPs and TTPs. Note that the pixel information of TTPs is obtained with an image processing thread and ϵ_s is a small number (10^{-8}) to avoid reward divergence to infinity.

5.3.2.4 Features

In order to satisfactorily build a good linear approximation function for $Q^*(s, a)$, it is necessary to select a set of features that can properly distinguish what is a good action in a given state for the task of tissue manipulation. The only simple human reasoning needed to select such features is that the actions from TGPs (instruments) changes the states of TTPs, which implies unknown coupling between them (see Fig. 5.2c). We embed these couplings into our Q-learning framework by selecting features in the form of x or y distances between each TTP and corresponding desired points, multiplied by all permutations of actions from TGPs (represented by numeric values). For the x actions of the k^{th} ($k \in \{1, 2\}$) TGP, a_{kx} is set to -1 for an action in the negative x direction, 0 for no movement in the x direction, and +1 for an action in the positive x direction. Similarly, for the y actions of the k^{th} ($k \in \{1, 2\}$) TGP, a_{ky} is set to -1 for an action in the negative y direction, 0 for no movement in the y direction, and +1 for action in the positive y direction. Therefore, a total number of 16 (4 couplings × 2 relative x or y pixel positions between TTPs and IDPs × 2 TTP-IDP pairs) features are selected which can be expressed in the form:

$$f_i(s, a) = (d_{kl} - t_{kl})\ a_{pq},\ \ i = 1, 2, ..., 16 \tag{5.6}$$

where d and t represent IDP and TTP respectively, $k, p \in \{1, 2\}$ indicating the k^{th} or p^{th} point, $q, l \in \{x, y\}$ indicating the coordinate or direction. These features work to consider how the action of each grasp point affects the x and y distances between each target point and corresponding desired point. However, none of these features will output the "no move" action. Intuitively, the TGPs should stop moving if the task is complete and the TTPs are very close to the IDPs. To enable this functionality, a 17^{th} feature was added that is essentially a Boolean statement to output a 1 if the reward is above a certain threshold and the "no move" action is selected. It can be formulated as:

$$f_{17}(s, a) = \begin{cases} 1, & \text{if } R(s, a = 0, s') > 0.08 \\ 0, & \text{otherwise} \end{cases} \tag{5.7}$$

The threshold selected was 0.08, which roughly corresponds to when the target points mostly overlap the desired points in the image. Increasing or decreasing the threshold therefore correspondingly changes the amount of training needed.

5.3.2.5 Episodic Training

It is unlikely for random actions along a single trajectory to explore a wide variety of state-action pairs. Hence, a training episode structure was used where the state configuration is reinitialized at the beginning of each episode with a total number of N_{action} actions. This is repeated for a total number of $N_{episode}$ episodes.

5.3.2.6 Exploration Strategy

To properly train a Q-learning algorithm, it is necessary to find a balance between exploring unknown state-action pairs and exploiting the current optimal policy. This is known as *exploration-exploitation trade-off* in the literature [104]. Some of the standard methods that were attempted for this task include ϵ-first, ϵ-greedy, and ϵ-decreasing. The most success was an ϵ-decreasing strategy according to (5.8)

$$\epsilon = \max(0.1, 1 - \frac{N_{action} \times n_{episode} + n_{action}}{N_{action} \times N_{episode}}) \tag{5.8}$$

where n_{action} is the number of actions that have been taken in the current episode, $n_{episode}$ is the current episode number from 0 to $N_{episode} - 1$.

5.3.2.7 Learning Rate and Discount Factor

The learning rate, α is the step size in the gradient descent of updating weights in (5.4). There is a trade-off between smaller or larger values of learning rate. The larger α will enable faster convergence but has a potential for divergence while smaller α has higher chance for convergence. A common strategy for learning rate is to set it to the following form for some constant K:

$$\frac{K}{K + N_{action} \times n_{episode} + n_{action}} \tag{5.9}$$

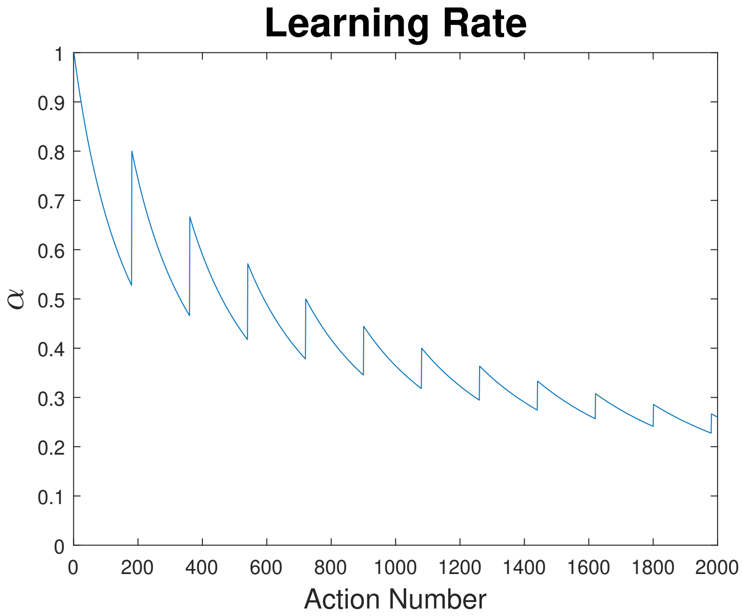

Figure 5.3: Cyclical decreasing learning rate, α, as a function of action number.

However, when this was tested in the given task it typically caused convergence to a solution that was notably sub-optimal. As such, a more advanced strategy was selected for α that consists of a periodic decreasing function as seen in Fig. 5.3. Such cyclical decreasing learning rates are proposed in [111]). This was chosen as it should cause convergence of weights as the number of actions approaches infinity, but also periodically resets the learning rate to a higher value to overcome saddle points and correct for noise due to visual occlusion. The period of the oscillation was chosen to be $0.9 * N_{action}$ so that the learning rate would spike at varying points during the training episodes, giving the opportunity to learn not just when close to the initialized locations. Discount factor was set to $\gamma = 0.9$.

5.3.2.8 Approximate Q-learning Algorithm

The general procedure of the approximate Q-learning algorithm for training used in this paper is detailed in Algorithm 1. After training, ϵ is set to zero, w_i stops updating, and deterministic optimal trained policy is used for testing.

5.4 Simulation Study and Evaluation

To evaluate the efficacy of the proposed SL algorithm based on linear approximate Q-learning for robotic tissue manipulation, we first developed a simulation environment. We then designed tissue manipulation simulation experiments based on real surgical scenarios and evaluated the performance of the algorithm from both learning and tissue manipulation point of views.

5.4.1 Simulation Environment

The simulation environment was created using CHAI3D [112]. OpenCV library [113] was deployed for image processing purposes. Fig. 5.2 depicts the simulation environment.

The high frequency (∼1 kHz) *Dynamics Thread* solves the underlying *Partial Differential Equation*s (PDEs) in real time to update the position of each node (shown by blue spheres in Fig. 5.2a). The low frequency (∼60 Hz) *Graphics Thread* receives the data from the dynamics thread and renders the image by updating the image pixels. This rendering is internally taken care of by means of OpenGL library [114]. For the purpose of this work, a new thread, *Image Processing Thread*, was added that runs at (∼60 Hz) and performs image filtering to obtain an estimate of the states for the problem.

5.4.1.1 Simulation Model

The GEL module of the open-source CHAI3D library [112] is used to simulate the motion/force of a real deformable tissue. The model consists of a rectangular prism structure of $25 \times 25 \times 1$ *Nodes* (see Fig. 5.2b). The nodes of each lateral surface of the model are held fixed. Each node is connected to its adjacent nodes by means of *Links* which specify how the motion of the nodes affect each other. The model takes into account the physical properties of each node (i.e. mass and radius) along with the physical properties of each link (i.e. linear and rotational stiffness and damping). This general structure is then used to calculate the interaction forces and dynamics of the tissue. For the purpose of this paper, additional software was developed so any node can be grasped and moved.

5.4.1.2 Vision Algorithm

Since in real surgical scenarios the IDPs are expressed in endoscopic images by surgeons, proper image processing should be used to extract TTPs pixel information from the images in real time. The image processing thread receives the frame buffer of the CHAI3D virtual camera at 60 Hz which could be replaced by an endoscopic frame buffer for software testing on an actual robotic surgery system. While more advanced algorithms (i.e. based on Convolutional Neural Nets [115]) could be used for tracking TTPs, in this work we use filters including Gaussian Blur and color-based HSV for image processing. The x and y center of the smallest circle containing all the identified TTP pixels are used to represent the position of the TTPs.

Algorithm 1 Approximate Q-learning

```
set $n_{episode}$ to 0
set $N_{episode}$ and $N_{action}$ values
initialize weights to random numbers uniformly distributed between -0.5 and 0.5
while ($n_{episode} < N_{episode}$) do
    initialize configuration of simulation environment
    set $n_{action}$ to 0
    increase $n_{episode}$ by 1
    while ($n_{action} < N_{action}$) do
        set $\epsilon$ and $\alpha$
        select $\epsilon$-greedy action $a$
        calculate all $f_i(s,a)$ and $Q(s,a)$
        take action $a$
        calculate $R(s,a,s')$ and $\max_{a'} Q(s',a')$
        update all $w_i$ according to (5.4)
        increase $n_{action}$ by 1
```

5.4.1.3 Q-Learning Algorithm

Once the Vision Algorithm obtains an estimate of states (positions of the TTPs), it inputs the estimated states to the Q-learning algorithm (Algorithm 1) upon a query. State estimation is then used to calculate $f_i(s,a)$, $Q(s,a)$, $R(s,a,s')$ and $\underset{a'}{max}\ Q(s',a')$ and it takes ϵ-greedy action a.

5.4.2 Simulation Experiment Design

To design the experiments, we considered realistic situations that might happen during a robotics tissue manipulation procedure. For instance, locations of TGPs and IDPs are defined based on the clinical situations, surgical sites, and the preference of the surgeon. Therefore, the utilized manipulation algorithm must be robust to these variations. A relevant example for autonomous tissue manipulation is an anastomosis, where two tissues must be accurately positioned adjacent to each other for proper suturing. Moreover, although the camera calibration data may be available during real surgical robotic procedures, it may not be accurate or may vary when the experimental parameters are changed. Hence, it is highly desirable that the algorithm performance be independent of camera calibration and/or configuration. Considering these realistic cases, the performance of the algorithm was assessed on four different configurations, as shown is Fig. 5.4. In the first three sets of experiments, the initial configurations of all TGPs , IDPs , and TTPs were changed (CASE I). For the fourth experiment, in addition to changing these points, the camera location was also altered (CASE II).

5.4.3 Performance Evaluation Metrics

To evaluate our algorithm, we assessed its performance from the learning point of view as well as the tissue manipulation perspective. In this regard, the learning performance was measured based on the reward during training episodes and error during testing. The tissue

Figure 5.4: Example successful policies. Four configurations (C1-C4) are displayed for representative progressing actions during testing episodes from (a) *initialization* to (d) *task completion*. Each configuration represents a different set of initial TTPs, IDPs, and TGPs. Additionally, in (C4), the camera configuration is changed. In order to maintain simulation stability, it was necessary to manipulate TGPs via simulated springs with low stiffness connected to the graspers. As such, small gaps between graspers and the tissue are observable for large deformations.

manipulation task was considered accomplished based on the Root Mean Square (RMS) error between TTPs and IDPs pixel coordinates.

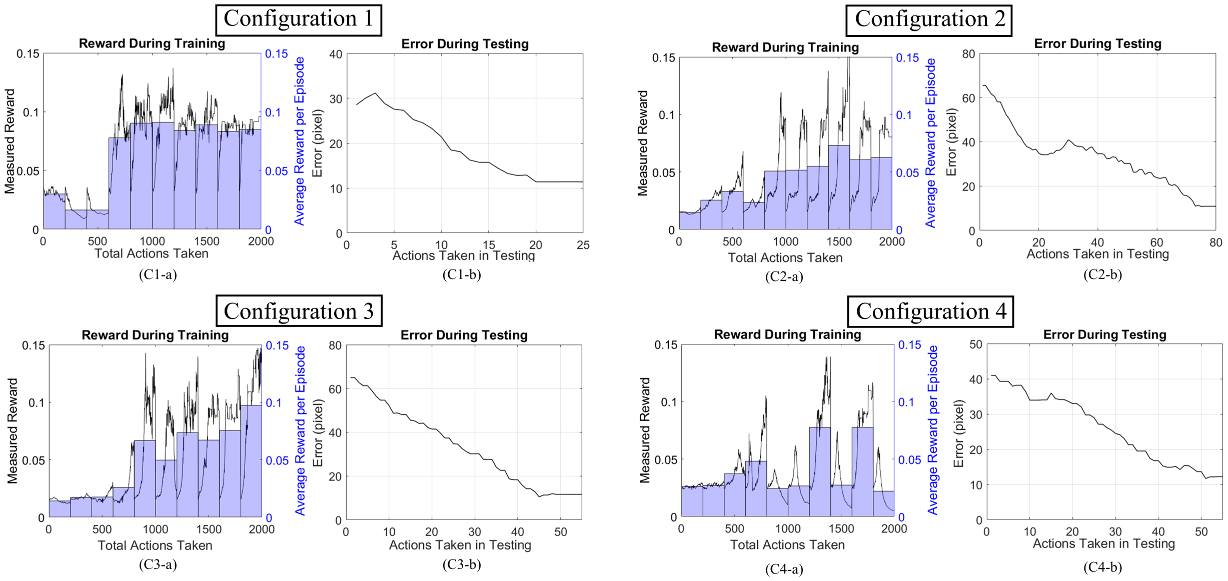

Figure 5.5: Reward during training and error during testing. (a) Rewards across all episodes of training for each configuration. The line plots indicate the reward per action while the bar plots display the average reward in each episode. (b) Euclidean error norm for single testing episodes for each configuration.

5.5 Results and Discussion

In each training set, $N_{episode} = 10$ episodes and $N_{action} = 200$ actions were used. Following the complete 2000 action training set, the trained policy was assessed with testing episodes using a greedy policy ($\epsilon = 0$) with $\alpha = 0$.

Fig. 5.4 displays four time instances from (a) *initialization* to (d) *task completion* of robotic tissue manipulation for the described four different simulation studies. In these studies, the goal is to indirectly manipulate Green TTPs via TGPs to reach black IDPs . The first three rows are associated with the CASE I and the last row is associated with CASE II.

Fig. 5.5 shows the defined performance evaluation metrics including the reward during the training episodes of each simulation study as well as the error which is the reciprocal of the reward during testing, as defined in (5.5). As can be observed in Fig. 5.5, the algorithm correctly learns a policy that increases reward (on average) as training progresses. Of note, the displayed rewards are associated with all actions during the training sets leading to the policies shown in Fig. 5.4. For each configuration, reward increases both within episodes and across episodes. Note that the high frequency variation in reward at high values is due to the action size causing individual actions to significantly effect reward.

For testing episodes, Fig. 5.5 plots the Euclidean error norm between TTPs and IDPs against the number of actions taken. While configuration 1 does not require many actions, the learned policy directs the TGPs to quickly move the TTPs to the IDPs . Configuration 2 and 3 represent more challenging tasks that requires significant strain on the simulated tissue. Despite the increased complexity of the dynamics with large deformation, successful policies are learned. Configuration 4 further increases the complexity of the task by changing the configuration of the camera. As can be seen in Fig. 5.4, instances C4-a through C4-d and Fig.5.5, instances C4-a through C4-b, the proposed algorithm was capable of learning weights that provide a successful policy. The converging errors in Fig. 5.5 instances C1-b through C4-b highlight the value of the defined feature in (5.7). This feature effectively serves as a completion criterion for the task by halting both graspers when the reward exceeds 0.08, which corresponds to a Euclidean error of 12.5 pixels, or roughly 8 pixel error for each TTP. This criterion can be modified as needed for a given surgical setup to reflect proper completion of the task. The four configurations shown represent very different initial configurations, yet the weight associated with the feature is able to be properly trained in each case, demonstrating the learning capabilities of the proposed SL algorithm.

There were a number of challenges for both developing and running the proposed SL algorithm:

Visual Occlusion: Due to the simulation environment including avatars of both surgical robot graspers, as well as the use of an opaque tissue phantom model, it is not uncommon for vision of one or both TTPs to become occluded. Proper selection of TGPs relative to TTPs in the camera frame can help to prevent the graspers or dragged tissue from obscuring the TTPs during exploitation with a good policy. However, during exploration, the random actions will cause the grasper to pass over nearly all nearby points including the TTPs. When this occurs, it was found necessary to halt the update of all weights until proper vision is restored via actions selected by the current ϵ-greedy policy. Additionally, if a grasper passes over a TTP, it is possible for the vision algorithm to incorrectly determine the center of the TTP, creating noise in the reward and features. The cyclical decreasing learning rate used in this work was found to assist in overcoming this noise.

Feature Selection: Feature selection is among the most challenging parts of feature-based Q-Learning as there is not a standard method for selecting features. Features must be selected based upon knowledge of the system and potentially subjective judgments for what equation should be optimized.

This work aimed to show that incorporation of simple features based on intuitive human knowledge was capable of solving the highly complicated task of simulated tissue manipulation with no camera calibration information with approximate Q-learning. The features chosen were selected to be the simplest and minimum number necessary to approach the task without knowledge of registration between camera, tissue, and robot. The developed algorithm can converge to a successful solution, indicating that the simulation environment, image processing, and Q-learning all are designed reasonably. As such, the authors consider this work to be a successful implementation of a computational framework on a previously undocumented Q-learning problem.

CHAPTER 6

A Method for Fast Localization of Tool Tip During Robot-Assisted Autonomous Cataract Surgery

The following chapter is adapted from the journal paper titled "A Novel Tissue Identification Framework in Cataract Surgery using an Integrated Bioimpedance-Based Probe and Machine Learning Algorithms" published in IEEE Transactions on Biomedical Engineering (TBME) and co-first authored with Sahba Aghajani Pedram [116].

6.1 Abstract

Objective: The objective of this work was to develop and experimentally validate a bioimpedance-based framework to identify tissues in contact with the surgical instrument during cataract surgery.

Methods: This work introduces an integrated hardware and software solution based on the unique bioimpedance of different intraocular tissues. The developed hardware can be readily integrated with commonly used surgical instruments. The proposed software framework, which encompasses data acquisition and a machine-learning classifier, is fast enough to be deployed in real-time surgical interventions. The experimental protocol included bioimpedance data collected from 31 *ex vivo* pig eyes targeting four intraocular tissues: *Iris*, *Cornea*, *Lens*, and *Vitreous*. *Results:* A classifier based on a support vector machine exhibited an overall accuracy of 91% across all trials. The algorithm provided substantial performance in detecting the intraocular tissues with 95% sensitivity and 100% reliability for the lens, along with 94%

sensitivity and 88% reliability for the vitreous. *Conclusion:* The developed impedance-based framework demonstrated successful intraocular tissue identification. *Significance:* Clinical implications include the ability to ensure safe operations by detecting posterior capsule rapture with 94% probability and improving surgical efficacy through lens detection with 100% reliability.

6.2 Introduction

A cataract is the progressive clouding of the lens of the eye which blocks light and, over time, can cause blindness. Worldwide, approximately one-third of cases of blindness and one-sixth of cases of vision impairment are the result of cataracts [117]. Cataract surgery is used to prevent cataract-induced blindness and is the most frequently performed surgical procedure in the United States, totaling about 3.6 million operations per year in 2015 [118]. Cataract surgery is a multiple-step process that involves extraction of the cloudy lens and implantation of an artificial lens implant. While technologies such as femtosecond laser systems have improved the safety of surgical steps such as corneal incision [119], capsulorhexis [120], and lens fragmentation [121], the most critical step, extraction of the lens, continues to be manually performed.

Manual extraction of the cataract is hindered by human hand tremor [122] and a limited ability to visually ascertain depth [123]. During intraocular procedures, the surgeon must rely on indirect visual cues such as cast shadows or color change to indicate instrument position relative to the surrounding anatomy (Fig. 6.1), but these cues are prone to misinterpretation and lack a direct measure of depth. As such, inadequate estimation of the instrument intraocular depth can lead to PC rupture, one of the most serious complications of cataract surgery [124]. To avoid the increased risk of PC rupture, many surgeons choose to skip thorough capsular polishing, which may lead to an increase in PC opacification [125], [126] and can result in hazy or reduced vision.

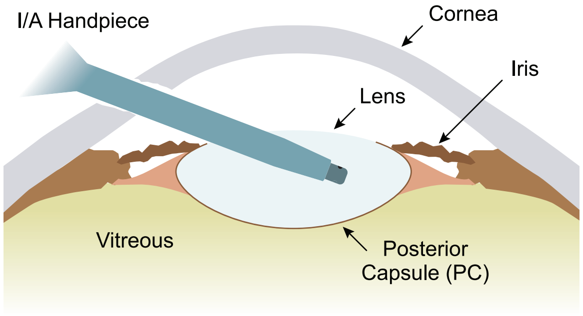

Figure 6.1: An illustrated eye during cataract surgery with relevant components labeled.

The accurate positioning requirements of cataract surgery are not prohibitive to a robotic system. For example, both the Preceyes Surgical System from Preceyes BV [127], [128] and the Mynutia, an intraocular robotic system from the Catholic University of Leuven, Belgium, have been used in teleoperation or collaboration mode to demonstrate intraocular surgical procedures in *in vivo* pig eyes [129] as well as in human patients [130]. In addition, the *Intraocular Robotic Interventional Surgical System* (IRISS) has been used to perform a range of intraocular surgical procedures via teleoperation, including complete lens extractions on *ex vivo* pig eyes [131], [132] as well as partially automated lens removal with vision feedback [133], [134].

Despite the success of robotic systems in performing intraocular procedures, these systems are hindered by a limited ability to ascertain the type of tissue in contact with the tool in real-time. For example, during the polishing step of cataract surgery, the *Irrigation/Aspiration* (I/A) handpiece must be brought in close contact with the PC and used under low aspiration force. However, the PC is approximately 4–9 µm thick [135], difficult to visualize, and is physically delicate. The rupture of the posterior capsule represents a major complication that requires immediate attention but can easily remain undetected without a means to directly detect the breakage.

Timely, accurate identification of what intraocular tissue the surgical instrument is in contact with could benefit the surgeon in several ways. For example, real-time detection of contact with the lens could inform a surgeon that it is safe to continue aspirating and may decrease surgical complications due to inadequate control of aspiration pressure. Similarly, many intraocular tissues a surgical instrument contacts over the course of cataract surgery are visually identical yet have vastly different surgical implications. For example, *Balance Salt Solution* (BSS), viscoelastic gel, and vitreous humor all appear as clear fluid through a surgical microscope. However, tool contact with BSS or viscoelastic gel is common and expected, whereas tool contact with vitreous would imply that the PC has been ruptured and immediate remedial actions must be taken. The ability to distinguish between these tissues in a timely and accurate manner would therefore assist the surgeon in making informed decisions.

In light of the dynamic, mobile nature of the eye and the intraocular anatomical structures during physical manipulations, real-time registration of the instrument with respect to the anatomy presents a significant challenge. To address this issue, systems such as the integrated scanning probe from Vanderbilt University [136] or the IRISS [133], [134] from the University of California, Los Angeles, have *Optical Coherence Tomography* (OCT) to simultaneously sense both the tool position as well as the surrounding anatomy during surgical procedures (Fig. 6.2). However, OCT-based methods of tool localization are prone to uncertainty due to the low signal-to-noise ratio of the captured data and can also be prohibitively slow due to the time requirement for the acquisition and processing of the OCT data. Furthermore, OCT suffers from the same inability of a surgical microscope in visually differentiating between BSS, viscoelastic gel, and vitreous humor as these materials appear optically similar.

An alternative method to know which tissue the surgical instrument is in contact with is to use the unique bioimpedance of each tissue. These methods have been explored for various clinical applications in the literature. For example, Lee et al. [137] used measurements of bioimpedance to differentiate between tumors and healthy tissue in the prostate. In another study [138], the authors developed a needle system to measure impedance variations of the kidney as a function of needle insertion depth and used this data to confirm successful

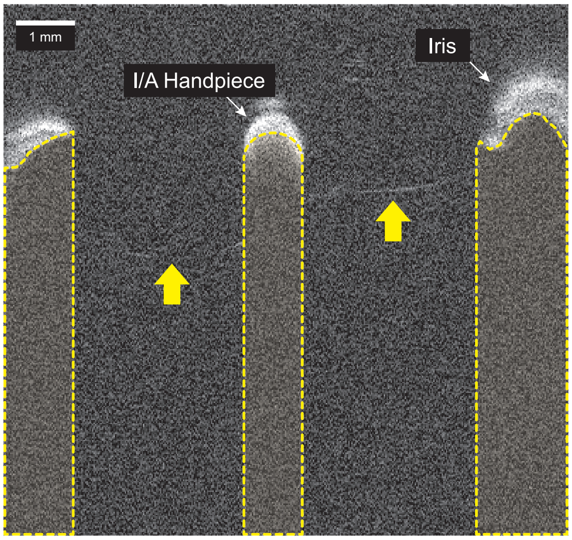

Figure 6.2: An OCT B-scan image acquired during a robot-guided PC polishing maneuver. The PC is faint and nearly indiscernible (yellow arrows). Yellow dotted regions represent occluded regions (the iris and I/A handpiece are opaque to the OCT laser) and therefore preclude the possibility of sensing beneath the tool or near the equator of the capsular bag, representing a serious safety concern for tool control.

percutaneous kidney access. Moreover, Cheng et al. [139] proposed a bioimpedance sensing method for a venipuncture procedure for the arm and used this system to differentiate various tissue types accessed during the insertion process. In [140], [141], the authors developed a bioelectrical impedance sensor and used a detection algorithm based on the collected tissue impedance data to prevent double puncturing of retinal vessels during retinal vein cannulation.

The overarching aim of this study was to explore the use of the bioimpedance attribute of various intraocular materials for fast tissue identification during cataract surgery. The study is motivated by the following reasons. First, it is known that different intraocular materials, such as cortical material and vitreous gel, exhibit dissimilar material properties which result in different electrical behaviour and response [142]–[144]. Second, the hardware required to measure bioimpedance could be designed to be incorporated into common cataract-surgery instrumentation (hand held or robotically manipulated). Third, processing of measured data can be fast and therefore the framework could be deployed in a real-time setting.

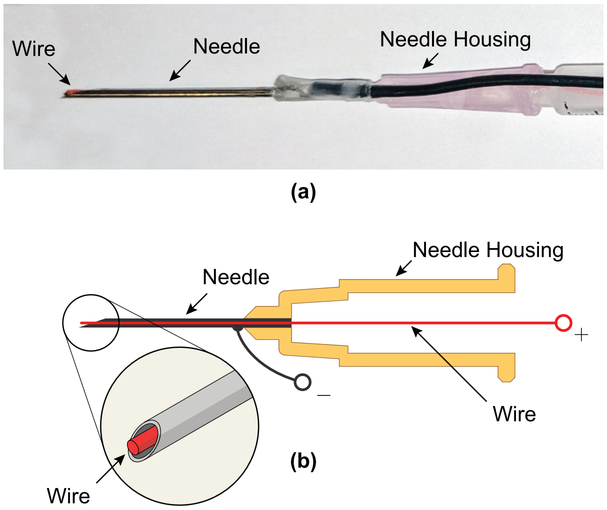

Figure 6.3: (a) Photograph showing the prototype probe integrated into a standard 18 Ga (1.2 mm) stainless-steel needle. (b) Cross-sectional schematic of prototype to highlight construction and geometry.

The outcomes of this study are a hardware and software sensing solution for measurement of bioimpedance property. The contributions to the literature are:

- The ability to differentiate between intraocular tissues during lens extraction that was experimentally validated in *ex vivo* pig eyes.
- A generalized hardware solution that can be integrated into common cataract-surgery instrumentation.

6.3 Method

6.3.1 Mechanical Design

Surgeons are accustomed to performing cataract surgery using specific surgical instruments and the current robotic systems, such as the IRISS, are designed to use the same commercially available suite of tools. Therefore, to ease adoption into both traditional manual cataract surgery and RAS, the design of a probe-based sensor must be well incorporated into existing instrumentation such that the external geometry of the tool is maintained. In this work, as a first step we demonstrate this using a prototype based on a needle (Fig. 6.3). However, the developed technology is designed in such a way that it can be integrated into tools for cataract surgery (such as a phacoemulsification or I/A handpiece) without changing how the tool is held or maneuvered by the surgeon within the eye.

To implement an impedance-based sensor, it was necessary to create a closed electrical circuit through the intraocular tissue to be identified. This required two connections: one for generating the input signal and a second to close the circuit. After initial experimentation with several designs, an integrated probe design was chosen.

The integrated probe design consists of both the connector that generates the input signal and the connector that closes the circuit mechanically integrated into the probe. The designed probe insulates the two connectors from each other except for a small ($\sim$ 1 mm) exposed section located at the tip of the probe. This insulation is used to constrain the electrical path measured by the probe to be between the conductors at the tool tip. Placement of the exposed portions of the conductors in close proximity suggests that the bioimpedance measured will be of the intraocular tissue at the tip of the probe. The mechanical construction of the sensor is not limited to any specific surgical instrument. As long as two conductors can be integrated into a surgical instrument, and insulated from each other except for a portion at the tip, the presented sensing method can be used. It should be noted that any conductive material, such as the metals that many commercially available surgical instruments are made of, can serve as one of the two required conductors. Therefore, the sensor can be embedded into any instrument with a metallic tip via the addition of a single wire as conceptually rendered in Fig. 6.4.

As a proof-of-concept, a standard 18 Ga (1.2 mm) stainless-steel needle fit onto a 1 mL syringe was used. The metal needle of the syringe was connected to one wire, while a second was inserted through the barrel of the syringe such that the end aligned with the needle tip as shown in Fig. 6.5b.

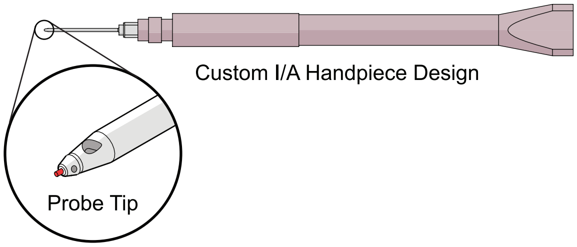

Figure 6.4: Illustration of touch probe design concept based on a sleeveless I/A handpiece. Note: this design was not implemented in this work, but is shown to illustrate the ease of integration of the developed technology into a commercially available tool.

6.3.2 Electrical Design

The working principle behind the electrical design of the sensor is a voltage divider circuit shown in Fig. 6.5a. The circuit consists of a single reference resistor, R_{ref}, in series with the probe. A voltage is generated across both the resistor and probe, and the voltage is measured across the probe. The voltage measured increases with impedance of the path between the conductors at the tool-tip according to Eq. 6.1.

$$V_{out} = V_{in} \frac{Z_{eye}}{R_{ref} + Z_{eye}} \tag{6.1}$$

where V_{out} is the measured voltage across the probe, V_{in} is the generated voltage, and Z_{eye} is the impedance of the path between the conductors at the tool tip. Differentiating Eq. 6.1 with respect to Z_{eye} results in:

$$\frac{dV_{out}}{dZ_{eye}} = V_{in} \frac{R_{ref}}{(R_{ref} + Z_{eye})^2} \tag{6.2}$$

For changes in the value of Z_{eye} to be reflected in large changes of V_{out}, it is desirable to maximize Eq. 6.2 with respect to R_{ref}. This constitutes a framework to select the best R_{ref} which maximizes the changes in the measured response (V_{out}) with respect to the changes in Z_{eye}. This is desirable as to gather dissimilar responses from different parts of the eye. This occurs when the $R_{ref} = \sqrt{Z_{eye} Z^*_{eye}}$, where Z^*_{eye} is the complex conjugate of Z_{eye}.

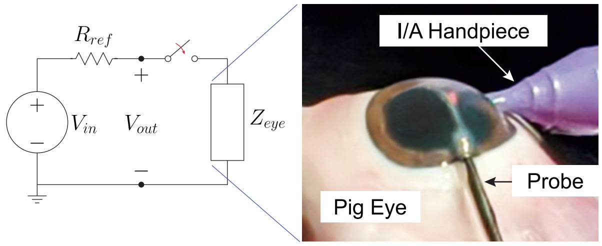

(a) **(b)**

Figure 6.5: (a) Electrical circuit diagram of the system. The switch (red arrow) indicates tissue contact. (b) Photograph of an experimental setup. The I/A handpiece provided constant irrigation and aspiration forces inside the eye while the probe was used to touch intraocular anatomy. The impedance Z_{eye} corresponds to physical anatomy within the eye.

However, Z_{eye} varies with frequency and the fluid or tissue constituting the path between the conductors at the tip of the surgical instrument. Because Z_{eye} was unknown, numerous values of R_{ref} between 100 Ω and 12 kΩ were tested in experiments on *ex vivo* pig eyes. Plots of V_{out} were visually examined for measurements of the various tissues and fluids of interest, and the value of R_{ref} was modified using a resistor box (allowing consecutive measurements for different resistances without movement of the probe). $R_{ref} = 2\ \text{k}\Omega$ was selected due to resulting in the largest overall variation in V_{out} for the tissues and fluids of interest.

6.3.3 Signal Generation

A myRIO-1900 (National Instruments) programmed in LabVIEW and LabVIEW FPGA is used for both signal generation and measurement (Fig. 6.6). Several input signals were trialed including DC, chirp, and step signals. Ultimately, it was found that a pseudorandom filtered Gaussian white noise signal resulted in the most distinguishable and consistent responses for the tissues and fluids of interest. A Gaussian white noise signal was generated between −5 VDC and 5 VDC at 1 kHz for 10k samples. This signal was then filtered through a fourth-order, low-pass filter with a cutoff frequency of 20 Hz to improve signal-to-noise ratio at the frequencies previously observed to best capture the system dynamics. The resulting signal was then stored and used as the input signal at V_{in} for all measurements (Fig. 6.7a).

A sample response from vitreous is displayed in Fig. 6.7b. The ability to differentiate the responses of the tested intraocular tissues was found to improve by using the same filtered signal for each measurement by reducing the influence of generation and measurement noise and making the input consistent between all trials.

6.3.4 Algorithm

6.3.4.1 Algorithm Selection

There are three main reasons motivating our choice to use *Machine Learning* (ML) algorithms. The first point that should be emphasized is that the underlying dynamic models of the different eye structures appear to be both non-linear and complex. This can be verified by examining the Bode plots (Section 6.5). Of particular note is the phase shift of different structures which are less than -22 degrees. This is in contrast to linear n^{th}-order systems with phase shifts in multiples of -90 degrees. Due to non-linearity of the system, simple signal processing algorithms cannot capture the complexity of the system's behavior. The second point is to qualitatively examine the data. Again, from the Bode plots, the lens structure (shown with green) is generally distinguishable (upper part of the Bode plot) but the other three are intertwined across all frequencies. This further confirms the complexity of the behaviour of different structures of the eye, and indicates that simple time domain/frequency domain system identifications are not capable of describing the problem. The third point is that the goal of this paper is not studying the eye tissue structures (dynamics) and how they behave, but rather to identify what tissue structure is in contact with the instrument, which is essentially a classification problem.

Based on these three points, (I) structures dynamics are nonlinear and complex, (II) qualitative analysis of the data, and (III) classification of structures is important rather than the actual structure dynamics, we decided to choose black-box (vs. white-box or gray-box) system identification (classification) approaches where no internal system's model is given/of

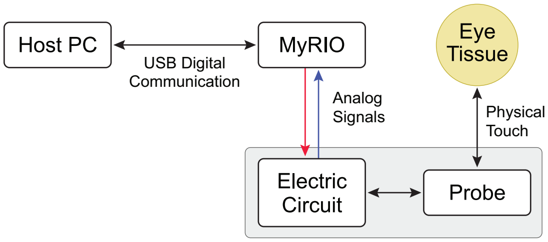

Figure 6.6: High-level diagram of the system setup. The host PC records data from a National Instruments MyRIO data acquisition device, which sends and receives analog signals to the electric circuit connected to the probe.

interest. A ML approach was selected because they are established black-box methods shown to be successful for various challenging classification problems. Also, due to the fact that there is no prior work in the literature for applying ML algorithms to our unique data set, several candidates needed to be tested to find the most appropriate one.

6.3.4.2 Supervised Machine Learning

As mentioned, the developed probe generates a pseudorandom voltage signal (V_{in}) to trigger all possible modes of the system and the output voltage across intraocular tissue (V_{out}) is recorded. Since the correspondence between each of the four intraocular tissue and the generated response (i.e., V_{out}) is known, supervised learning algorithms were used for classification purposes. More specifically, the recorded output voltage was used as an input of the algorithm and the corresponding intraocular tissue touched by the probe was used as its class label. A total of four classes (intraocular tissues) were considered in this study: (I) *Cornea*, (II) *Iris*, (III) *Lens*, and (IV) *Vitreous*. These classes are referred to as C, I, L, and V, respectively.

6.3.4.3 Features Selection

Generally, there are two approaches regarding the feature selections for ML algorithms. In one methodology (i.e. [145]), distinctive features of the input data are hand-picked by

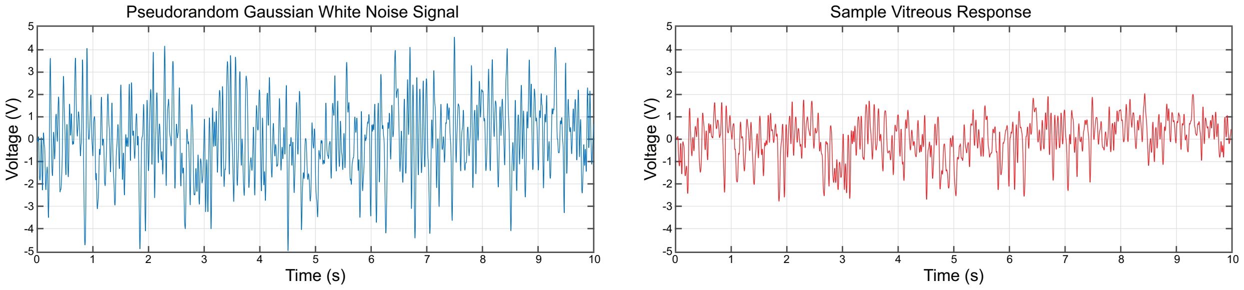

(a) (b)

Figure 6.7: An example of electrical signals for the probe in contact in vitreous: (a) pseudorandom input signal and (b) measured output signal.

engineers and then fed into the ML algorithm to boost learning, i.e. the dimensionality of the data and/or the number of labeled data required for training can be significantly reduced. One drawback of this method, however, is that it generally requires some domain knowledge/expertise of the problem being solved making it a challenging task. The other method for feature selection works based on the fact that if the right ML algorithm is chosen, the algorithm itself should be able to learn important features to be able to classify the input data [98], [146]–[148]. The drawback of this method is that for some applications, large amounts of data for training may be required which is both expensive and time-consuming. There is no one method that fits all problems but it is generally the premise of the ML algorithm to learn the patterns/features by itself [98]. We take the second approach and apply some of the commonly used classification algorithms to the collected raw data (i.e. the raw V_{out} signals are the input and the corresponding classes are the output). This independence from prior knowledge and human intervention in feature extraction is a major advantage.

6.3.4.4 Algorithms

The algorithms tested were *Decision Tree* (DT), *AdaBoosted Decision Tree* (ADT), *Random Forest* (RF), *Support Vector Machine* (SVM), a linear model with *Stochastic Gradient*

Descent (SGD), and *Convolutional Neural Net* (CNN) [149]. These algorithms were chosen as a general representation of classification algorithms commonly employed in the literature.

DTs are a non-parametric supervised learning method where the goal is to create a model that predicts the value of a target variable by learning simple decision rules inferred from the data features. The models are obtained by recursively partitioning the data space (represented as a decision tree) and fitting a simple prediction model within each partition. A tree is basically a piecewise constant function to fit the data. [150].

ADT [151], or Adaptive Boosting Decision Tree, is a meta-classifier which starts with a DT (as "weak" estimator) but improves its performance by fitting additional copies of the classifier on the same dataset. In this way, the weights of incorrectly classified instances are adjusted such that subsequent classifiers focus more on difficult cases, hence improving the performance.

RF [152] is a meta estimator that fits an ensemble of decision tree classifiers on various sub-samples of the dataset and uses averaging (or most popular votes of the trees) to improve the predictive accuracy and control over-fitting. Compared to ADTs, while the error rates of RFs are comparable, they are more robust with respect to noises.

SVM [153] is a ML algorithm that constructs a hyperplane or set of hyperplanes, in the original or transformed data space, for classification. The optimal classification is achieved by the hyperplane that has the largest distance to the nearest data point of any class. This is because, in general, the larger classification margin corresponds to the lower generalization error of the classifier.

Linear model (SGD) estimator implements regularized linear models with SGD learning scheme. The gradient of the loss is estimated at each sample (mini-batch of training data) and the model is updated with a decreasing learning rate to ensure proper convergence.

CNN is a ML algorithm that works based on the shared-weight architecture of the convolution kernels in the hidden layers for translation of invariance characteristics. As in Neural

Networks, the learning is done through a backward propagation scheme which makes it tractable for high-dimensional input data and networks with a large number of parameters while the evaluation/testing is performed through forward propagation [98].

6.3.4.5 Hyperparameters

Each of the algorithms selected has various hyperparameters that can be tuned for a given dataset. For each algorithm, we have picked three hyperparameters to optimize while the other hyperparameters are set to default. In the following, each of these hyperparameters are explained:

For DT, the maximum depth of the tree (depth_), the number of features to select when searching for the best split (max_features_), and the strategy deployed to split at each node (splitter_) are chosen.

Table 6.1: Hyperparameters for different ML algorithms.

Algorithm	Hyperparameters
DT	depth_ = {None, 1, 2, 3, 5, 10} max_ features_ = {None, “auto”, “sqrt”, “log2”} splitter_ = {“best”, “random”}
ADT	depth_ = {None, 1, 2, 3, 5, 10} n_estimators_ = {50, 100, 300, 500, 2000} learning_rate_ = {0.01, 0.1, 0.5, 1.0, 1.5}
RF	depth_ = {None, 1, 2, 3, 5, 10} n_estimators_ = {50, 100, 300, 500, 2000} max_features_ = {None, “auto”, “sqrt”, “log2”}
SVM	reg_ = {0.01, 0.1, 1, 10, 100, 1000} kernel_ = {‘linear’, ‘poly’, ‘rbf’, ‘sigmoid’} deg_ = {2, 3, 4, 5, 10}
SGD	loss_ = {‘log’, ‘mod_huber’, ‘squared_hinge’, ‘perceptron’} alpha_ = {0.0001, 0.001, 0.01, 0.1, 1.0} penalty_ = {‘l2’, ‘l1’, ‘elasticnet’}
CNN	n_hidden_layers_ = {1, 2 , 3, 4} n_filters_ = {3, 5, 7, 11} kernel_sizes_ = {3, 5, 7, 11}

For ADT, the maximum depth of the tree (depth_), the maximum number of estimators at which boosting is terminated (n_estimators_), and the learning rate parameter which shrinks the contribution of each classifier (learning_rate_) are selected.

For RF, the depth_, n_estimators_, and max_features_ explained above are chosen.

For SVM, the regularization parameter (reg_), the kernel function used in the algorithm (kernel_), and the degree of the polynomial kernel function ('poly') are picked.

For Linear Model (SGD), the loss function to be used (loss_), the weight of the regularization term (alpha_), and the penalty, or regularization term, to be used (penalty_) are selected.

For CNN, the number of hidden layers (n_hidden_layers_), number of convolutional filters (n_filters_), and convolution kernel sizes (kernel_sizes_) are chosen. The number of epochs is selected to be 400 and Adaptive Moment Estimation (Adam) optimizer [154] with learning rate of 0.001 is selected. To avoid overfitting the data, early stopping was used by means of using validation data during training.

Table 6.1 summarizes various values that were tested for hyperparameters of each ML algorithm.

6.4 Experiment

6.4.1 Experiment Setup and Procedure

For the experiments, *ex vivo* pig eyes (Sierra For Medical Science Inc., CA, USA) were used as the eye model. The unscalded eyes were removed from pigs slaughtered the previous day and shipped overnight on ice. Preparation of each eye for all experiments were performed under a surgical microscope (M840, Leica Microsystems, GmbH). For the corneal incisions, a clear corneal incision was created near the limbus using a 2.2 mm corneal knife (Alcon Laboratories Inc., Forth Worth, TX, USA) and the anterior chamber was filled with viscoelastic (Healon; Abbott Laboratories, Abbott Park, IL, USA).

To simulate intraocular dynamics similar to those that occur during cataract surgery, a straight-tip I/A handpiece with a side aspiration port (8172 UltraFLOW, Alcon Laboratories, Inc.) was inserted through a second corneal incision opposite to that of the first (Fig. 6.5b). The I/A handpiece was connected to an ACCURUS surgical system (Model 800CS, Alcon Laboratories, Inc.) to control the irrigation and aspirations pressures. Irrigation was held constant at approximately 30 mmHg and the aspiration pressure was manually varied with the foot pedal control between 0–50 mmHg. BSS (NDC 0065-0800-50, Alcon) was used as the irrigation fluid during the whole procedure.

For measuring each tissue, the probe was inserted through the corneal incision and placed in contact with the tissue of interest. Specifically, the probe's tip was placed in contact with the corneal endothelium, the iris stroma, and the crystalline lens. For the vitreous humor, the probe was used to intentionally rupture the PC and then held stationary within the vitreous. The response of the cornea, iris, lens, and vitreous humor were each measured three times, in the order listed, for each eye. The position of the probe tip was visually confirmed through the surgical microscope prior to each measurement and was held stationary and in contact with the intraocular tissue for the full duration of each measurement. Between measurements, the position of the probe tip was relocated to ensure contact with a different part of the same intraocular tissue.

The proposed solution was tested on a total of 31 *ex vivo* pig eyes over the course of five days, where each day involved multiple eyes and is referred to as an "experiment set". As three trials were performed for each of the four intraocular tissues of each eye, a total of ($31 \times 4 \times 3 = 372$) trials were conducted across all five experiment sets. The main reason to include multiple samples from each eye as well as having multiple eyes is to capture inter- and intra-subject variabilities with our classification algorithms. In each trial, the probe was placed in contact with an intraocular tissue, the pseudorandom voltage signal was used as the input (Fig. 6.7a), V_{in}, and the voltage across the tissue through the probe, V_{out}, was recorded. The transfer function of interest, $H(s)$, was defined as

$$H(s) = \frac{V_{out}(s)}{V_{in}(s)} \tag{6.3}$$

6.4.2 Performance Evaluation Metrics

There are three important criteria which were deployed to assess the performance of classification algorithms. These measures are *sensitivity*, *reliability*, and *accuracy*, denoted by C_s, C_r, and C_a, respectively. The mathematical formulations of these measures are as follow:

$$C_s = \frac{|y \cap \hat{y}|}{|y|} \tag{6.4a}$$

$$C_r = \frac{|y \cap \hat{y}|}{|\hat{y}|} \tag{6.4b}$$

$$C_a = \frac{2}{C_s^{-1} + C_r^{-1}} = \frac{2C_sC_r}{C_s + C_r} \tag{6.4c}$$

where $|\cdot|$ denotes the size of the set, y is the set of true labels, $\cap$ denotes intersection, and $\hat{y}$ is the set of predicted labels. Note that these concepts can be defined with respect to all class labels (called *overall* labels) or for each class pair (called *pairwise* labels). It can be seen that the overall sensitivity, reliability, and accuracy are equivalent. On the other hand, the pairwise sensitivity and reliability are generally different and can be expressed as:

$$C_s^{i,j} = \frac{|y_i \cap \hat{y}_j|}{|y_i|} \tag{6.5a}$$

$$C_r^{i,j} = \frac{|y_i \cap \hat{y}_j|}{|\hat{y}_j|} \tag{6.5b}$$

These two equations pertain to the true class label j being predicted as label i.

Based on these definitions, we consider three evaluation matrices to compare the classification algorithms. These matrices are *overall accuracy*, *pair-wise sensitivity*, and *pairwise*

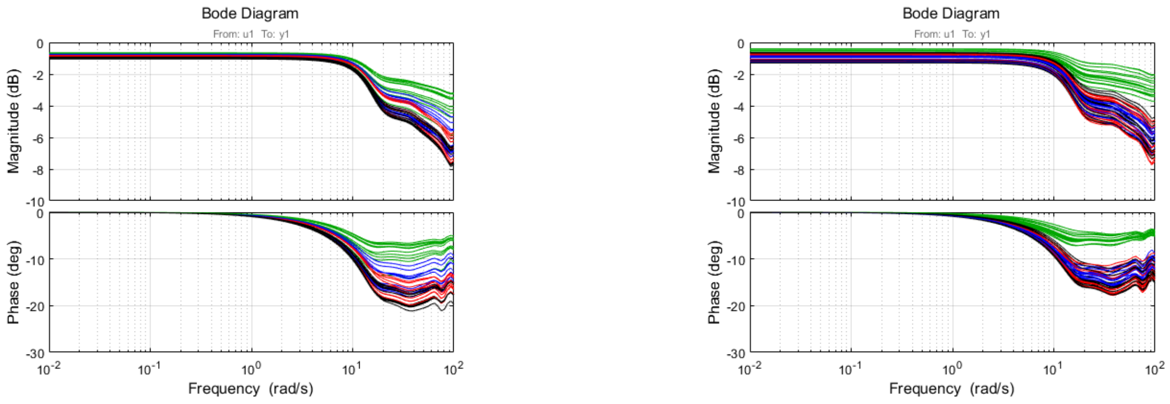

Experiment set I (4 eyes)   Experiment set II (5 eyes)

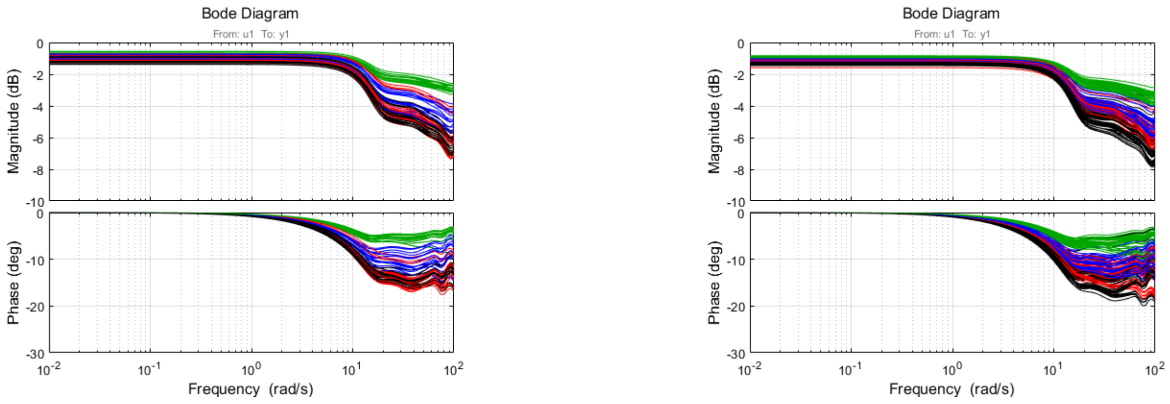

Experiment set III (6 eyes)   Experiment set IV (12 eyes)

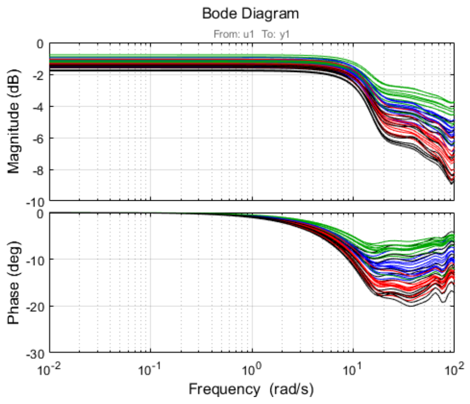

Experiment set V (4 eyes)

Figure 6.8: Bode plots of the collected bio-electrical responses across five different experiment sessions/days. The four relevant intraocular tissues examined were the iris (blue), cornea (red), lens (green), and vitreous (black).

reliability. These three measures provide different information about the performance of the algorithm and all are important from the clinical point of view. First, $C_s^{i,j}$ measures the probability of the algorithm to correctly label anatomical tissue when the probe is in contact with that tissue. Second, $C_r^{i,j}$ measures the probability in which the algorithm's estimation is correct. These two criteria are particularly important to a surgeon and could provide crucial safety measures while performing cataract surgery (see Section 6.6 for more detailed explanations). Third, the C_a criterion provides the overall accuracy information across all classes and therefore is an important measure to use for assessing the optimal detection/classification algorithm.

6.5 Results

The Bode plots of Eq. 6.3 for each experiment set are shown in Fig. 6.8. Each plot represents the superimposed Bode plots of all the trials performed in a particular experiment set. The parameters used for this analysis included a sampling time of $T_s = 1$ ms and frequency window of $[-2, 2]$ rad/s in log space which roughly corresponds to frequencies under 20 Hz. The main reason to represent the experiment data in the frequency domain was to gain better insights on whether different intraocular tissues were distinguishable in some domain. From Fig. 6.8, it can be seen that certain tissues (e.g., the lens) were very distinct in the frequency domain while other tissues might not be classifiable in this domain.

As the main purpose of the proposed framework was to identify the intraocular tissue in which the probe was in contact with, various classification algorithms were tested to accomplish this task. Because clear distinction between all the intraocular tissues was not observed in the data represented in the frequency domain (see Bode plots, Fig. 6.8), we decided to input the raw time-series experiment data into the classification algorithms. If there are distinctive features in the frequency or other domains, the machine learning algorithms should be able to learn [98]. As a result, the time-domain data should suit our purpose and was therefore chosen for the input of the classification algorithms.

As mentioned in Section 6.3.4, six ML algorithms were tested for classification of the gathered data. We used Python 3.7 to for the algorithm development purposes. To find the best classifier, we performed *within-class* and *between-class* searches in a brute force manner. The former was done to find the optimal hyper-parameters and the later was performed to finalize the optimal model parameters. First, a within-class optimization was done by performing a grid search over the hyper-parameters of each model (see Table 6.1 for the hyper-parameter values that were tested) and evaluated each model's performance using the overall accuracy, C_a in (6.4c). The evaluation process was iterated 100 times for each of the six models, with an early stopping criterion and data replacement. First, the data was randomly split into two training (80%) and testing (20%) sets. Note that the Bode plots (see Fig. 6.8) show that both the inter-subject and intra-subject variabilities are relatively small (i.e. responses can be seen as clusters with the same color), hence training/testing on the entire dataset, as opposed to methods with one or multiple subject leave-outs, would have very similar outcomes. At each iteration, the models with various hyper-parameters were trained on the training set using 5-fold cross-validation. The best-performing hyper-parameters for each model (based on the 5-fold cross-validation results) as well as the testing results were recorded. Once the iterations are done, the set of hyper-parameters that was most frequently selected was chosen as the optimal one for each classifier. Finally, a between-class optimization was performed to select the best classifier (with chosen hyper-parameters) based on the recorded testing results. The pairwise sensitivity, $C_s^{i,j}$, and pairwise reliability, $C_r^{i,j}$, of each algorithm are represented as confusion matrices in Fig. 6.9. Moreover, the overall accuracies, C_a, of all the models are reported in Table 6.2. As can be seen, SVM ($kernel\_ = rbf,\ reg\_ = 10$) performs the best in terms of the overall accuracy as well as the pair-wise sensitivity and reliability, hence was selected as the optimal model.

Pairwise Sensitivity:

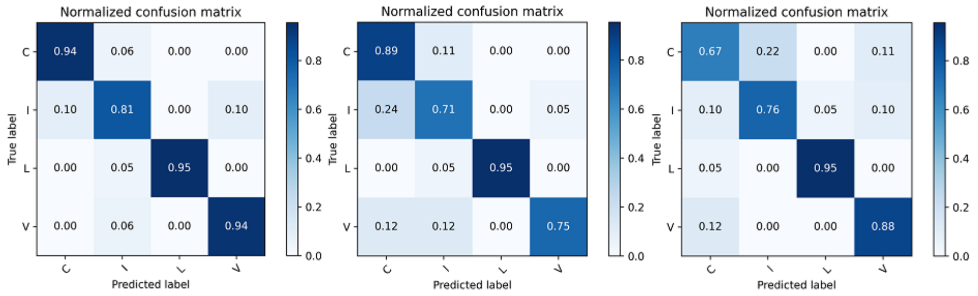

	C	I	L	V
C	0.94	0.06	0.00	0.00
I	0.10	0.81	0.00	0.10
L	0.00	0.05	0.95	0.00
V	0.00	0.06	0.00	0.94

	C	I	L	V
C	0.89	0.11	0.00	0.00
I	0.24	0.71	0.00	0.05
L	0.00	0.05	0.95	0.00
V	0.12	0.12	0.00	0.75

	C	I	L	V
C	0.67	0.22	0.00	0.11
I	0.10	0.76	0.05	0.10
L	0.05	0.00	0.95	0.00
V	0.12	0.00	0.00	0.88

SVM ADT CNN

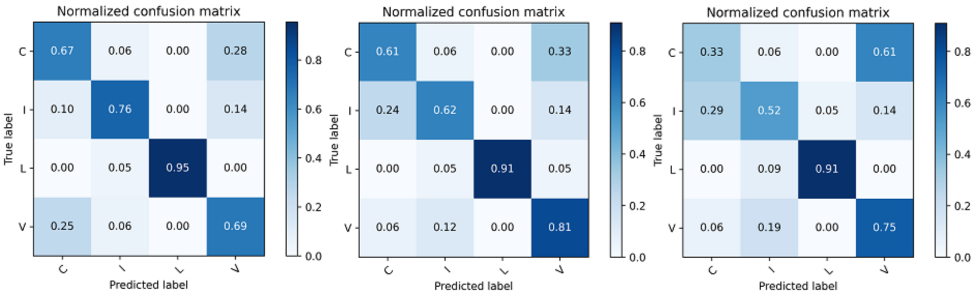

	C	I	L	V
C	0.67	0.06	0.00	0.28
I	0.10	0.76	0.00	0.14
L	0.00	0.05	0.95	0.00
V	0.25	0.06	0.00	0.69

	C	I	L	V
C	0.61	0.06	0.00	0.33
I	0.24	0.62	0.00	0.14
L	0.00	0.05	0.91	0.05
V	0.06	0.12	0.00	0.81

	C	I	L	V
C	0.33	0.06	0.00	0.61
I	0.29	0.52	0.05	0.14
L	0.00	0.09	0.91	0.00
V	0.06	0.19	0.00	0.75

DT RF SGD

Pairwise Reliability:

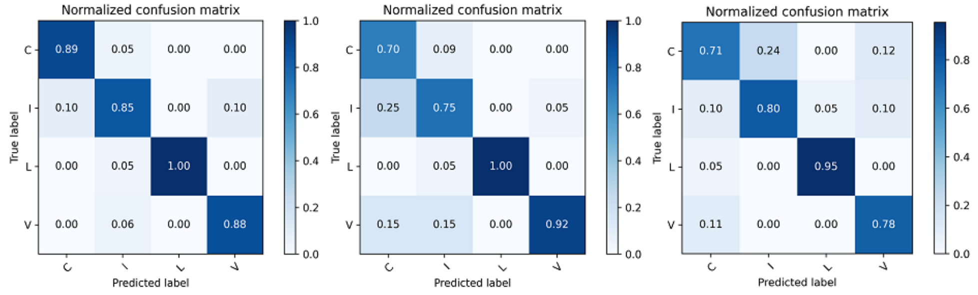

	C	I	L	V
C	0.89	0.05	0.00	0.00
I	0.10	0.85	0.00	0.10
L	0.00	0.05	1.00	0.00
V	0.00	0.06	0.00	0.88

	C	I	L	V
C	0.70	0.09	0.00	0.00
I	0.25	0.75	0.00	0.05
L	0.00	0.05	1.00	0.00
V	0.15	0.15	0.00	0.92

	C	I	L	V
C	0.71	0.24	0.00	0.12
I	0.10	0.80	0.05	0.10
L	0.05	0.00	0.95	0.00
V	0.11	0.00	0.00	0.78

SVM ADT CNN

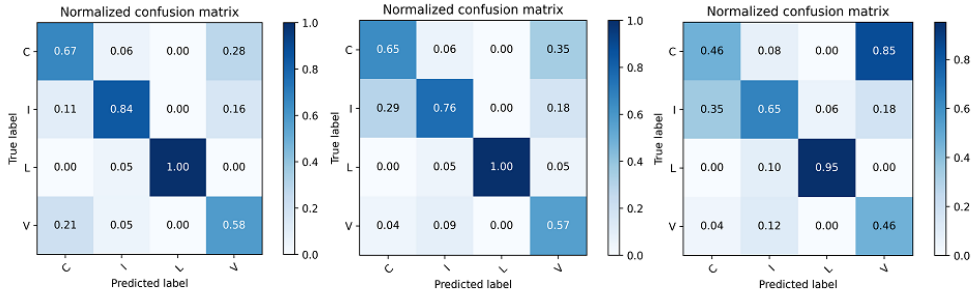

	C	I	L	V
C	0.67	0.06	0.00	0.28
I	0.11	0.84	0.00	0.16
L	0.00	0.05	1.00	0.00
V	0.21	0.05	0.00	0.58

	C	I	L	V
C	0.65	0.06	0.00	0.35
I	0.29	0.76	0.00	0.18
L	0.00	0.05	1.00	0.05
V	0.04	0.09	0.00	0.57

	C	I	L	V
C	0.46	0.08	0.00	0.85
I	0.35	0.65	0.06	0.18
L	0.00	0.10	0.95	0.00
V	0.04	0.12	0.00	0.46

DT RF SGD

Figure 6.9: Confusion matrices with pairwise sensitivity and reliability for SVM, ADT, CNN, DT, RF, and SGD. Labels are: Cornea (C), Iris (I), Lens (L), and Vitreous (V).

6.6 Discussion

An important aspect of the presented system is the simplicity of the mechanical design, and thus the ability for it to be adapted to many form factors. The requirements for integration of the system into any given tool is the ability to position two conductors such that they are insulated from each other except at the tool tip, and to route the two conductors to a data-acquisition system. A non-straight instrument shape does not prohibit the use of the developed system, and therefore it is applicable to the curved tools commonly employed in cataract surgery. Furthermore, instrument functionality is not expected to interfere with accuracy of the developed sensing method. Examples include ultrasonic vibration (from a phacoemulsification probe) or irrigation/aspiration fluid motion (from an I/A handpiece). The prototype probe demonstrated in this paper was installed in an 18 Ga (1.27 mm) syringe with length of 38 mm. However a variety of other surgical instruments could easily be adapted, such as an I/A handpiece (conceptually shown in Fig. 6.4), a phacoemulsification probe, an injector for intraocular lens implants, or curved syringes for viscoelastic injection.

The results of the overall accuracy of various classification algorithms are presented in Table 6.2. As can be seen, the SVM outperforms all of the other classification methods. A particular challenge for the classification task in our application was to gather a sufficiently large quantity of data because the experimentation was challenging and time-consuming. Each eye took approximately 30 minutes to complete from start of setup to final measurement, and required the full attention of a trained surgeon and two engineers. In our

Table 6.2: Performance of various classification algorithms.

Algorithm	Accuracy
SVM	0.91
ADT	0.84
CNN	0.81
DT	0.77
RF	0.74
SGD	0.63

experiments, the number of samples of each class (31 eyes × 3 trials = 93 samples) was much smaller than the number of dimensions of the input data (10,000) which is equal to the length of an individual signal. As a result, it was important to select an algorithm which could perform well for a smaller data set. This is one of the main reasons that SVM outperforms the other classifiers: this algorithm maintains its effectiveness even in cases where the number of dimensions is greater than the number of samples [98].

The sensitivity and reliability results of the six classification algorithms are shown in Fig. 6.9. Of note, the numbers in each cell are between 0 and 1; it is desirable to have larger values on the diagonal (ideally 1 shown with dark blue color in Fig. 6.9) and smaller values on the off diagonal (ideally 0 shown with light blue color in Fig. 6.9). Similar to the overall accuracy results, the SVM algorithm demonstrates strong performance in classifying each of the four classes (sensitivity ≥ 0.81, reliability ≥ 0.85). The algorithm's best performance is for the lens class (sensitivity = 0.95, reliability = 1.0) and its worst is for the iris class (sensitivity = 0.81, reliability = 0.85). From a surgical perspective, it is desirable for the lens to exhibit higher sensitivity and reliability than the iris. This is because the area of highest surgical risk is near the PC, especially when cortical material is still present and obscuring the PC. Therefore, the ability to distinguish lens is preferred over the ability to detect the iris as it has more important clinical benefits. These results confirm that using the proposed acquisition method combined with the SVM classifier is successful to estimate, with high sensitivity and reliability, the intraocular tissue in contact with the probe.

The sensitivity of the detection algorithm, $C_s^{i,j}$, measures the probability of the algorithm to correctly label intraocular tissue when the probe is in contact with it. This information can be useful to a surgeon while performing cataract surgery. For example, if the probe inadvertently punctures the PC, an algorithm which could detect with high probability the contact of the probe with vitreous ($C_s^{V,V}$) would be valuable in assisting the surgeon in knowing the PC has been ruptured. The selected SVM algorithm exhibits $C_s^{V,V} = 0.94$, meaning the there is a 94% chance that the suggested algorithm could detect PC rupture. Therefore, our proposed methodology could provide useful information during cataract surgery practice. On the other hand, the reliability of the detection algorithm, $C_r^{i,j}$, measures the probability that the algorithm's estimation is correct. This could also have important implications for surgeons. For example, during the lens extraction, a large value of $C_r^{L,L}$ would assure the surgeon that the probe is in contact with lens material and that it is safe to proceed. The selected SVM algorithm has $C_r^{L,L} = 1.00$, which means that as long as our framework predicts the tool is inside the lens, the extraction procedure is 100% safe to continue.

The experiments considered four intraocular tissues: cornea, iris, lens, and vitreous. Identification of each, independent from other anatomical structures, is useful in the sense that it provides confirmation on which anatomical structure the tool is currently in contact with. This information, whether a confirmation of existing information or an update of entirely new information, could assist the surgeon in making decisions to the benefit of the surgical outcomes. In addition to specific identification, many of the pairwise comparisons can also be useful and may even be the difference between a successful and a failed surgery.

For example, an important pairwise comparison is lens-to-vitreous, as the rupture of the PC leading to vitreous incarceration represents one of the major complications during cataract surgery and can easily remain undiagnosed when relying on only the surgical microscope. The detection of PC rupture after it occurs is valuable because it helps the surgeon quickly and properly address the complication. For example, early recognition of PC rupture can prevent expansion of the tear size, nucleus drop, and vitreous prolapse. Currently, surgeons must rely on a variety of indirect signs of PC rupture, which are transient in nature (and therefore require a few seconds to notice) or are purely visual (and therefore may be difficult to even detect). For these reasons, having a direct measurement of PC rupture, even if it comes after PC rupture, still has surgical benefit.

The developed system has potential application outside of cataract surgery, such as vitreoretinal procedures including pars plana vitrectomy (vitreous humor *cf.* retina), epiretinal membrane peeling (vitreous humor *cf.* membrane), and subretinal injection (neural retina *cf.*

retinal pigment epithelium). All of these procedures could benefit from timely and accurate identification of tissue in contact with the surgical instrument.

6.7 Conclusion

One difficulty for surgeons during cataract surgery is to know, with high confidence, which tissue the surgical instrument is in contact with. The common practice is to rely on visualization from the surgical microscope, but this provides limited depth perception and surgeons must rely on indirect visual cues such as shadows and color changes. Such methods render specific steps of cataract surgery challenging. For example, during PC polishing, in which the probe comes into close contact with the posterior capsule (thickness is 4–9 µm), limited depth perception can increase surgical risk. The use of OCT-based identification is another method to identify tissue, but this technology is still in its infancy and has slow data acquisition and processing, prohibiting its use in real-time applications. To address these challenges, we propose an integrated software and hardware detection solution. Such a framework could be easily integrated with the current cataract surgery setup, can be used for real-time applications, and is able to provide knowledge of the anatomy in contact with the tool tip with high sensitivity and reliability.

6.8 Acknowledgements

The authors would like to thank Andrea Govetto, MD; Anibal Andrés Francone, MD; Ismaël Chehaibou, MD; Moritz Pettenkofer, MD; and Mercedes Rodriguez, MD for their surgical expertise and assisting with the physical experiments. This work was supported in part by funds from the UCLA Stein Eye Institute; The Hess Foundation, New York, NY, USA; The Earl and Doris Peterson Fund, Los Angeles, CA, USA; an unrestricted institutional grant from Research to Prevent Blindness (RPB), NewYork, NY, USA; unrestricted gifts that support Professor Tsu-Chin Tsao's research program from various donors; the National Institutes of Health Grant No. R01-EY029689-01; and the Public Health Services Grant No. T32-EY7026-43.

CHAPTER 7

Conclusion

In summary, the research presented in this dissertation sought to advance the state of the art in how robotic technology can be applied to improving human health. The effort largely fell into three categories: 1) development of a novel hand exoskeleton for rehabilitation, 2) application of approximate Q-learning to the surgical subtask of tissue manipulation, and 3) demonstrating a proof-of-concept for using bioelectrical impedance sensing to identify contacted tissues in the eye during cataract surgery.

The largest research effort was the design and testing of the OTHER Hand exoskeleton. The OTHER Hand contains numerous novel design features, foremost among them the off-axis solution enabling thumb opposition. Designed to be integrated with upper limb exoskeletons such as the EXO-UL8 and BLUE SABINO, it addresses the challenge of high inertia and bulk at the hand via use of a bowden cable transmission allowing for remote placement of the motors. It uses a three-linkage, lateral base-to-distal topology with link lengths kinematically optimized to fit the wide range of hand sizes of the general public. Additionally, improve ease of use, particularly for those with impairments of the hand such as spasticity, it is designed with quick disconnect finger attachments that can be donned individually. Through testing with thirteen volunteers, both by subjective evaluation and objectively using the Anthropomorphic Hand Assessment Protocol, the design choices were validated. Users of all hand sizes were able to score exceptionally high on their ability to grasp and maintain a variety of household objects using a set of ten of the most common prehensile grasps and hand postures used in activities of daily living.

The second effort attempted to address the task of autonomous tissue manipulation using approximate Q-Learning. Using a set of seventeen simple features, it was demonstrated that the algorithm was capable of solving the task. Although other researchers and research efforts have previously addressed the task of automated tissue manipulation, the presented approach stands out in it's simplicity. However, the algorithm was only tested in simulation, and significant work would be needed to improve its speed and consistency before it could be applied with a physical robot.

The final goal of the research was the development of a method to improve the safety of cataract surgery. This was accomplished through the design and testing of a bioelectrical impedance-based probe, combined with machine learning classification algorithms. The presented hardware and software solution was tested *ex vivo* on 31 pig eyes to demonstrate classification of four ocular tissues: the cornea, iris, lens, and vitreous. A pseudorandom Gaussian white noise voltage signal was generated, channeled through the tissue between the ends of two conductors at the tip of a mock surgical tool, and resulting response recorded. The accuracy in classifying the tissues gives confidence that the solution could be practically applied with meaningful effects. The ability to alert a human or robot surgeon to contact with vitreous, iris, or cornea can serve as an alarm to prevent or minimize damage to the eye that would otherwise be challenging to detect. Meanwhile, detection of the lens can give the surgeon confidence that the tool is positioned appropriately and the surgery can proceed.

Bibliography

[1] P. W. Ferguson, Y. Shen, and J. Rosen, "Hand Exoskeleton Systems–Overview," in *Wearable Robotics: Systems and Applications*, J. Rosen and P. W. Ferguson, Eds., Academic Press, 2020, pp. 149–175. DOI: `10.1016/B978-0-12-814659-0.00008-4`.

[2] N. Hogan, H. I. Krebs, J. Charnnarong, P. Srikrishna, and A. Sharon, "MIT - MANUS : A Workstation for Manual Therapy and Training," in *Proceedings of the IEEE International Workshop on Robot and Human Communication*, 1992, pp. 161–165. DOI: `10.1109/ROMAN.1992.253895`.

[3] Y. Kawanishi, K. Oka, H. Tanaka, K. Okada, K. Sugamoto, and T. Murase, "In Vivo 3-Dimensional Kinematics of Thumb Carpometacarpal Joint During Thumb Opposition," *Journal of Hand Surgery*, vol. 43, no. 2, 182.e1–182.e7, 2018, ISSN: 15316564. DOI: `10.1016/j.jhsa.2017.07.028`. [Online]. Available: `https://doi.org/10.1016/j.jhsa.2017.07.028`.

[4] D. Giurintano, A. Hollister, W. Buford, D. Thompson, and L. Myers, "A virtual five-link model of the thumb," *Medical Engineering & Physics*, vol. 17, no. 4, pp. 297–303, 1995, ISSN: 1350-4533. DOI: `https://doi.org/10.1016/1350-4533(95)90855-6`. [Online]. Available: `https://www.sciencedirect.com/science/article/pii/1350453395908556`.

[5] F. J. Valero-Cuevas, M. E. Johanson, and J. D. Towles, "Towards a realistic biomechanical model of the thumb: The choice of kinematic description may be more critical than the solution method or the variability/uncertainty of musculoskeletal parameters," *Journal of Biomechanics*, vol. 36, no. 7, pp. 1019–1030, 2003. DOI: `10.1016/S0021-9290(03)00061-7`.

[6] A. Hollister, D. J. Giurintano, W. L. Buford, L. M. Myers, and A. Novick, "The axes of rotation of the thumb interphalangeal and metacarpophalangeal joints," *Clinical Orthopaedics and Related Research®*, vol. 320, pp. 188–193, 1995.

[7] Z.-M. Li and J. Tang, "Coordination of thumb joints during opposition," *Journal of biomechanics*, vol. 40, no. 3, pp. 502–510, 2007.

[8] P. Heo, G. M. Gu, S.-j. Lee, K. Rhee, and J. Kim, "Current hand exoskeleton technologies for rehabilitation and assistive engineering," *International Journal of Precision Engineering and Manufacturing*, vol. 13, no. 5, pp. 807–824, 2012.

[9] M. Sarac, M. Solazzi, and A. Frisoli, "Design requirements of generic hand exoskeletons and survey of hand exoskeletons for rehabilitation, assistive, or haptic use," *IEEE Transactions on Haptics*, vol. 12, no. 4, pp. 400–413, 2019.

[10] G. Zong, X. Pei, J. Yu, and S. Bi, "Classification and type synthesis of 1-dof remote center of motion mechanisms," *Mechanism and Machine Theory*, vol. 43, no. 12, pp. 1585–1595, 2008.

[11] J. Leijnse, P. Quesada, and C. Spoor, "Kinematic evaluation of the finger's interphalangeal joints coupling mechanism—variability, flexion–extension differences, triggers, locking swanneck deformities, anthropometric correlations," *Journal of Biomechanics*, vol. 43, no. 12, pp. 2381–2393, 2010.

[12] H. Vallery, J. Veneman, E. Van Asseldonk, R. Ekkelenkamp, M. Buss, and H. Van Der Kooij, "Compliant actuation of rehabilitation robots," *IEEE Robotics & Automation Magazine*, vol. 15, no. 3, pp. 60–69, 2008.

[13] D. Rus and M. T. Tolley, "Design, fabrication and control of soft robots," *Nature*, vol. 521, no. 7553, pp. 467–475, 2015.

[14] K. R. Mills, "The basics of electromyography," *Journal of Neurology, Neurosurgery & Psychiatry*, vol. 76, no. suppl 2, pp. ii32–ii35, 2005.

[15] J. R. Millan, F. Renkens, J. Mourino, and W. Gerstner, "Noninvasive brain-actuated control of a mobile robot by human eeg," *IEEE Transactions on Biomedical Engineering*, vol. 51, no. 6, pp. 1026–1033, 2004.

[16] C. J. Bell, P. Shenoy, R. Chalodhorn, and R. P. Rao, “Control of a humanoid robot by a noninvasive brain–computer interface in humans,” *Journal of Neural Engineering*, vol. 5, no. 2, p. 214, 2008.

[17] S. W. O’Driscoll and N. J. Giori, “Continuous passive motion (cpm): Theory and principles of clinical application,” *Journal of Rehabilitation Research and Development*, vol. 37, no. 2, pp. 179–188, 2000.

[18] B. T. Volpe, M. Ferraro, D. Lynch, *et al.*, “Robotics and other devices in the treatment of patients recovering from stroke,” *Current Atherosclerosis Reports*, vol. 6, no. 4, pp. 314–319, 2004.

[19] P. S. Lum, C. G. Burgar, M. Van der Loos, P. C. Shor, M. Majmundar, and R. Yap, “The mime robotic system for upper-limb neuro-rehabilitation: Results from a clinical trial in subacute stroke,” in *9th International Conference on Rehabilitation Robotics (ICORR)*, IEEE, 2005, pp. 511–514.

[20] C. G. Burgar, P. S. Lum, A. Scremin, *et al.*, “Robot-assisted upper-limb therapy in acute rehabilitation setting following stroke: Department of veterans affairs multisite clinical trial,” *J Rehabil Res Dev*, vol. 48, no. 4, pp. 445–458, 2011.

[21] H. Kim, L. M. Miller, I. Fedulow, *et al.*, “Kinematic data analysis for post-stroke patients following bilateral versus unilateral rehabilitation with an upper limb wearable robotic system,” *IEEE Transactions on Neural Systems and Rehabilitation Engineering*, vol. 21, no. 2, pp. 153–164, 2012.

[22] L. Lucas, M. DiCicco, and Y. Matsuoka, “An emg-controlled hand exoskeleton for natural pinching,” *Journal of Robotics and Mechatronics*, vol. 16, pp. 482–488, 2004.

[23] M. Mulas, M. Folgheraiter, and G. Gini, “An emg-controlled exoskeleton for hand rehabilitation,” in *9th International Conference on Rehabilitation Robotics, 2005 (ICORR 2005).*, IEEE, 2005, pp. 371–374.

[24] E. B. Brokaw, I. Black, R. J. Holley, and P. S. Lum, “Hand spring operated movement enhancer (handsome): A portable, passive hand exoskeleton for stroke rehabilitation,” *IEEE Transactions on Neural Systems and Rehabilitation Engineering*, vol. 19, no. 4, pp. 391–399, 2011.

[25] L. Dovat, O. Lambercy, R. Gassert, *et al.*, “Handcare: A cable-actuated rehabilitation system to train hand function after stroke,” *IEEE Transactions on Neural Systems and Rehabilitation Engineering*, vol. 16, no. 6, pp. 582–591, 2008.

[26] T. Nef, M. Mihelj, G. Kiefer, C. Perndl, R. Muller, and R. Riener, “Armin-exoskeleton for arm therapy in stroke patients,” in *2007 IEEE 10th International Conference on Rehabilitation Robotics*, IEEE, 2007, pp. 68–74.

[27] M. Simkins, I. Fedulow, H. Kim, G. Abrams, N. Byl, and J. Rosen, “Robotic rehabilitation game design for chronic stroke,” *Games For Health: Research, Development, and Clinical Applications*, vol. 1, no. 6, pp. 422–430, 2012.

[28] M. Simkins, J. R. Roldan, H. Kim, G. Abrams, N. Byl, and J. Rosen, “Kinematic analysis of virtual reality task intensity induced by a rehabilitation robotic system in stroke patients,” in *ASME 2013 Dynamic Systems and Control Conference*, American Society of Mechanical Engineers Digital Collection, 2013.

[29] Y. Ren, H.-S. Park, and L.-Q. Zhang, “Developing a whole-arm exoskeleton robot with hand opening and closing mechanism for upper limb stroke rehabilitation,” in *2009 IEEE International Conference on Rehabilitation Robotics*, IEEE, 2009, pp. 761–765.

[30] P. W. Ferguson*, B. Dimapasoc*, Y. Shen, and J. Rosen, “Design of a Hand Exoskeleton for Use with Upper Limb Exoskeletons,” in *4th International Symposium on Wearable Robotics (WeRob)*, Springer, 2018, pp. 276–280. DOI: `10.1007/978-3-030-01887-0_53`.

[31] E. J. Benjamin, M. J. Blaha, S. E. Chiuve, *et al.*, “Heart disease and stroke statistics—2017 update: A report from the american heart association,” *Circulation*, vol. 135, no. 10, e146–e603, 2017, ISSN: 0009-7322. DOI: `10.1161/CIR.0000000000000485`.

[32] A. Wege and A. Zimmermann, “Electromyography sensor based control for a hand exoskeleton,” in *2007 IEEE Int. Conf. on Robotics and Biomimetics (ROBIO)*, Dec. 2007, pp. 1470–1475. DOI: `10.1109/ROBIO.2007.4522381`.

[33] N. S. K. Ho, K. Y. Tong, X. L. Hu, *et al.*, “An emg-driven exoskeleton hand robotic training device on chronic stroke subjects: Task training system for stroke rehabilitation,” in *2011 IEEE International Conference on Rehabilitation Robotics*, Jun. 2011, pp. 1–5. DOI: `10.1109/ICORR.2011.5975340`.

[34] C. N. Schabowsky, S. B. Godfrey, R. J. Holley, and P. S. Lum, “Development and pilot testing of HEXORR: Hand EXOskeleton Rehabilitation Robot,” *Journal of NeuroEngineering and Rehabilitation*, vol. 7, no. 1, p. 36, Jul. 2010, ISSN: 1743-0003. DOI: `10.1186/1743-0003-7-36`.

[35] A. Frisoli, F. Rocchi, S. Marcheschi, A. Dettori, F. Salsedo, and M. Bergamasco, “A new force-feedback arm exoskeleton for haptic interaction in virtual environments,” in *First Joint Eurohaptics Conference and Symposium on Haptic Interfaces for Virtual Environment and Teleoperator Systems. World Haptics Conference*, 2005, pp. 195–201. DOI: `10.1109/WHC.2005.15`.

[36] C. Lauretti, F. Cordella, A. L. Ciancio, *et al.*, “Learning by demonstration for motion planning of upper-limb exoskeletons,” *Frontiers in Neurorobotics*, vol. 12, p. 5, 2018, ISSN: 1662-5218. DOI: `10.3389/fnbot.2018.00005`.

[37] Y. Shen, J. Ma, B. Dobkin, and J. Rosen, “Asymmetric dual arm approach for post stroke recovery of motor function utilizing the exo-ul8 exoskeleton system: A pilot study,” in *Engineering in Medicine and Biology Society (EMBC)*, Jun. 2018.

[38] J. C. Perry, R. Maura, C. K. Bitikofer, and E. T. Wolbrecht, “Blue sabino: Development of a bilateral exoskeleton instrument for comprehensive upper-extremity neuromuscular assessment,” in *2018 Int. Conf. on Neurorehabilitation (ICNR)*, Oct. 2018.

[39] I. Kapandji, L. Honoré, and F. Poilleux, *Upper Limb*, ser. Physiology of the joints : Annotated diagrams of the mechanics of the human joints / I.A. Kapandji. L.H. Honoré Übers. Churchill Livingstone, 1982, ISBN: 9780443025044.

[40] T. Feix, J. Romero, H. Schmiedmayer, A. M. Dollar, and D. Kragic, “The grasp taxonomy of human grasp types,” *IEEE Transactions on Human-Machine Systems*, vol. 46, no. 1, pp. 66–77, 2016.

[41] J. Z. Zheng, S. De La Rosa, and A. M. Dollar, “An investigation of grasp type and frequency in daily household and machine shop tasks,” in *2011 IEEE International Conference on Robotics and Automation*, IEEE, 2011, pp. 4169–4175.

[42] M. Tonkin, “Thumb opposition: Its definition and my approach to its measurement,” *Journal of Hand Surgery (European Volume)*, vol. 45, no. 3, pp. 315–317, 2020, PMID: 31793377. DOI: `10.1177/1753193419889504`. eprint: `https://doi.org/10.1177/1753193419889504`. [Online]. Available: `https://doi.org/10.1177/1753193419889504`.

[43] S. F. Duncan, C. E. Saracevic, and R. Kakinoki, “Biomechanics of the hand,” *Hand clinics*, vol. 29, no. 4, pp. 483–492, 2013.

[44] L. Y. Chang and Y. Matsuoka, “A kinematic thumb model for the act hand,” in *Proceedings 2006 IEEE International Conference on Robotics and Automation, 2006. ICRA 2006.*, IEEE, 2006, pp. 1000–1005.

[45] B. Alexander and K. Viktor, “Proportions of hand segments,” *International Journal of Morphology*, vol. 28, no. 3, pp. 755–758, 2010.

[46] A. I. Kapandji, “Clinical evaluation of the thumb’s opposition,” *Journal of Hand Therapy*, vol. 5, no. 2, pp. 102–106, 1992.

[47] Y. Kadowaki, T. Noritsugu, M. Takaiwa, D. Sasaki, and M. Kato, “Development of soft power-assist glove and control based on human intent,” *Journal of Robotics and Mechatronics*, vol. 23, no. 2, pp. 281–291, 2011.

[48] P. Polygerinos, Z. Wang, K. C. Galloway, R. J. Wood, and C. J. Walsh, “Soft robotic glove for combined assistance and at-home rehabilitation,” *Robotics and Autonomous Systems*, vol. 73, pp. 135–143, 2015.

[49] P. Maeder-York, T. Clites, E. Boggs, *et al.*, “Biologically Inspired Soft Robot for Thumb Rehabilitation,” *Journal of Medical Devices*, vol. 8, no. 2, Apr. 2014, 020933, ISSN: 1932-6181. DOI: `10.1115/1.4027031`.

[50] M. Cempini, M. Cortese, and N. Vitiello, “A powered finger–thumb wearable hand exoskeleton with self-aligning joint axes,” *IEEE/ASME Transactions on Mechatronics*, vol. 20, no. 2, pp. 705–716, 2014.

[51] A. Wege and G. Hommel, “Development and control of a hand exoskeleton for rehabilitation of hand injuries,” in *2005 IEEE/RSJ International Conference on Intelligent Robots and Systems*, IEEE, 2005, pp. 3046–3051.

[52] H. Kawasaki, S. Ito, Y. Ishigure, *et al.*, “Development of a hand motion assist robot for rehabilitation therapy by patient self-motion control,” in *2007 IEEE 10th International Conference on Rehabilitation Robotics*, IEEE, 2007, pp. 234–240.

[53] F. Wang, M. Shastri, C. L. Jones, *et al.*, “Design and control of an actuated thumb exoskeleton for hand rehabilitation following stroke,” in *2011 IEEE International Conference on Robotics and Automation*, IEEE, 2011, pp. 3688–3693.

[54] P. M. Aubin, H. Sallum, C. Walsh, L. Stirling, and A. Correia, “A pediatric robotic thumb exoskeleton for at-home rehabilitation: The isolated orthosis for thumb actua-

tion (iota)," in *2013 IEEE 13th International Conference on Rehabilitation Robotics (ICORR)*, IEEE, 2013, pp. 1–6.

[55] P. Agarwal, Y. Yun, J. Fox, K. Madden, and A. D. Deshpande, "Design, control, and testing of a thumb exoskeleton with series elastic actuation," *The International Journal of Robotics Research*, vol. 36, no. 3, pp. 355–375, 2017.

[56] K. Tadano, M. Akai, K. Kadota, and K. Kawashima, "Development of grip amplified glove using bi-articular mechanism with pneumatic artificial rubber muscle," in *2010 IEEE International Conference on Robotics and Automation*, IEEE, 2010, pp. 2363–2368.

[57] M. Fontana, A. Dettori, F. Salsedo, and M. Bergamasco, "Mechanical design of a novel hand exoskeleton for accurate force displaying," in *2009 IEEE International Conference on Robotics and Automation*, IEEE, 2009, pp. 1704–1709.

[58] A. Chiri, N. Vitiello, F. Giovacchini, S. Roccella, F. Vecchi, and M. C. Carrozza, "Mechatronic design and characterization of the index finger module of a hand exoskeleton for post-stroke rehabilitation," *IEEE/ASME Transactions on Mechatronics*, vol. 17, no. 5, pp. 884–894, 2011.

[59] J. Ryu, W. P. Cooney, L. J. Askew, K.-N. An, and E. Y. Chao, "Functional ranges of motion of the wrist joint," *The Journal of Hand Surgery*, vol. 16, no. 3, pp. 409–419, 1991, ISSN: 0363-5023. DOI: `https://doi.org/10.1016/0363-5023(91)90006-W`. [Online]. Available: `https://www.sciencedirect.com/science/article/pii/036350239190006W`.

[60] D. C. Boone and S. P. Azen, "Normal range of motion of joints in male subjects.," *The Journal of Bone and Joint Surgery*, vol. 61, no. 5, pp. 756–759, 1979.

[61] N. Secciani, M. Bianchi, A. Ridolfi, *et al.*, "Tailor-made hand exoskeletons at the university of florence: From kinematics to mechatronic design," *Machines*, vol. 7, no. 2, p. 22, 2019.

[62] M. Fontana, S. Fabio, S. Marcheschi, and M. Bergamasco, “Haptic Hand Exoskeleton for Precision Grasp Simulation,” *Journal of Mechanisms and Robotics*, vol. 5, no. 4, Oct. 2013, 041014, ISSN: 1942-4302. DOI: `10.1115/1.4024981`. [Online]. Available: `https://doi.org/10.1115/1.4024981`.

[63] P. Stergiopoulos, P. Fuchs, and C. Laurgeau, “Design of a 2-finger hand exoskeleton for vr grasping simulation,” *Eurohaptics, Dublin, Ireland*, pp. 80–93, 2003.

[64] P. W. Ferguson, B. Dimapasoc, and J. Rosen, “Optimal Kinematic Design of the Link Lengths of a Hand Exoskeleton,” in *Wearable Robotics: Systems and Applications*, J. Rosen and P. W. Ferguson, Eds., Academic Press, 2020, pp. 193–206. DOI: `10.1016/B978-0-12-814659-0.00010-2`.

[65] M. C. Hume, H. Gellman, H. McKellop, and R. H. Brumfield, “Functional range of motion of the joints of the hand,” *Journal of Hand Surgery*, vol. 15, no. 2, pp. 240–243, 1990.

[66] J. P. Merlet, “Jacobian, Manipulability, Condition Number, and Accuracy of Parallel Robots,” *Journal of Mechanical Design*, vol. 128, no. 1, pp. 199–206, Jun. 2005, ISSN: 1050-0472. DOI: `10.1115/1.2121740`. [Online]. Available: `https://doi.org/10.1115/1.2121740`.

[67] P. P. Urban, T. Wolf, M. Uebele, *et al.*, “Occurence and clinical predictors of spasticity after ischemic stroke,” *Stroke*, vol. 41, no. 9, pp. 2016–2020, 2010.

[68] R. Yokogawa and K. Hara, “Measurement of Distribution of Maximum Index-Fingertip Force in all Directions at Fingertip in Flexion/Extension Plane,” *Journal of Biomechanical Engineering*, vol. 124, no. 3, pp. 302–307, May 2002, ISSN: 0148-0731. DOI: `10.1115/1.1468637`. eprint: `https://asmedigitalcollection.asme.org/biomechanical/article-pdf/124/3/302/5533572/302\_1.pdf`. [Online]. Available: `https://doi.org/10.1115/1.1468637`.

[69] A. A. Timmermans, H. A. Seelen, R. D. Willmann, and H. Kingma, "Technology-assisted training of arm-hand skills in stroke: Concepts on reacquisition of motor control and therapist guidelines for rehabilitation technology design," *Journal of Neuroengineering and Rehabilitation*, vol. 6, no. 1, p. 1, 2009.

[70] *Dexo: Dual force-feedback arm and hand exoskeletons.* [Online]. Available: `https://www.spaceapplications.com/wp-content/uploads/2018/05/8-product-sheet-dexo-1.pdf` (visited on 07/08/2020).

[71] M.-A. Choukou, S. Mbabaali, J. Bani Hani, and C. Cooke, "Haptic-enabled hand rehabilitation in stroke patients: A scoping review," *Applied Sciences*, vol. 11, no. 8, 2021, ISSN: 2076-3417. DOI: `10.3390/app11083712`. [Online]. Available: `https://www.mdpi.com/2076-3417/11/8/3712`.

[72] M. Cutkosky, "On grasp choice, grasp models, and the design of hands for manufacturing tasks," *IEEE Transactions on Robotics and Automation*, vol. 5, no. 3, pp. 269–279, Jun. 1989, ISSN: 2374-958X. DOI: `10.1109/70.34763`.

[73] N. Yozbatiran, L. Der-Yeghiaian, and S. C. Cramer, "A standardized approach to performing the action research arm test," *Neurorehabilitation and Neural Repair*, vol. 22, no. 1, pp. 78–90, 2008. DOI: `10.1177/1545968307305353`. eprint: `https://doi.org/10.1177/1545968307305353`. [Online]. Available: `https://doi.org/10.1177/1545968307305353`.

[74] C. M. Light, P. H. Chappell, and P. J. Kyberd, "Establishing a standardized clinical assessment tool of pathologic and prosthetic hand function: Normative data, reliability, and validity," *Archives of Physical Medicine and Rehabilitation*, vol. 83, no. 6, pp. 776–783, 2002, ISSN: 0003-9993. DOI: `https://doi.org/10.1053/apmr.2002.32737`. [Online]. Available: `https://www.sciencedirect.com/science/article/pii/S0003999302095795`.

[75] I. Llop-Harillo, A. Pérez-González, J. Starke, and T. Asfour, "The anthropomorphic hand assessment protocol (ahap)," *Robotics and Autonomous Systems*, vol. 121, p. 103 259, 2019, ISSN: 0921-8890. DOI: `10.1016/j.robot.2019.103259`.

[76] B. Calli, A. Walsman, A. Singh, S. Srinivasa, P. Abbeel, and A. M. Dollar, "Benchmarking in manipulation research: Using the yale-cmu-berkeley object and model set," *IEEE Robotics Automation Magazine*, vol. 22, no. 3, pp. 36–52, Sep. 2015, ISSN: 1558-223X. DOI: `10.1109/MRA.2015.2448951`.

[77] I. Llop-Harillo, A. Pérez-González, and J. Andrés-Esperanza, "Grasping ability and motion synergies in affordable tendon-driven prosthetic hands controlled by able-bodied subjects," *Frontiers in Neurorobotics*, vol. 14, 2020, ISSN: 1662-5218. DOI: `10.3389/fnbot.2020.00057`. [Online]. Available: `https://www.frontiersin.org/article/10.3389/fnbot.2020.00057`.

[78] L. Timm, "Design and development of an open-source adl-compliant prosthetic arm for transradial amputees," M.S. thesis, Faculty of Health Sciences, 2021.

[79] M. A. Bardien and S. Sivarasu, "The Self Actuated Tenim Hand: The Conversion of a Body-Driven Prosthesis to an Electromechanically Actuated Device," ser. Frontiers in Biomedical Devices, vol. 2021 Design of Medical Devices Conference, Apr. 2021. DOI: `10.1115/DMD2021-1086`. eprint: `https://asmedigitalcollection.asme.org/BIOMED/proceedings-pdf/DMD2021/84812/V001T12A013/6805493/v001t12a013-dmd2021-1086.pdf`. [Online]. Available: `https://doi.org/10.1115/DMD2021-1086`.

[80] H. G. Malabet, R. A. Robles, and K. B. Reed, "Symmetric motions for bimanual rehabilitation," in *2010 IEEE/RSJ International Conference on Intelligent Robots and Systems*, 2010, pp. 5133–5138.

[81] S. A. Pedram*, P. W. Ferguson*, C. Shin, *et al.*, "Toward Synergic Learning for Autonomous Manipulation of Deformable Tissues via Surgical Robots: An Approximate Q-Learning Approach," in *8th International Conference on Biomedical Robotics and*

Biomechatronics (BioRob), 2020, pp. 878–884. DOI: `10.1109/BioRob49111.2020.9224421`.

[82] A. Kapoor, M. Li, and R. H. Taylor, "Spatial motion constraints for robot assisted suturing using virtual fixtures," in *International Conference on Medical Image Computing and Computer-Assisted Intervention*, Springer, 2005, pp. 89–96.

[83] S. A. Pedram, P. Ferguson, J. Ma, E. Dutson, and J. Rosen, "Autonomous suturing via surgical robot: An algorithm for optimal selection of needle diameter, shape, and path," in *Robotics and Automation (ICRA), IEEE Int'l Conference on*, IEEE, 2017, pp. 2391–2398.

[84] S. Sen, A. Garg, D. V. Gealy, S. McKinley, Y. Jen, and K. Goldberg, "Automating multi-throw multilateral surgical suturing with a mechanical needle guide and sequential convex optimization," in *IEEE Int'l Conf. on Robotics and Automation (ICRA)*, 2016, pp. 4178–4185.

[85] A. Shademan, R. S. Decker, J. D. Opfermann, S. Leonard, A. Krieger, and P. C. Kim, "Supervised autonomous robotic soft tissue surgery," *Science translational medicine*, vol. 8, no. 337, 2016.

[86] F. Alambeigi, Z. Wang, Y.-h. Liu, R. H. Taylor, and M. Armand, "Toward semi-autonomous cryoablation of kidney tumors via model-independent deformable tissue manipulation technique," *Annals of Biomedical Engineering*, vol. 46, no. 10, pp. 1650–1662, 2018.

[87] F. Alambeigi, Z. Wang, R. Hegeman, Y.-H. Liu, and M. Armand, "Autonomous data-driven manipulation of unknown anisotropic deformable tissues using unmodelled continuum manipulators," *IEEE Robotics and Automation Letters*, vol. 4, no. 2, pp. 254–261, 2019.

[88] A. Murali, S. Sen, B. Kehoe, *et al.*, "Learning by observation for surgical subtasks: Multilateral cutting of 3d viscoelastic and 2d orthotropic tissue phantoms," in *2015*

IEEE International Conference on Robotics and Automation (ICRA), IEEE, 2015, pp. 1202–1209.

[89] C. Coulson, R. Taylor, A. Reid, M. Griffiths, D. Proops, and P. Brett, "An autonomous surgical robot for drilling a cochleostomy: Preliminary porcine trial," *Clinical Otolaryngology*, vol. 33, no. 4, pp. 343–347, 2008.

[90] F. Alambeigi, M. Bakhtiarinejad, S. Sefati, *et al.*, "On the use of a continuum manipulator and a bendable medical screw for minimally-invasive interventions in orthopedic surgery," *IEEE Trans. on Medical Robotics and Bionics*, 2019.

[91] F. Alambeigi, Z. Wang, R. Hegeman, Y.-H. Liu, and M. Armand, "A robust data-driven approach for online learning and manipulation of unmodeled 3-d heterogeneous compliant objects," *IEEE Robotics and Automation Letters*, vol. 3, no. 4, pp. 4140–4147, 2018.

[92] A. Krizhevsky, I. Sutskever, and G. E. Hinton, "Imagenet classification with deep convolutional neural networks," in *Advances in neural information processing systems*, 2012, pp. 1097–1105.

[93] S. Levine, C. Finn, T. Darrell, and P. Abbeel, "End-to-end training of deep visuomotor policies," *The Journal of Machine Learning Research*, vol. 17, no. 1, pp. 1334–1373, 2016.

[94] S. Hirai and T. Wada, "Indirect simultaneous positioning of deformable objects with multi-pinching fingers based on an uncertain model," *Robotica*, vol. 18, no. 1, pp. 3–11, 2000.

[95] P. Jiménez, "Survey on model-based manipulation planning of deformable objects," *Robotics and computer-integrated manufacturing*, vol. 28, no. 2, pp. 154–163, 2012.

[96] C. Shin, P. W. Ferguson, S. A. Pedram, J. Ma, E. P. Dutson, and J. Rosen, "Autonomous tissue manipulation via surgical robot using learning based model predic-

tive control," in *Int'l Conference on Robotics and Automation (ICRA)*, IEEE, 2019, pp. 3875–3881.

[97] F. Alambeigi, S. A. Pedram, J. L. Speyer, *et al.*, "Scade: Simultaneous sensor calibration and deformation estimation of fbg-equipped unmodeled continuum manipulators," *IEEE Transactions on Robotics*, 2019.

[98] C. Bishop, *Pattern recognition and machine learning.* springer, 2006.

[99] J. Peters, K. Mulling, and Y. Altun, "Relative entropy policy search," in *Twenty-Fourth AAAI Conference on Artificial Intelligence*, 2010.

[100] M. P. Deisenroth, G. Neumann, and J. Peters, "A survey on policy search for robotics," *Foundations and Trends® in Robotics*, vol. 2, no. 1–2, pp. 1–142, 2013, ISSN: 1935-8253. DOI: `10.1561/2300000021`. [Online]. Available: `http://dx.doi.org/10.1561/2300000021`.

[101] S. Gu, T. Lillicrap, I. Sutskever, and S. Levine, "Continuous deep q-learning with model-based acceleration," in *International Conference on Machine Learning*, 2016, pp. 2829–2838.

[102] C. J. Watkins and P. Dayan, "Q-learning," *Machine learning*, vol. 8, no. 3-4, pp. 279–292, 1992.

[103] C. J. C. H. Watkins, "Learning from delayed rewards," Ph.D. dissertation, King's College, Cambridge, 1989.

[104] J. Kober, J. A. Bagnell, and J. Peters, "Reinforcement learning in robotics: A survey," *The International Journal of Robotics Research*, vol. 32, no. 11, pp. 1238–1274, 2013.

[105] D. Navarro-Alarcon, H. M. Yip, Z. Wang, *et al.*, "Automatic 3-d manipulation of soft objects by robotic arms with an adaptive deformation model," *IEEE Transactions on Robotics*, vol. 32, no. 2, pp. 429–441, 2016.

[106] B. Hannaford, J. Rosen, D. W. Friedman, *et al.*, "Raven-ii: An open platform for surgical robotics research," *IEEE Transactions on Biomedical Engineering*, vol. 60, no. 4, pp. 954–959, 2013.

[107] R. S. Sutton and A. G. Barto, *Introduction to reinforcement learning.* MIT press Cambridge, 1998, vol. 135.

[108] T. J. Rivlin, *An introduction to the approximation of functions.* Courier Corporation, 2003.

[109] D. Pandey and P. Pandey, "Approximate q-learning: An introduction," in *2010 int'l conf. on machine learning and computing*, pp. 317–320.

[110] V. Mnih, K. Kavukcuoglu, D. Silver, *et al.*, "Playing atari with deep reinforcement learning," *arXiv preprint arXiv:1312.5602*, 2013.

[111] L. N. Smith, "Cyclical learning rates for training neural networks," in *2017 IEEE Winter Conference on Applications of Computer Vision (WACV)*, Mar. 2017, pp. 464–472. DOI: `10.1109/WACV.2017.58`.

[112] F. Conti, F. Barbagli, R. Balaniuk, *et al.*, "The chai libraries," in *Proc. of Eurohaptics 2003*, Dublin, Ireland, 2003, pp. 496–500.

[113] G. Bradski and A. Kaehler, "Opencv," *Dr. Dobb's journal of software tools*, vol. 3, 2000.

[114] D. Hearn, M. P. Baker, and M. P. Baker, *Computer graphics with OpenGL.* Pearson Prentice Hall Upper Saddle River, NJ: 2004, vol. 3.

[115] S. Ren, K. He, R. Girshick, and J. Sun, "Faster r-cnn: Towards real-time object detection with region proposal networks," in *Advances in neural information processing systems*, 2015, pp. 91–99.

[116] S. A. Pedram*, P. W. Ferguson*, M. J. Gerber, C. Shin, J.-P. Hubschman, and J. Rosen, “A Novel Tissue Identification Framework in Cataract Surgery Using an Integrated Bioimpedance-Based Probe and Machine Learning Algorithms,” *IEEE Transactions on Biomedical Engineering*, vol. 69, no. 2, pp. 910–920, 2022. DOI: `10.1109/TBME.2021.3109246`.

[117] D. Pascolini and S. P. Mariotti, “Global estimates of visual impairment: 2010,” *British Journal of Ophthalmology*, vol. 96, no. 5, pp. 614–618, 2012.

[118] R. Lindstrom, “Thoughts on cataract surgery: 2015,” *Rev Ophthalmol*, 2015.

[119] K. E. Donaldson, R. Braga-Mele, F. Cabot, *et al.*, “Femtosecond laser–assisted cataract surgery,” *Journal of Cataract & Refractive Surgery*, vol. 39, no. 11, pp. 1753–1763, 2013, ISSN: 0886-3350. DOI: `https://doi.org/10.1016/j.jcrs.2013.09.002`. [Online]. Available: `https://www.sciencedirect.com/science/article/pii/S0886335013011929`.

[120] D. Palanker, G. Schuele, N. J. Friedman, *et al.*, “Cataract surgery with oct-guided femtosecond laser,” in *Optics in the Life Sciences*, Optica Publishing Group, 2011, BTuC4. DOI: `10.1364/BODA.2011.BTuC4`. [Online]. Available: `http://opg.optica.org/abstract.cfm?URI=BODA-2011-BTuC4`.

[121] T. V. Roberts, M. Lawless, S. J. Bali, C. Hodge, and G. Sutton, “Surgical outcomes and safety of femtosecond laser cataract surgery: A prospective study of 1500 consecutive cases,” *Ophthalmology*, vol. 120, no. 2, pp. 227–233, 2013, ISSN: 0161-6420. DOI: `https://doi.org/10.1016/j.ophtha.2012.10.026`. [Online]. Available: `https://www.sciencedirect.com/science/article/pii/S0161642012010457`.

[122] C. N. Riviere, R. S. Rader, and P. K. Khosla, “Characteristics of hand motion of eye surgeons,” in *Proceedings of the 19th Annual International Conference of the IEEE Engineering in Medicine and Biology Society.'Magnificent Milestones and Emerging*

Opportunities in Medical Engineering'(Cat. No. 97CH36136), IEEE, vol. 4, 1997, pp. 1690–1693.

[123] P. B. Hibbard, A. E. Haines, and R. L. Hornsey, "Magnitude, precision, and realism of depth perception in stereoscopic vision," *Cognitive Research: Principles and Implications*, vol. 2, no. 1, p. 25, 2017.

[124] M. Zare, M.-A. Javadi, B. Einollahi, A.-R. Baradaran-Rafii, S. Feizi, and V. Kiavash, "Risk factors for posterior capsule rupture and vitreous loss during phacoemulsification," *Journal of ophthalmic & vision research*, vol. 4, no. 4, p. 208, 2009.

[125] J. Y. Paik, M. Shiloach, and M. S. Macsai-Kaplan, "The effect of posterior capsule polishing on posterior capsule opacification," *Investigative Ophthalmology & Visual Science*, vol. 53, no. 14, pp. 6668–6668, 2012.

[126] A. Kurt, C. Caglar, A. Gül, *et al.*, "Effect of anterior and posterior capsular polishing on the rate of posterior capsule opacification," *Journal of Advances in Medicine and Medical Research*, pp. 1–7, 2016.

[127] M. D. de Smet, T. C. M. Meenink, T. Janssens, *et al.*, "Robotic assisted cannulation of occluded retinal veins," *PLOS ONE*, vol. 11, no. 9, pp. 1–16, Sep. 2016. DOI: `10.1371/journal.pone.0162037`. [Online]. Available: `https://doi.org/10.1371/journal.pone.0162037`.

[128] M. D. de Smet, J. M. Stassen, T. C. M. Meenink, *et al.*, "Release of experimental retinal vein occlusions by direct intraluminal injection of ocriplasmin," *British Journal of Ophthalmology*, vol. 100, no. 12, pp. 1742–1746, 2016, ISSN: 0007-1161. DOI: `10.1136/bjophthalmol-2016-309190`. eprint: `https://bjo.bmj.com/content/100/12/1742.full.pdf`. [Online]. Available: `https://bjo.bmj.com/content/100/12/1742`.

[129] K. Willekens, A. Gijbels, L. Schoevaerdts, *et al.*, "Robot-assisted retinal vein cannulation in an in vivo porcine retinal vein occlusion model," *Acta Ophthalmologica*, vol. 95, no. 3, pp. 270–275, 2017.

[130] A. Gijbels, J. Smits, L. Schoevaerdts, *et al.*, "In-human robot-assisted retinal vein cannulation, a world first," *Annals of Biomedical Engineering*, vol. 46, no. 10, pp. 1676–1685, 2018.

[131] E. Rahimy, J. Wilson, T.-C. Tsao, S. Schwartz, and J.-P. Hubschman, "Robot-assisted intraocular surgery: Development of the iriss and feasibility studies in an animal model," *Eye*, vol. 27, no. 8, p. 972, 2013.

[132] J. T. Wilson, M. J. Gerber, S. W. Prince, *et al.*, "Intraocular robotic interventional surgical system (iriss): Mechanical design, evaluation, and master–slave manipulation," *The International Journal of Medical Robotics and Computer Assisted Surgery*, vol. 14, no. 1, e1842, 2018, e1842 rcs.1842. DOI: `https://doi.org/10.1002/rcs.1842`. eprint: `https://onlinelibrary.wiley.com/doi/pdf/10.1002/rcs.1842`. [Online]. Available: `https://onlinelibrary.wiley.com/doi/abs/10.1002/rcs.1842`.

[133] C.-W. Chen, Y.-H. Lee, M. J. Gerber, *et al.*, "Intraocular robotic interventional surgical system (iriss): Semi-automated oct-guided cataract removal," *The International Journal of Medical Robotics and Computer Assisted Surgery*, vol. 14, no. 6, e1949, 2018, e1949 rcs.1949. DOI: `https://doi.org/10.1002/rcs.1949`. eprint: `https://onlinelibrary.wiley.com/doi/pdf/10.1002/rcs.1949`. [Online]. Available: `https://onlinelibrary.wiley.com/doi/abs/10.1002/rcs.1949`.

[134] C.-W. Chen, A. A. Francone, M. J. Gerber, *et al.*, "Semiautomated optical coherence tomography-guided robotic surgery for porcine lens removal," *Journal of Cataract & Refractive Surgery*, vol. 45, no. 11, pp. 1665–1669, 2019, ISSN: 0886-3350. DOI:

https://doi.org/10.1016/j.jcrs.2019.06.020. [Online]. Available: https://www.sciencedirect.com/science/article/pii/S0886335019304948.

[135] S. Krag and T. T. Andreassen, "Mechanical properties of the human posterior lens capsule," *Investigative ophthalmology & visual science*, vol. 44, no. 2, pp. 691–696, 2003.

[136] H. Yu, J.-H. Shen, K. M. Joos, and N. Simaan, "Calibration and integration of b-mode optical coherence tomography for assistive control in robotic microsurgery," *IEEE/ASME Transactions on Mechatronics*, vol. 21, no. 6, pp. 2613–2623, 2016. DOI: 10.1109/TMECH.2016.2583259.

[137] B. R. Lee, W. W. Roberts, D. G. Smith, *et al.*, "Bioimpedance: Novel use of a minimally invasive technique for cancer localization in the intact prostate," *The Prostate*, vol. 39, no. 3, pp. 213–218, 1999. DOI: https://doi.org/10.1002/(SICI)1097-0045(19990515)39:3<213::AID-PROS10>3.0.CO;2-8. eprint: https://onlinelibrary.wiley.com/doi/pdf/10.1002/\%28SICI\%291097-0045\%2819990515\%2939\%3A3\%3C213\%3A\%3AAID-PROS10\%3E3.0.CO\%3B2-8. [Online]. Available: https://onlinelibrary.wiley.com/doi/abs/10.1002/%5C%28SICI%5C%291097-0045%5C%2819990515%5C%2939%5C%3A3%5C%3C213%5C%3A%5C%3AAID-PROS10%5C%3E3.0.CO%5C%3B2-8.

[138] D. J. Hernandez, V. A. Sinkov, W. W. Roberts, *et al.*, "Measurement of bio-impedance with a smart needle to confirm percutaneous kidney access," *The Journal of Urology*, vol. 166, no. 4, pp. 1520–1523, 2001.

[139] Z. Cheng, B. L. Davies, D. G. Caldwell, and L. S. Mattos, "A venipuncture detection system for robot-assisted intravenous catheterization," in *2016 6th IEEE International Conference on Biomedical Robotics and Biomechatronics (BioRob)*, 2016, pp. 80–86. DOI: 10.1109/BIOROB.2016.7523602.

[140] L. Schoevaerdts, G. Borghesan, M. Ourak, D. Reynaerts, and E. V. Poorten, "Electrical bio-impedance proximity sensing for vitreo-retinal micro-surgery," *IEEE Robotics and Automation Letters*, vol. 4, no. 4, pp. 4086–4093, 2019. DOI: `10.1109/LRA.2019.2930482`.

[141] L. Schovaerdts, L. Esteveny, A. Gijbels, J. Smits, D. Reynaerts, and E. Vander Poorten, "Design and evaluation of a new bioelectrical impedance sensor for micro-surgery: Application to retinal vein cannulation," *International Journal of Computer Assisted Radiology and Surgery*, vol. 14, no. 2, pp. 311–320, 2019. DOI: `https://doi.org/10.1007/s11548-018-1850-3`.

[142] H. Zauberman, H. De Guillebon, and F. J. Holly, "Retinal traction in vitro : Biophysical aspects," *Investigative Ophthalmology & Visual Science*, vol. 11, no. 1, pp. 46–55, Jan. 1972, ISSN: 1552-5783. eprint: `https://arvojournals.org/arvo/content\_public/journal/iovs/932867/46.pdf`.

[143] D. A. Luce, "Determining in vivo biomechanical properties of the cornea with an ocular response analyzer," *Journal of Cataract & Refractive Surgery*, vol. 31, no. 1, pp. 156–162, 2005.

[144] W. K. McEwen, M. Shepherd, and E. H. McBain, "An Electrical Model of the Human Eye : I. The basic model," *Investigative Ophthalmology & Visual Science*, vol. 6, no. 2, pp. 155–159, Apr. 1967, ISSN: 1552-5783.

[145] D. C. Toledo-Pérez, J. Rodríguez-Reséndiz, R. A. Gómez-Loenzo, and J. Jauregui-Correa, "Support vector machine-based emg signal classification techniques: A review," *Applied Sciences*, vol. 9, no. 20, p. 4402, 2019.

[146] Z. Xiong, M. K. Stiles, and J. Zhao, "Robust ecg signal classification for detection of atrial fibrillation using a novel neural network," in *2017 Computing in Cardiology (CinC)*, IEEE, 2017, pp. 1–4.

[147] M. Zihlmann, D. Perekrestenko, and M. Tschannen, “Convolutional recurrent neural networks for electrocardiogram classification,” in *2017 Computing in Cardiology (CinC)*, IEEE, 2017, pp. 1–4.

[148] M. Zia ur Rehman, A. Waris, S. O. Gilani, *et al.*, “Multiday emg-based classification of hand motions with deep learning techniques,” *Sensors*, vol. 18, no. 8, 2018, ISSN: 1424-8220. DOI: `10.3390/s18082497`. [Online]. Available: `https://www.mdpi.com/1424-8220/18/8/2497`.

[149] K. P. Murphy, *Machine learning: a probabilistic perspective.* MIT press, 2012.

[150] W.-Y. Loh, “Classification and regression trees,” *Wiley interdisciplinary reviews: data mining and knowledge discovery*, vol. 1, no. 1, pp. 14–23, 2011.

[151] Y. Freund and R. E. Schapire, “A decision-theoretic generalization of on-line learning and an application to boosting,” *Journal of computer and system sciences*, vol. 55, no. 1, pp. 119–139, 1997.

[152] L. Breiman, “Random forests,” *Machine learning*, vol. 45, no. 1, pp. 5–32, 2001.

[153] L. Wang, *Support vector machines: theory and applications.* Springer Science & Business Media, 2005, vol. 177.

[154] D. P. Kingma and J. Ba, “Adam: A method for stochastic optimization,” *arXiv preprint arXiv:1412.6980*, 2014.